

3-1-2017

Thermodynamics and Kinetics of Ligand Photodissociation in Heme Proteins and Formation of DNA i-Motif

David S. Butcher
dbutc001@fiu.edu

DOI: 10.25148/etd.FIDC001737

Follow this and additional works at: <https://digitalcommons.fiu.edu/etd>

 Part of the [Biochemistry Commons](#), and the [Biophysics Commons](#)

Recommended Citation

Butcher, David S., "Thermodynamics and Kinetics of Ligand Photodissociation in Heme Proteins and Formation of DNA i-Motif" (2017). *FIU Electronic Theses and Dissertations*. 3259.
<https://digitalcommons.fiu.edu/etd/3259>

This work is brought to you for free and open access by the University Graduate School at FIU Digital Commons. It has been accepted for inclusion in FIU Electronic Theses and Dissertations by an authorized administrator of FIU Digital Commons. For more information, please contact dcc@fiu.edu.

FLORIDA INTERNATIONAL UNIVERSITY

Miami, Florida

THERMODYNAMICS AND KINETICS OF LIGAND PHOTODISSOCIATION IN
HEME PROTEINS AND FORMATION OF DNA I-MOTIF

A dissertation submitted in partial fulfillment of

the requirements for the degree of

DOCTOR OF PHILOSOPHY

in

CHEMISTRY

by

David Butcher

2017

To: Dean Michael R. Heithaus
College of Arts, Sciences and Education

This dissertation, written by David Butcher, and entitled Thermodynamics and Kinetics of Ligand Photodissociation in Heme Proteins and Formation of DNA i-Motif, having been approved in respect to style and intellectual content, is referred to you for your judgment.

We have read this dissertation and recommend that it be approved.

Joong Ho Moon

Konstantinos Kavallieratos

Yuk-Ching Tse-Dinh

Irina Agoulnik

Jaroslava Miksovska, Major Professor

Date of Defense: March 1, 2017

The dissertation of David Butcher is approved.

Dean Michael R. Heithaus
College of Arts, Sciences and Education

Andrés G. Gil
Vice President for Research and Economic Development
and Dean of the University Graduate School

Florida International University, 2017

© Copyright 2017 by David Butcher

All rights reserved.

DEDICATION

This dissertation is dedicated to my mother, father and brother, who have provided support throughout my academic career; to my grandparents Kenneth and Mikki who have given me much-needed emotional and financial assistance; and to the memory of my grandmother Altagracia, who was a constant source of love and inspiration.

ACKNOWLEDGMENTS

I would like to gratefully acknowledge the support of former group members Drs. Luisana Astudillo, Walter Gonzalez, and Khoa Pham who shared their time and knowledge freely and without reservation. I would also like to thank current group members Antonija Tangar, Samiol Azam, and Setareh Sakhdari for helping to make the lab an enjoyable place to spend every waking hour.

I am grateful to the Graduate & Professional Student Committee and the College of Arts & Sciences for providing travel funding to assist in my professional development and to the MBRS-RISE Biomedical Research Initiative for providing funds enabling computational research, much of which appears in this dissertation.

I thank the members of my dissertation committee, Professors Jaroslava Miksovská, Konstantinos Kavallieratos, Joong Ho Moon, Irina Agoulnik, and Yuk-Ching Tse-Dinh for their participation and valuable criticism. I also thank Professors Fenfei Leng and Martin Quirke for encouragement, assistance and valuable advice.

Lastly, I would like to thank Professor Jaroslava Miksovská once again for providing the initial inspiration to take on the challenge of doctoral studies and for providing criticism and encouragement of the necessary amount and intensity.

ABSTRACT OF THE DISSERTATION
THERMODYNAMICS AND KINETICS OF LIGAND PHOTODISSOCIATION IN
HEME PROTEINS AND FORMATION OF DNA I-MOTIF

by

David Butcher

Florida International University, 2017

Miami, Florida

Professor Jaroslava Miksovska, Major Professor

Heme proteins carry out a diverse array of functions *in vivo* while maintaining a well-conserved 3-over-3 α -helical structure. Human hemoglobin (Hb) is well-known for its oxygen transport function. Type 1 non-symbiotic hemoglobins (nsHb1) in plants and bacterial flavohemoglobins (fHb) from a variety of bacterial species have been predicted to carry out a nitric oxide dioxygenase function. In nsHb1 and fHb this function has been linked to protection from nitrosative stress. Herein, I combine photoacoustic calorimetry (PAC), transient absorption spectroscopy (TA), and classical molecular dynamics (cMD) simulations to characterize molecular mechanism of diatomic ligand interactions with a hexa-coordinate globin from plant (rice hemoglobin), bacterial flavohemoglobins and human hemoglobin.

In rice type 1 non-symbiotic hemoglobin (rHb1), the dynamics and energetics of structural changes associated with ligand photodissociation is strongly impacted by solvent and temperature, namely CO escape from the protein matrix is slower at pH = 6.0 compare to neutral pH (<50 ns) due to the CD loop reorganization which forms a pathway for ligand

escape. In human hemoglobin, exogenous allosteric effectors modulate energetics of conformational changes associated with the CO and O₂ escape although the effectors impact on rate constants for ligand association is small. The conformational dynamics associated with ligand photorelease from fHbs from *Cupriavidus necator* (FHP) and *Staphylococcus aureus* (HMP_{sa}) are strongly modulated by the presence ofazole drugs indicating that drug association modulates structural properties of the heme binding pocket.

In addition, we carried out a study of the formation of the DNA intercalated motif (i-motif). The formation of the structure is strongly favored at acidic pH; therefore, PAC was combined with a 2-nitrobenzaldehyde pH-jump to probe formation of the i-motif on fast timescales. i-Motif folding is two-step process with the initial protonation of cytosine residues being endothermic with $\Delta H_{\text{fast}}=8.5 \pm 7.0 \text{ kcal mol}^{-1}$ and $\Delta V_{\text{fast}}=10.4 \pm 1.6 \text{ mL mol}^{-1}$ and subsequent nucleation/i-motif folding ($\tau = 140 \text{ ns}$) with $\Delta H_{\text{slow}}=-51.5 \pm 4.8 \text{ kcal mol}^{-1}$ and $\Delta V_{\text{slow}}=-6.6 \pm 0.9 \text{ mL mol}^{-1}$. The above results indicate that PAC can be employed to study diverse biochemical reactions such as DNA folding, drug binding and ligand photorelease from proteins.

TABLE OF CONTENTS

CHAPTER	PAGE
1 INTRODUCTION	2
2 MATERIALS AND METHODS	10
2.1 Materials	10
2.2 Methods	10
2.2.1 Recombinant expression of rice type 1 non-symbiotic hemoglobin wild-type and H73L mutant	10
2.2.2 Photoacoustic calorimetry	13
2.2.2.1 Rice hemoglobin PAC procedure	13
2.2.2.2 Human hemoglobin PAC procedure	14
2.2.2.3 2-nitrobenzaldehyde & i-motif DNA PAC	15
2.2.2.4 PAC data analysis	16
2.2.3 Time-resolved transient absorption spectroscopy	20
2.2.3.1 Properties of ligand rebinding in heme proteins	20
2.2.3.2 Characterization of the 2-nitrobenzaldehyde pH-jump	22
2.2.4 Circular dichroism spectroscopy	25
2.2.5 Classical molecular dynamics simulations	25
3 THE ROLE OF IONIC STRENGTH AND PH IN MODULATING THERMODYNAMIC PROFILES ASSOCIATED WITH CO ESCAPE FROM RICE NON-SYMBIOTIC HEMOGLOBIN 1	28
3.1 Introduction	28
3.2 Results	30
3.2.1 UV-vis spectra	30
3.2.2 Kinetics of CO escape to the surrounding solvent	32
3.2.3 Volume and enthalpy changes of CO photorelease from rHb1	35
3.2.4 Temperature dependence of $\Delta H/\Delta V$ for CO escape	36
3.2.5 Kinetics for bimolecular CO rebinding	40
3.2.6 Classical molecular dynamics simulations	42
3.3 Discussion	46
3.3.1 Origin of the temperature dependence of thermodynamic parameters	46
3.3.2 Effects of histidine protonation on ligand migration	52
3.4 Conclusion	63
4 THERMODYNAMIC PARAMETERS FOR O ₂ PHOTORELEASE FROM HEMOGLOBIN:EFFECTOR COMPLEXES	64
4.1 Introduction	64
4.2 Results	67
4.2.1 UV-vis spectra	67
4.2.2 Photoacoustic calorimetry results	68
4.2.3 Transient absorption results	75

4.3	Discussion	78
4.3.1	Temperature dependence of ΔH and ΔV	79
4.3.2	Ligand dependence of ΔH and ΔV	82
4.3.3	Bimolecular quantum yield.....	84
4.3.4	Rate constants for geminate rebinding.....	86
4.4	Conclusion.....	88
5	IMPACT OF AZOLE DRUGS ON ENERGETICS, KINETICS, AND LIGAND MIGRATION PATHWAYS OF CO PHOTODISSOCIATION IN BACTERIAL FLAVOHEMOGLOBINS	90
5.1	Introduction	90
5.2	Results	92
5.2.1	UV-vis Spectroscopy	92
5.2.2	PAC & TA Results.....	95
5.2.3	Classical Molecular Dynamics	101
5.2.3.1	CO migration pathways within FHP	101
5.2.3.2	Binding sites of ketoconazole and miconazole in FHP	104
5.3	Discussion	107
5.3.1	The effect of azole drugs on ligand migration pathways in FHP	107
5.3.2	The impact of azole drugs on thermodynamic and kinetic parameters	109
5.3.3	Mechanism of inhibition of fHbs by azole drugs.....	116
5.4	Conclusion.....	118
6	STRUCTURES OF THE KINETICALLY TRAPPED I-MOTIF DNA INTERMEDIATES.....	120
6.1	Introduction	120
6.2	Results	122
6.2.1	Parameters of the 2-nitrobenzaldehyde pH-jump	122
6.2.2	Folding equilibrium determined by circular dichroism	123
6.2.3	Enthalpy and volume changes determined by PAC.....	123
6.3	Discussion	125
6.4	Conclusion.....	129
7	CONCLUSIONS.....	130
	LIST OF REFERENCES	133
	VITA.....	150

LIST OF TABLES

TABLE	PAGE
Table 3.1 Observed volume and enthalpy changes associated with photo-dissociation of CO from WT and H73L mutant rHb1.	34
Table 3.2 Thermodynamic and kinetic parameters determined for the PAC slow phase of CO photo-dissociation from CO-rHb1 WT and H73L. Parameters determined using Arrhenius and Eyring plots.	34
Table 3.3 Rate constants and activation parameters determined from Arrhenius and Eyring plots for bimolecular recombination of CO to deoxy-rHb1 WT and H73L. Stripped and 0.50 M NaCl studies were conducted in 20 mM HEPES at pH 7.0. ...	42
Table 3.4 A selection of data from analysis of cMD trajectories, including average distance between the proximal His and distal residue α -carbons ($r_{\alpha-\alpha}$), average distance between ζ -nitrogen of Lys69 and the heme-6-propionate group carboxyl carbon, and average distance between guanidino carbon of Arg103 and heme-7-propionate group carboxyl carbon. Data derived from then H73L mutant simulations are highlighted in gray. Values of $r_{\alpha-\alpha}$ are presented with standard deviations derived from at least 2000 MD snapshots. Multiple values indicate multiple stable conformations, with approximate percentage of frames in the closer conformation in the last 2000 frames of each simulation given in parentheses.	43
Table 4.1 Volume and enthalpy changes (ΔV and ΔH) associated with CO/O ₂ photodissociation from stripped Hb and Hb:effector complexes.....	71
Table 4.2 Rate constants for geminate rebinding of O ₂ to stripped (O ₂) ₃ Hb and (O ₂) ₃ Hb:effector complexes at 25°C as determined by MEM analysis. Conditions: 30 μ M Hb, 20 mM HEPES buffer, pH 7.0.	76
Table 4.3 Quantum yield and rate constants for bimolecular rebinding of O ₂ to stripped (O ₂) ₃ Hb and (O ₂) ₃ Hb:effector complexes at 25°C as determined by MEM analysis. Conditions: 30 μ M Hb, 20 mM HEPES buffer, pH 7.0.....	76
Table 4.4 Rate constants for geminate and bimolecular rebinding of O ₂ to stripped (O ₂) ₃ Hb and (O ₂) ₃ Hb:effector complexes at 25°C as determined by fitting to a three exponential decay model. Conditions: 30 μ M Hb, 20 mM HEPES buffer, pH 7.0.....	77

Table 5.1 Thermodynamic parameters determined using PAC for photo-release of CO from CO-bound flavohemoglobins from <i>Ralstonia eutropha</i> (FHP) and <i>Staphylococcus aureus</i> (HMP _{sa}) in the presence and absence of ketoconazole and miconazole. Asterisks indicate hypothetical values and correspond to ΔH_{bound} and ΔV_{bound}	97
Table 5.2 Pathways of CO escape observed during 30 ns MD simulation of CO:FHP using locally enhanced sampling with 20 enhanced ligands.....	102
Table 5.3 Rate constants for “slow” geminate and bimolecular rebinding of CO to flavohemoglobins from <i>Ralstonia eutropha</i> (FHP) and <i>Staphylococcus aureus</i> (HMP _{sa}) in the presence and absence of ketoconazole and miconazole. Error values are standard deviations for multiple runs. for All data listed were determined at 20 °C.	110

LIST OF FIGURES

FIGURE	PAGE
Figure 1.1 Crystal structure of oxygen-bound <i>Phyester catodon</i> (sperm whale) myoglobin (158). (PDB: 1A6M).....	2
Figure 1.2 Structure of heme B. Central iron atom is shown in the common 2+ oxidation state.	3
Figure 1.3 Crystal structures of penta-coordinate deoxy-Hb (left, PDB ID: 2DN2) (121) and hexa-coordinate rHb1 (right, PDB ID: 1D8U). (40)	4
Figure 1.4 (Left) Crystal structure of the α subunit of human oxyHb (PDB ID: 2DN1). (121) (Right) Heme active site of α subunit of human oxyHb showing interaction between distal His and bound ligand.	6
Figure 1.5 Cavities determined in the crystal structure of deoxy-Mb (PDB ID: 1A6N) (158) using a probe radius of 1.4 Å.	7
Figure 2.1 Instrument setup for TA studies of ligand rebinding to heme proteins.	20
Figure 2.2 Instrument setup for characterization of 2-nitrobenzaldehyde pH-jump using TA.	22
Figure 2.3 (Top) Absorption spectra of 50 μ M pyranine in 50 mM sodium phosphate buffer.	23
Figure 2.4 Example TA trace for photolysis of 1.0 mM 2-NBA with a total laser power of 15.3 mJ in the presence of 50 μ M bromocresol green in deionized water at 20 °C.	24
Figure 3.1(Left) Steady-state UV-vis absorption spectra for rHb1 WT in the met form (solid line), deoxy form (dashed line) and CO-bound (dotted line). Conditions: 5 μ M rHb1 WT in 20 mM HEPES buffer, pH 7.5.....	31
Figure 3.2 PAC traces for CO photorelease from rHb1 WT at pH 6.0 at 12 °C (black line) and heat deposited to the solvent by Fe(III)4SP under same conditions (red line). Simulated trace produced by convolution of component waves in Sound Analysis 1.50D is shown in gray.	32

Figure 3.3 Arrhenius plots for CO escape from rHb1 WT (black) and H73L (grey) in 20 mM HEPES, pH 6.0.	33
Figure 3.4 Plot of $E_{hv}(\phi_{1-1})/\Phi_{bm}$ vs. C_{pp}/β for CO photorelease from CO-rHb1 WT (black) and H73L (gray) under stripped conditions (squares) and with 0.50 M NaCl (open circles).	37
Figure 3.5 Plot of $E_{hv}(\phi_{1-1})/\Phi_{bm}$ and $E_{hv}(\phi_{2})/\Phi_{bm}$ versus the temperature dependent factor (C_{pp}/β) for CO photorelease from CO-rHb1 WT (black) and H73L (gray) the data for the fast phase (<50 ns) and slow phase (~50 ns – 10 μ s) are shown as closed triangles and open inverted triangles respectively.	38
Figure 3.6 Representative TA traces determined for rebinding of CO to deoxy-rHb1 WT under stripped conditions (black), with 0.50 M NaCl (grey) and at pH 6 (light grey) at 20 °C.	40
Figure 3.7 Quantum yields for bimolecular recombination of CO to rHb1 WT (black) and H73L (grey) under stripped conditions (squares), with 0.50 M NaCl (open circles), and in pH 6.0 HEPES buffer (triangles).	41
Figure 3.8 Top Panel: Distance between ζ -nitrogen of Lys69 and carboxyl carbon of heme-6-propionate group during cMD trajectory of penta-coordinate WT rHb1 (black line) and CO-rHb1 WT (grey line).	44
Figure 3.9 Channels determined in MD simulation of deprotonated CO-rHb1 WT (left) and deprotonated CO-rHb1 H73L (right) along with critical residues and an F-helix fragment. Critical residues bordering the channels are shown as stick representations.	45
Figure 3.10 Representative positions of charged residues and heme propionate groups taken from cMD simulations of penta-coordinate WT (left) and CO-bound WT rHb1 (right) with His residue deprotonated. Proximal and distal histidines are not shown.	48
Figure 3.11 Overlay of EF region of deprotonated penta-coordinate rHb1 WT (green) and deprotonated CO-bound rHb1 WT (cyan) cMD simulations. Interhelical distance ($r_{\alpha-\alpha}$) of penta-coordinate WT is given by orange dotted line and text, while that of the CO-bound species is given by the red dotted line and text.	49
Figure 3.12 Fraction of protonated His 73 in oxidized rHb1 WT as determined by shift in Soret band wavelength according to the method of Nienhaus et al. (78)	54

Figure 3.13 Distance between alcohol oxygen of Ser49 and N δ of His117 during cMD trajectories of penta-coordinate rHb1 WT (top) and penta-coordinate rHb1 H73L (bottom) without (black line) and with (grey line) protonation of His73, His117, and His152.	56
Figure 3.14 Overlay of EF region and CD loop of deprotonated 5c rHb1 WT (cyan) and protonated 5c rHb1 WT (cyan) cMD simulations. Residues 40 – 78 of the CD loop and E-helix and residues 102 – 112 of the F-helix are shown in cartoon representation.	57
Figure 3.15 CD loop and EF regions of rHb1 with representative cavities determined by MDpocket analysis shown. Carbon monoxide, His73, His108, His117, Ser49 and heme group shown. In all images residues 40 – 78 of the CD loop and E-helix and residues 102 – 112 of the F-helix are shown in cartoon representation.....	59
Figure 3.16 Sequence alignment of the top 10 nsHbs in the UniProt database with highest sequence homology to rHb1. The Ser at the C-terminal end of the B-helix (Ser49 in rHb1) and His in the CD loop (His117 in rHb1) are highlighted with red boxes.	62
Figure 4.1 Steady-state UV-vis absorption spectra of metHb (solid black line), deoxyHb (dashed line), and oxyHb (solid gray line) in 20 mM HEPES buffer with no effector present, pH 7.0. Inset: Absorbance spectra from 500 – 600 nm showing Q bands.....	68
Figure 4.2 PAC traces for O $_2$ photorelease from stripped oxyHb (black line) and the reference compound Fe(III)4SP (gray line) at 20°C in 20 mM HEPES buffer, pH 7.0.....	69
Figure 4.3 (Left) Plot of ratio of sample and reference acoustic trace amplitudes as a function of the temperature dependent factor (C_p/β) for CO photorelease from stripped CO-Hb (filled squares), O $_2$ photorelease from stripped oxyHb (open squares) and oxyHb in the presence of 500 mM NaCl (half-filled squares).....	70
Figure 5.1 UV-vis traces for met-, deoxy-, and CO-FHP in the absence ofazole drugs..	92
Figure 5.2 UV-vis traces for met-, deoxy-, and CO-FHP in the presence of 14 μ M ketoconazole.	93
Figure 5.3 Chemical structures of ketoconazole (top) and miconazole (bottom).....	93

Figure 5.4 UV-vis traces for met-, deoxy-, and CO-FHP in the presence of 408 μM miconazole.	94
Figure 5.5 Example PAC traces for dissociation of CO from CO-FHP (black) and 4SP reference compound (grey) at 20 $^{\circ}\text{C}$ in 10 mM sodium phosphate and 10 mM potassium chloride buffer, pH 7.5.....	95
Figure 5.6 Plots of $C_{p\rho}/\beta$ vs. $E_{\text{hv}}(\varphi-1)/\Phi_{\text{bm}}$ for photo-dissociation of CO from CO-FHP in the absence of drug compounds (black), with 14 μM ketoconazole (gray), and with 408 μM miconazole (light gray).	96
Figure 5.7 Plots of $C_{p\rho}/\beta$ vs. $E_{\text{hv}}(\varphi-1)/\Phi_{\text{bm}}$ for photo-dissociation of CO from CO-HMP _{Sa} in the absence of drug compounds (black), with 14 μM ketoconazole (gray), and with 408 μM miconazole (light gray).....	97
Figure 5.8 Example TA traces for bimolecular rebinding of CO to deoxy-FHP in the absence of azole drugs at 16 $^{\circ}\text{C}$ (black), 20 $^{\circ}\text{C}$ (dark gray), 26 $^{\circ}\text{C}$ (grey) and 35 $^{\circ}\text{C}$ (light gray).	99
Figure 5.9 Escape pathways found in LES-enabled simulation of CO escape from FHP. Pathways A and E are shown as red and green dashed lines respectively. CO molecules are shown in red and magenta.....	100
Figure 5.10 Alternate view of the overlay of MD snapshots of CO-FHP with ketoconazole bound (cyan) with the drug-free CO-FHP (magenta) after 20 ns of simulation. For both proteins residues 1 – 130 are shown as cartoon representations and Asn44 and Gln48 are shown as sticks. The ketoconazole molecule is shown with yellow carbons.	101
Figure 5.11 Binding locations of ketoconazole (left) and miconazole (right) to CO-FHP predicted by Autodock Vina. Heme, CO, Tyr29 and His85 are shown as licorice and the five drug conformations with highest binding affinity are shown as thin lines.	103
Figure 5.12 A view of the heme binding pocket of CO-FHP with ketoconazole bound after 20 ns of MD simulation. Hydrophobic interactions are shown as gray lines, cation- π interactions are shown as orange lines, and hydrogen bonds are shown as blue lines.	104
Figure 5.13 A view of the heme binding pocket of CO-FHP with miconazole bound after 20 ns of MD simulation. Hydrophobic interactions are shown as gray lines.	105

Figure 5.14 Overlay of MD snapshots of CO-FHP with ketoconazole bound (cyan) with the drug-free CO-FHP (magenta) after 20 ns of simulation. For both proteins residues 1 – 130 are shown as cartoon representations and Asn44 and Gln48 are shown as sticks. The ketoconazole molecule is shown with yellow carbons.	106
Figure 5.15 An alternate view of the heme binding pocket of CO-FHP with miconazole bound after 20 ns of MD simulation. Hydrophobic interactions are shown as gray lines.	107
Figure 6.1 (Right) Solution structure DNA i-motif with the sequence 5' d(CCCTA2CCCTA2CCCTA2CCCT)-3' determined by NMR (PDB: 1ELN) (157).	120
Figure 6.2 (Left) Molar attenuation coefficients as a function of pH for 50 μ M pyranine in 50 mM sodium phosphate buffer. Logistic fit of the data points is shown as a solid black line.	122
Figure 6.3 pH of the illuminated volume after photolysis of 2-NBA as a function of the cross-sectional power of the laser pulse. Error bars indicate the standard deviation of the laser power determined from the average of 100 laser pulses.	123
Figure 6.4 Circular dichroism spectra of i-motif DNA (30 μ M in deionized water) as a function of the solution pH = 4.0–9.0 at 20 $^{\circ}$ C.	124
Figure 6.5 Plot of the fast (ϕ_1) and slow (ϕ_2) phases as a function of $C_p\rho/\beta$ in the 16–26 $^{\circ}$ C temperature range. In the inset, PAC traces for 2-NBA photodissociation in the presence of i-motif DNA sample (blue) and 4SP reference compound (red) at 16 $^{\circ}$ C.	125
Figure 6.6 Arrhenius plot for the slow kinetic phase determined by PAC.	126

ABBREVIATIONS AND ACRONYMS

ϵ	Molar attenuation coefficient
$^{\circ}\text{C}$	Degrees Celsius
2-NBA	2-nitrobenzaldehyde
5c	Penta-coordinate
6c	Hexa-coordinate
BCG	Bromocresol green, 2,6-Dibromo-4-[7-(3,5-dibromo-4-hydroxy-2-methyl-phenyl)-9,9-dioxo-8-oxa-9 λ 6-thiabicyclo[4.3.0]nona-1,3,5-trien-7-yl]-3-methyl-phenol
BZF	Bezafibrate, 2-(4-{2-[(4-chlorobenzoyl)amino]ethyl}phenoxy)-2-methylpropanoic acid
CD	Circular dichroism spectroscopy
Cl^{-}	Chloride anion
cMD	Classical molecular dynamics
CN	Cyanide
CO	Carbon monoxide
CO-	Used to denote heme proteins with a CO molecule bound to the heme iron
C-rich	Cytosine-rich
deoxy-	Denotes heme proteins where the Fe atom of the heme cofactor is in the 2+ oxidation state
deoxyHb	Deoxyhemoglobin

EDTA	ethylenediaminetetraacetic acid
FADH	Flavin adenine dinucleotide, reduced form
Fe(III)4SP	Fe(III)meso-tetra(4-sulfonatophenyl)porphine chloride
fHb	Bacterial flavohemoglobin
FHP	<i>Cupriavidus necator</i> bacterial flavohemoglobin
G-rich	Guanosine-rich
Hb	Hemoglobin
HCl	hydrochloric acid
HEPES	2-[4-(2-hydroxyethyl)piperazin-1-yl]ethanesulfonic acid
HMP _{Sa}	<i>Staphylococcus aureus</i> bacterial flavohemoglobin
iDNA	Synthetic oligonucleotide of sequence 5'-[CCCTAA] ₃ CCC-3'
IHP	Inositol hexakisphosphate
IPTG	isopropyl β-D-1-thiogalactopyranoside
K _a	Acid dissociation constant
K _D	Dissociation constant
L35	2-[4-(3,5-dichlorophenylureido)phenoxy]-2-methylpropionic acid
LES	Locally enhanced sampling

Mb	Myoglobin
MEM	Maximum entropy method
met-	Denotes heme proteins where the Fe atom of the heme cofactor is in the 3+ oxidation state
metHb	Methemoglobin
MWC	Monod-Wyman-Changeux
N _ε	Nitrogen at position ε in the imidazole ring of the histidine amino acid residue
NADPH	Nicotinamide adenine dinucleotide phosphate, reduced form
NaCl	Sodium chloride
NaOH	sodium hydroxide
Nd:YAG	Neodymium-doped yttrium aluminum garnet
NMR	Nuclear magnetic resonance
NO	Nitric oxide
NOD	NO dioxygenase
NPT	Isothermal-isobaric ensemble
nsHb	Non-symbiotic hemoglobin
nsHb1	Type 1 non-symbiotic hemoglobin
N _δ	Nitrogen at position δ in the imidazole ring of the histidine amino acid residue

O ₂	Dioxygen
oxyHb	Oxyhemoglobin
PAC	Photoacoustic calorimetry
PDB	Protein Data Bank
pK _a	Logarithmic derivative of K _a ($\text{pK}_a = -\log_{10} K_a$)
Pyranine	Trisodium 8-hydroxypyrene-1,3,6-trisulfonate
rHb1	<i>Oryza sativa</i> type 1 non-symbiotic hemoglobin
r _{α-α}	EF region interhelical distance
ROS	Reactive oxygen species
sHb	Symbiotic hemoglobin
swMb	<i>Physeter catodon</i> (sperm whale) myoglobin
TA	Transient absorption spectroscopy
TB	Terrific broth
UV-vis	Ultraviolet and visible
WT	Wild-type
ΔH	Enthalpy change
ΔH [#]	Activation enthalpy change

ΔV	Volume change
Φ	Quantum yield for photo-induced processes
Φ_{bm}	Quantum yield for bimolecular rebinding of ligand molecule (CO or O ₂) to heme protein
Φ_{ref}	Quantum yield for bimolecular rebinding of CO to horse myoglobin

PREFACE

This dissertation contains research carried out between June 2011 and December 2016 by David Butcher under the supervision of Professor Jaroslava Miksovská at Florida International University. During this time, some of these results have been published as original research articles in peer-reviewed scientific journals.

Material from chapter 3 was accepted for publication in the Journal of Physical Chemistry B and published on their website (DOI: 10.1021/acs.jpcc.6b06933) and in print (*J. Phys. Chem. B*, **2017**, *121* (2), pp 351 – 364). Material from chapter 6 was published in Physical Chemistry Chemical Physics vol. 18, pg. 26691. Chapters 4 and 5 will be submitted for publication shortly. Chapter 5 in particular we would like to submit quickly to the ACS journal Chemical Biology.

1 INTRODUCTION

Heme proteins are a large and diverse family of proteins which exhibit a variety of activities in cells in several kingdoms of life. (1) (2) These activities include, but are not limited to transport and storage of dioxygen (O_2) as in myoglobin (Mb) and hemoglobin (Hb), hydroxylation of hydrophobic compounds (cytochromes P450), oxygenation, peroxidation, chloroperoxidation, nitric oxide (NO) synthesis, NO dioxygenation and electron transport (cytochromes). (3) The recently discovered vertebrate heme protein neuroglobin (4) has been suggested to participate in a variety of cell signaling pathways and has been demonstrated to protect neuronal tissues from damage under ischemic conditions. (5) In plants, the symbiotic and non-symbiotic hemoglobins are thought to participate in nitrogen fixation and in NO detoxification/signaling via their NO dioxygenase activity, respectively (6). Bacterial flavohemoglobins (fHbs) also exhibit NO dioxygenase activity and have been shown to protect bacterial cells from oxidative stress such as that associated with an immune response, enhancing bacterial survival in host

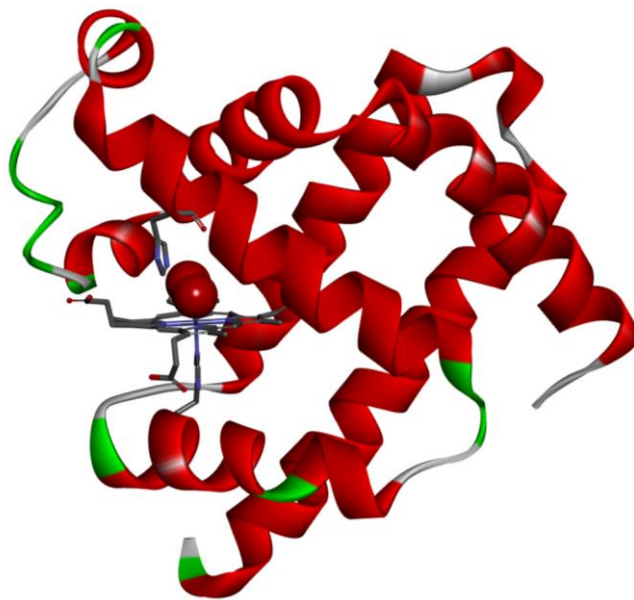


Figure 1.1 Crystal structure of oxygen-bound *Phyester catodon* (sperm whale) myoglobin (**162**). (PDB: 1A6M)

organisms (7). The diverse functions of heme proteins are enabled by the presence of the heme cofactor and the tuning of its reactivity and substrate accessibility by the protein matrix which encapsulates and complexes it. Various types of heme exist, but heme B is the most common form.

The heme B cofactor consists of an iron atom coordinated by the central nitrogen atoms of the macrocyclic protoporphyrin IX (Figure 1.2). Many heme globins exhibit a characteristic globin fold – a 3-over-3 α -helical “sandwich” structure (Figure 1.1) which envelops the porphyrin ring. (8) Recently, families of truncated heme proteins with a 2-over-2 fold which resembles the typical globin fold have been discovered in both plants and bacteria. (9) Regardless of the type of α -helical structure, the heme cofactor is universally buried in a hydrophobic cavity within the protein matrix with the heme propionate groups oriented towards the protein exterior, often in direct contact with the bulk solvent. Hydrophobic interactions between the protoporphyrin-IX macrocycle and protein matrix help to stabilize the position of the heme group within the protein. In

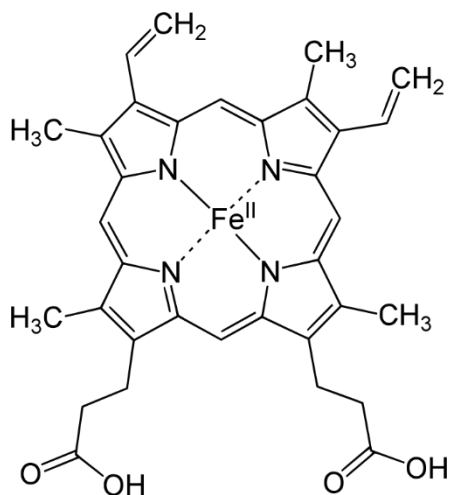


Figure 1.2 Structure of heme B. Central iron atom is shown in the common 2+ oxidation state.

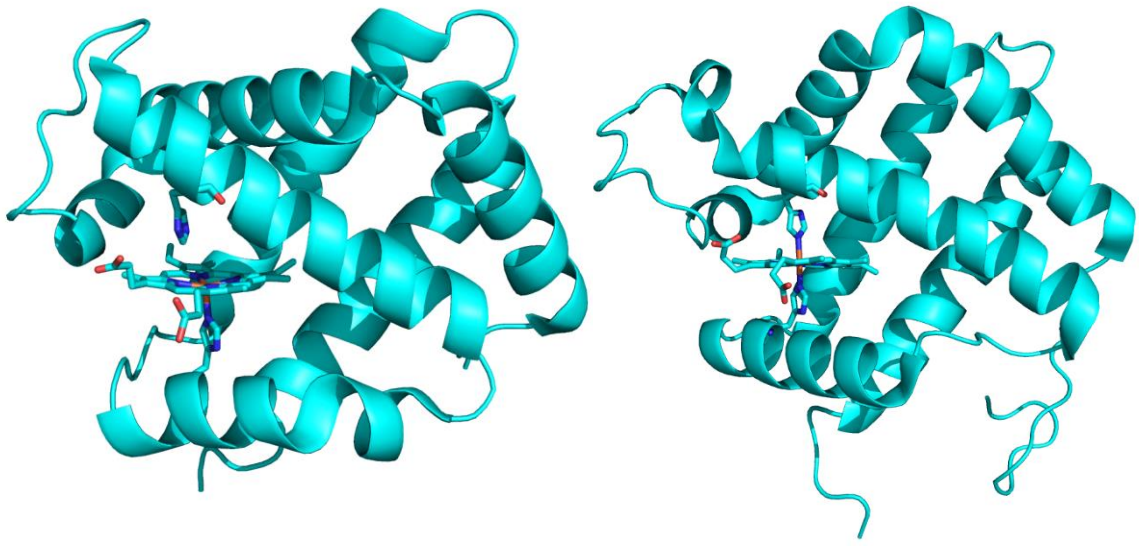


Figure 1.3 Crystal structures of penta-coordinate deoxy-Hb (left, PDB ID: 2DN2) (*125*) and hexa-coordinate rHb1 (right, PDB ID: 1D8U). (*46*)

addition, the heme iron is bound to the protein matrix by a coordination bond with a so-called “proximal” residue located on an α -helix typically designated the F-helix. The most common coordinating residues are histidine (as in Hb, Mb, neuroglobin, etc.) and cysteine (as in the cytochromes P450) (*10*). The heme iron may also be coordinated by a distal residue located on the preceding α -helix, usually the E-helix. The distal residue is most frequently a histidine. Proteins which exhibit coordination of the heme iron solely by the proximal residue are referred to as “penta-coordinate” and proteins which exhibit heme iron coordination by the proximal and distal residues are referred to as “hexa-coordinate” as shown in Figure 1.3. In some proteins the hexa-coordinate state exists in equilibrium with a significant population of protein in the penta-coordinate state. This equilibrium is typical in hexa-coordinate heme proteins which bind gas molecules in which the distal residue must dissociate to allow for binding of the ligand to the heme iron. (*11*)

The nature and dynamics of the protein matrix which constitutes the heme environment are extremely important to the function of any individual heme protein. This impact can be seen in the case of heme proteins involved in electron transfer, such as cytochrome c in the electron transport chain in mitochondria. The redox potential of the heme group in cytochrome c is modulated by the heme environment including the identity of the axial ligand (**I2**) and exposure to solvent (**I3**) in order to facilitate electron transfer between complex III (cytochrome bc₁ complex) and complex IV (cytochrome c oxidase). (**I4**) However, many heme proteins do not carry out electron transport and instead carry out enzymatic reactions or transport and storage of gaseous ligands. Under biological conditions, O₂ and NO are the most common substrates in gas-binding heme proteins. Carbon monoxide (CO) is also able to bind to the heme iron and is commonly used in studies of ligand interaction with heme proteins due to the convenient spectroscopic properties associated with CO-heme adducts, despite the low concentration of CO found *in vivo*. O₂, CO and NO can bind to ferric heme iron (Fe²⁺ oxidation state) while NO can also bind to ferrous heme iron (Fe³⁺ oxidation state).

O₂, CO and NO bind to the heme iron on the distal side, placing them in direct contact with residues in the distal heme pocket – the volume on the side of the heme plane facing the distal residue/E-helix which is directly adjacent to the heme iron. These residues are essential to catalysis of enzymatic reactions as they help to provide a favorable active site geometry and/or participate directly in the reaction. (**2**) For example, in the case of NO dioxygenation in type 1 non-symbiotic hemoglobins (nsHb1), the residue TyrB10 plays an important role in restricting dynamic fluctuations of the distal His, enhancing hydrogen

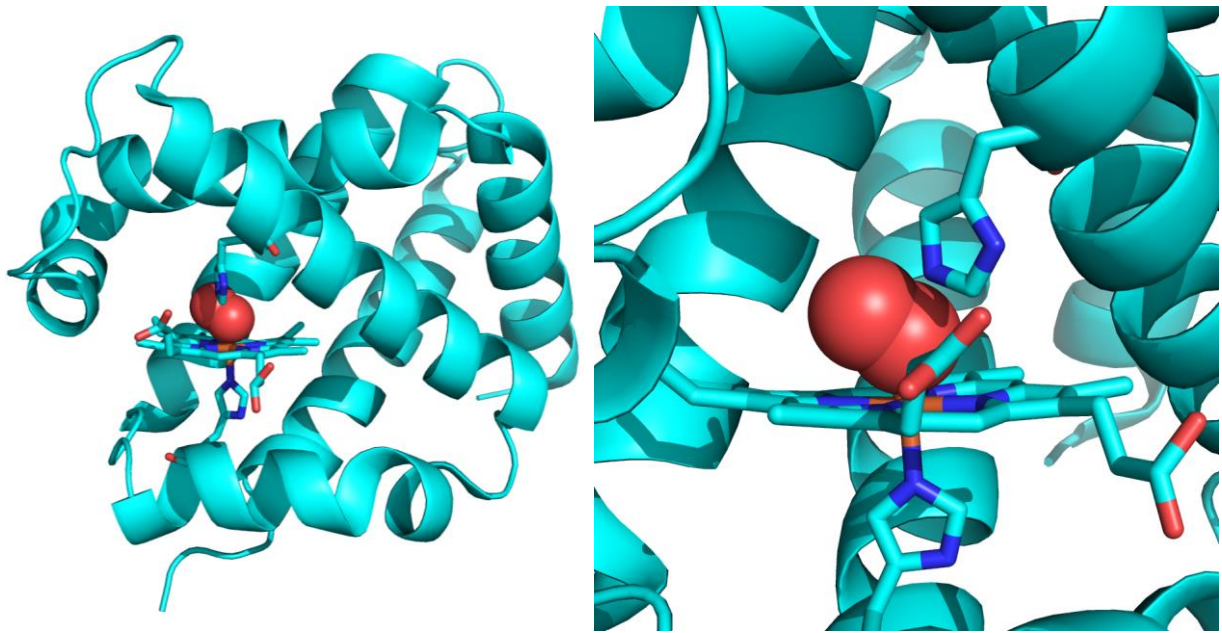


Figure 1.4 (Left) Crystal structure of the α subunit of human oxyHb (PDB ID: 2DN1). (125) (Right) Heme active site of α subunit of human oxyHb showing interaction between distal His and bound ligand.

bonding with the bound ligand and therefore the NO dioxygenase activity of the protein.

(15)

Residues in the distal heme pocket also assist in gas transport and storage. It is well known that the formation of a hydrogen bond with the distal His residue stabilizes O_2 bound to the heme iron in both human Hb (Figure 1.4) and Mb and modulates the affinity of the protein for gaseous ligands. (16) (17) The binding of allosteric effectors also plays an important role in the control of ligand affinity in heme proteins. An allosteric effector is typically a small molecule which binds in a specific location on the protein away from the active site and exhibits an impact on its activity. The decrease of O_2 affinity of human Hb by binding of 2,3-bisphosphoglycerate (2,3-BPG) is a well-known example. (18) The exact mechanism by which allosteric effectors impact the ligand affinity of Hb and other heme proteins has been intensely studied over the past several decades. The model originally described by Perutz (19) incorporating the theory of Monod, Wyman, and Changeux (20)

is often used to explain cooperative binding of ligands and the impact of allosteric effectors on human Hb. In the MWC/Perutz model, a change of the equilibrium between the high-affinity R and low-affinity T quaternary states of the protein as ligands bind to successive subunits is responsible for cooperative binding; allosteric effectors act by modulating this equilibrium.

The MWC/Perutz theory is unable to account for the impact of certain exogenous allosteric effectors such as bezafibrate (**21**) and 2-[4-(3,5-dichlorophenylureido)phenoxy]-2-methylpropionic acid (L35) (**22**) which have been demonstrated to lower ligand affinity without affecting the quaternary state of human Hb. (**23**) These same exogenous allosteric effectors can also exhibit their effect on human Hb dimers which do not retain the native quaternary structure, (**24**) a finding in direct contradiction with the MWC/Perutz model. Newer models have been developed including the tertiary two-state (**25**) and global

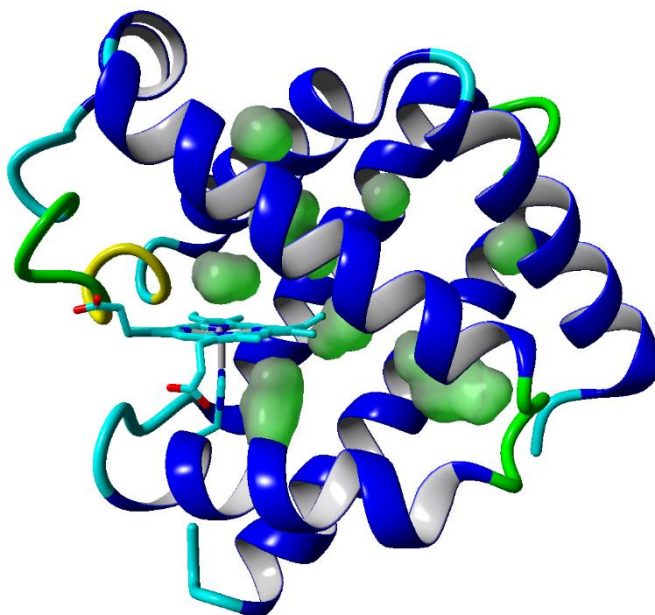


Figure 1.5 Cavities determined in the crystal structure of deoxy-Mb (PDB ID: 1A6N) (**162**) using a probe radius of 1.4 Å.

allostery (23) models which aim to account for these observations. Both models focus on the contributions of tertiary structure and structural dynamics to the observed impacts of effectors, both endogenous and exogenous on ligand-binding in proteins which exhibit cooperativity and allostery.

Accessibility of gaseous ligands to the heme active site is crucial to the activity of gas-binding heme proteins. In Hb, (16) Mb, (26) nsHb1 from *Arabidopsis thaliana* (27) and others, migration of gaseous ligands into the heme active site occurs through the distal His gate. Dynamic fluctuation of the sidechain of the distal His residue can transiently allow direct access of ligands to the heme iron. (16) Protonation of the residue can also force the side chain to adopt an “open” conformation, greatly enhancing accessibility of ligands to the heme iron. (26) However, gaseous ligands may enter the heme active site in other ways. Hydrophobic cavities in the protein matrix may also serve as pathways for ligand migration between the active site and the solvent. (28)

Hydrophobic cavities (Figure 1.5) are a common feature in globular proteins and are often referred to as Xe cavities because of their characterization by crystallization in the presence of high concentrations of xenon gas. (29) By facilitating ligand migration into the active site, these cavities enable a heme protein’s enzymatic activity or role in gas storage and transport. (30) Access of ligands to these cavities can be controlled by structural dynamics of the protein; (31) residue side chains may transiently move to block access to a cavity, or large-scale “breathing” motions of the protein may affect the distance between adjacent secondary structural elements, opening or collapsing a cavity between them. The importance of structural dynamics in in this regard highlights the importance of time-

resolved spectroscopic and computational studies as opposed to analysis of static structures in determining ligand migration routes which are critical for protein activity. Characterization of the migration of gaseous ligands between the bulk solvent, hydrophobic cavities, and the heme active site is essential to understanding the biological role of proteins.

In the first three chapters of this dissertation, I characterize the energetics and structural changes associated with ligand migration within a variety of heme proteins including human Hb, rice type 1 non-symbiotic hemoglobin (rHb1), and fHbs from *Cupriavidus necator* (FHP) and *Staphylococcus aureus* (HMP_{sa}) using calorimetric, spectroscopic and computational techniques. Photoacoustic calorimetry and transient absorption spectroscopy were used to determine kinetic and thermodynamic parameters associated with both photorelease of O₂ and CO from, as well as O₂ and CO rebinding to, the aforementioned heme proteins. In the case of rHb1 and fHbs, classical molecular dynamics simulations were used in combination with the calorimetric and spectroscopic data to develop a complete molecular description of ligand migration and structural changes occurring within the proteins after photolysis of the iron-ligand bond.

In the final chapter, I present thermodynamic and kinetic parameters resolved for the protonation and partial formation an intercalated motif (i-motif) in a DNA oligonucleotide using PAC in combination with a 2-nitrobenzaldehyde pH-jump technique. The oligonucleotide (5'-[CCCTAA]₃CCC-3') was chosen to mimic the sequence of the human telomeric repeat, which may form the i-motif structure *in vivo*. (32) The i-motif has also been predicted to form in other regions of the genome, including the promoter region of

the oncogene c-MYC (33). Understanding the nature of i-motif folding is therefore essential to understanding its function within the human genome.

2 MATERIALS AND METHODS

2.1 Materials

Rice type 1 non-symbiotic hemoglobin was expressed recombinantly in *Escherichia coli* BL21 cells according to the protocol in section 2.2.1. Human adult hemoglobin was obtained from Sigma-Aldrich, Inc. Fe(III)meso-tetra(4-sulfonatophenyl)porphine chloride (Fe[III]4SP) was obtained from Frontier Scientific and was used as received. 2-[4-(3,5-dichlorophenylureido)phenoxy]-2-methylpropionic acid (L35) was synthesized as described by Lalezari. (22) Inositol hexakisphosphate (IHP) was obtained from Sigma-Aldrich as a calcium salt and used without further purification. Synthetic oligonucleotide replicating the telomeric repeat sequence (5-[CCCTAA]₃CCC-3') (iDNA) was obtained from Integrated DNA Technologies and used without further purification. 2-nitrobenzaldehyde (2-NBA) was purchased from Sigma-Aldrich. All other compounds were obtained from Sigma-Aldrich unless otherwise noted.

2.2 Methods

2.2.1 Recombinant expression of rice type 1 non-symbiotic hemoglobin wild-type and H73L mutant

Competent *E. coli* BL21 cells were transfected with plasmids containing genes for ampicillin resistance and the sequence of either His-tagged rice type 1 non-symbiotic hemoglobin wild-type (WT) or His-tagged rice type 1 non-symbiotic hemoglobin H73L

mutant. Transfected cells were cultured on agar plates containing 100 mg/L of ampicillin. A single colony was selected and placed in 100 mL of autoclaved Terrific Broth (TB) medium, placed in an orbital shaker (Thermo Scientific MaxQ SHKA4000) set to 37 °C with a rotation rate of 250 RPM and allowed to grow to saturation over approximately 20 hours. Shaker flasks were prepared containing 1 L of autoclaved TB medium, 100 mg/L of ampicillin and 175 mg/L of δ -aminolevulinic acid. 8 mL of saturated cell solution was used to inoculate each of these 1 L flasks.

One liter flasks were placed in the shaker at 37 °C with rotation at 250 RPM until the optical density of the cell solution reached 1.0 at 600 nm, as determined by UV-vis spectrophotometry. This typically took approximately 3 hours. At this point 1 mL of 500 mM isopropyl β -D-1-thiogalactopyranoside (IPTG) stock solution was added to each flask to induce protein expression. Cells were allowed to incubate in the shaker at room temperature (~18 °C) with rotation at 250 RPM for 16 hours after which the cells were collected by centrifugation at 4000 RPM for 50 mins (Thermo Scientific Sorvall 16R). Cells were suspended in lysis buffer (50 mM tris HCl, 0.5% w/v Triton X-100, 0.2% w/v Tween 20, 0.5 mM dithiothreitol, 10% w/v glycerol, 1 mM ethylenediaminetetraacetic acid [EDTA], pH = 8.0) with a small amount of DNase and lysozyme (~0.1 g). Phenylmethane sulfonyl fluoride (PMSF) was also added to a final concentration of 0.5 mM. Cell solution was sonicated extensively (Fisher Scientific Sonic Dismembrator Model 100) while on ice to rupture *E. coli* cells and allow for recovery of the overexpressed protein. In some cases, cells were exposed to multiple freeze-thaw cycles by being moved between the -40 °C freezer and 4 °C refrigerator to increase the degree of cell rupture. Cell lysate was

centrifugated at 10,000 RPM for 50 minutes (Beckman-Coulter Allegra 64R) to separate soluble and insoluble cell components. If any red color (unrecovered rice hemoglobin) was observed in the pelleted insoluble components, the solid was resuspended in lysis buffer and sonicated further to increase protein recovery.

Cell lysate was run on a chromatographic column containing Ni-NTA resin (Qiagen Ni-NTA Superflow) to collect His-tagged rice hemoglobin WT or H73L mutant proteins (34). The column was flushed with several volumes of imidazole solution (imidazole, 50 mM tris HCl, 100 mM NaCl, pH = 8.0) of increasing concentration to remove undesired weakly-binding components from the cell lysate, with 200 mM imidazole solution fully eluting the purified protein. For the WT, concentrations of 5, 20, 40, 100, and 200 mM imidazole were used. For the H73L mutant, concentrations of 5, 40, and 200 were used. The 200 mM imidazole solution eluent was collected in 1 mL fractions until UV-vis spectra of the fractions resulted in an absorbance at 280 nm of less than 0.01 with a 1 cm path length.

The ratio of the Soret absorbance peak (~400 nm) to the absorbance peak for aromatic residues within the protein – referred to as the R_Z value – was determined for all fractions collected. Fractions with an R_Z value below ~1.5 for the WT and ~1.0 for the H73L mutant were discarded. Remaining fractions were concentrated via ultracentrifugation (Millipore Amicon Ultra-4, 10,000 kDa cutoff) at 4400 RPM for 15 minutes. Concentrated protein solutions were dialyzed extensively against 20 mM HEPES buffer, pH 7.0 until the concentration of imidazole was below 1 μM. Dialyzed, concentrated protein solutions were stored at -40 °C prior to use.

2.2.2 Photoacoustic calorimetry

Photoacoustic calorimetry (PAC) is a technique used to determine kinetics and thermodynamics for phototriggered processes occurring on nanosecond to microsecond timescales for species in liquid solution. A pulsed laser is used to excite a species in solution which undergoes a photochemical reaction, leading to the formation of a photoacoustic wave which can be detected using a piezoelectric transducer. Photoacoustic calorimetry has been used to characterize phototriggered processes occurring in small molecules including the enthalpy of dissociation of the O-H bond in phenol (35) and formation and decay the triplet metal to ligand charge transfer state in Ruthenium(II) bis(2,2'-bipyridine)(4,4'-dicarboxy-2,2'-bipyridine). (36) Photoacoustic calorimetry has also been used to characterize thermodynamics and kinetics associated with ligand photorelease from a variety of heme proteins including human hemoglobin (37), dehaloperoxidase from *Amphitrite ornata* (38), human cytoglobin (39), and human neuroglobin. (40)

2.2.2.1 Rice hemoglobin PAC procedure

The WT or H73L mutant rHb1 protein was stripped of salts by dialysis against several volumes of 20 mM HEPES buffer, pH 7.0. rHb1 samples were then used immediately or exchanged via ultracentrifugation or dilution into the desired buffer, either 20 mM HEPES containing 0.50 M NaCl at pH 7.0 or 20 mM HEPES buffer, pH 6.0. CO-bound samples (CO-rHb1) were prepared at 30 μ M in a 1 cm x 1 cm or 1 cm x 0.5 cm quartz cuvette. The cuvette was then sealed with a septum cap and purged with argon for

15 minutes. A freshly prepared solution of 1 mM sodium dithionite was used to reduce met-rHb1 to the deoxy form, followed by bubbling with CO to produce CO-rHb1. Formation of CO-rHb1 was confirmed by UV-vis spectroscopy using a single beam UV-vis spectrophotometer (Cary50, Varian). The concentration of protein was determined using $\epsilon = 15 \text{ mM}^{-1} \text{ cm}^{-1}$ at 500 nm and $117 \text{ mM}^{-1} \text{ cm}^{-1}$ at 410 nm for met-rHb1 (41).

Instrumentation set-up for PAC was described previously (42). The CO-rHb1 samples were placed in a temperature-controlled holder (TC 125, Quantum Northwest) and a piezoelectric transducer (Panametrics RV103, 1 MHz) was adhered to the side of the sample cell with a thin layer of honey. The photo-cleavage of the Fe-CO bond was initiated by the 532 nm output of an Nd:YAG laser (Surelite I-10, Continuum). The laser power was adjusted using neutral density filters to $\sim 25 \text{ }\mu\text{J}$ to prevent multi-photon absorption. The acoustic signal was amplified using an ultrasonic preamplifier (Panametrics 5662) and collected by a digital oscilloscope (Wave Surfer 42Xs, LeCroy). Typically, 45 traces were averaged at each temperature in the range of 7 - 35°C. Fe(III)4SP was used as a reference compound. Reference traces were measured under conditions identical to those for the sample.

2.2.2.2 Human hemoglobin PAC procedure

Human adult hemoglobin was solubilized in 20 mM HEPES buffer, pH 7.0 and stripped of inorganic phosphates using a Sephadex G-25 column followed by intensive dialysis against 20 mM HEPES buffer, pH 7.0. Oxyhemoglobin (oxyHb) samples were prepared by placing 30 μM stripped Hb in a 1 cm x 1 cm quartz cuvette. The sample cell was then sealed with a septum cap and purged with Ar for 15 minutes. A freshly prepared solution of sodium

dithionite (1 mM) was used to reduce metHb to deoxyhemoglobin (deoxyHb). The sample was then bubbled with air to form oxyHb. Formation of oxyHb was confirmed by UV-vis spectroscopy (Cary50, Varian). The solubility of O₂ in water at 25 °C is 269 μM. (43) The allosteric effectors L35 and IHP were added to Hb samples at the final concentration of 0.50 mM and 1.60 mM, respectively. Fe(III)4SP in 20 mM HEPES buffer, pH 7.0 was used as a reference compound in PAC measurements. Reference traces were measured under conditions identical to those for the sample.

2.2.2.3 2-nitrobenzaldehyde & i-motif DNA PAC

For PAC measurements, iDNA was solubilized in deionized water and 2-NBA was added to obtain a final iDNA and 2-NBA concentration to be 30 μM and 1 mM. The pH of the sample solution was adjusted by addition of a small amount of NaOH or HCl. All samples were freshly prepared and stored in the dark to prevent unwanted photolysis. A 500 μL aliquot of the sample solution was added to a 1 cm x 0.5 cm quartz cuvette (Starna Cells) and the cuvette was placed into a temperature-controlled sample holder with magnetic stirring capability (TC 125, Quantum Northwest). The photochemical reaction of 2-NBA was triggered by a 355 nm output of a pulsed laser (500 μJ, Surelite I-10, Continuum). A piezoelectric transducer (Panametrics V103, 1 MHz) was adhered to the side of the cuvette and the signal was amplified using an ultrasonic preamplifier (Panametrics 5662). Data were recorded by a digital oscilloscope (Wave Surfer 42Xs, LeCroy). The sample solution was stirred during measurements to prevent accumulation of the photoproduct and a fresh aliquot was used for each temperature measurement.

Fe(III)4SP solubilized in deionized water of pH 7.0 was employed as a reference compound. The absorbance of the reference solution matched the absorbance of the sample at the excitation wavelength of 355 nm.

2.2.2.4 PAC data analysis

The amplitude of the photoacoustic wave is proportional to the phototriggered volume change in the solution that consists of a sum of two contributions: a thermal expansion of the solvent (ΔV_{th}) and the non-thermal volume change ($\Delta V'$) as described in Equation 2.1:

$$S=KE_a(\Delta V_{th}+\Delta V') \quad (2.1)$$

where K is the instrument response constant and E_a is the number of Einsteins absorbed. For ligand photorelease from heme proteins, $\Delta V'$ reflects changes in protein conformation, protein solvation, and electrostriction of solvent molecules. For the formation of DNA structural motifs, $\Delta V'$ reflects changes in the conformation of the nucleic acid strand as well as reorganization of solvent molecules. ΔV_{th} is proportional to the amount of heat (Q) released into the solution according to Equation 2.2:

$$\Delta V_{th}=Q \left[\frac{\beta}{C_p \rho} \right] \quad (2.2)$$

where $\beta/C_p \rho$ is a temperature dependent factor consisting of the thermal expansion coefficient (β), heat capacity (C_p), and density (ρ) of the solvent.

In order to determine reaction volume and enthalpy change, photoacoustic traces for a reference compound which decomposes all absorbed energy by non-radiative decay and does not undergo any photochemical conversion are measured under conditions identical to those for the sample. Fe(III)4SP was used as the reference compound for all PAC studies in this dissertation. The amplitude of the reference acoustic wave can be written as:

$$R = K E_a E_{hv} \left[\frac{\beta}{C_p \rho} \right] \quad (2.3)$$

where E_{hv} is the energy of photon at the pump wavelength. In the experiments presented herein pump wavelengths of 532 nm (53.78 kcal mol⁻¹) and 355 nm (80.59 kcal mol⁻¹) are utilized. The reaction enthalpy (ΔH) and volume change (ΔV) are related to Q and $\Delta V'$ respectively, according to Equations 2.4 and 2.5:

$$Q = E_{hv} - \Phi \Delta H \quad (2.4)$$

where Φ is a function of the quantum yields of photo-induced processes occurring within the PAC timescale. In the case of ligand photorelease from heme proteins, Φ is equal to the bimolecular quantum yield (Φ_{bm}) when all observed ligand migration processes occur within the lower limit of resolution of the instrumentation. For the formation of DNA structural motifs, Φ is a function of the degree of formation of the structural motif and any coinciding photochemical processes, including photolysis of 2-NBA.

$$\Delta V' = \Phi \Delta V \quad (2.5)$$

Combining Equations 2.1 – 2.5, the ratio of the acoustic signal for sample and reference can be expressed as:

$$E_{\text{hv}}(\phi-1)/\Phi = \Delta V \left[\frac{C_p \rho}{\beta} \right] - \Delta H \quad (2.6)$$

In this equation ϕ is the ratio of the amplitudes of the sample and reference acoustic traces. Plotting $E_{\text{hv}}(\phi-1)/\Phi$ versus $C_p \rho / \beta$ produces a linear plot with a slope corresponding to ΔV and an intercept corresponding to $-\Delta H$.

For kinetic processes with measurable enthalpy and/or volume changes that take place between the lower and upper limits of resolution of our instrumentation (~50 ns and 10 μ s), a shift in phase between the sample and reference acoustic traces is observed. The combined volume and enthalpy changes for the fast process or processes that occur within the lower limit of resolution of the instrument (< 50 ns) can be determined. For subsequent processes that take place between the lower and upper limits of resolution (50 ns – 10 μ s), the time constant and associated volume and enthalpy changes can be determined. In such case, the sample trace is modeled as a convolution of the reference trace and an exponential function that describes the time profile of the volume change according to Equation 2.7:

$$S(t) = R(t) * \sum \phi(i)^{-t/\tau(i)} \quad (2.7)$$

where $S(t)$ and $R(t)$ are the modeled sample acoustic trace and reference acoustic trace, respectively, the asterisk represents convolution of the photoacoustic traces, and $\phi(i)$ and $\tau(i)$ are the pre-exponential factors and decay constants for each exponential. The volume and enthalpy change for the fast process (ΔV_1 and ΔH_1) are obtained by plotting ϕ_1 as a

function of $C_p\rho/\beta$ according to Equation 2.6. The reaction enthalpy change for the slow process relates to the amount of heat deposited to the solution according to Equation 2.8:

$$\Delta H_2 = -\frac{Q}{\Phi} \quad (2.8)$$

Thus the ratio of the sample and reference acoustic signal for the slow phase can be expressed as a function of the temperature dependent factor using Equation 2.9 and the reaction volume and enthalpy change for the slow process can be extrapolated from the linear plot of $E_{hv}\phi_2$ versus $C_p\rho/\beta$. Here, the value of Φ is dependent on the nature of the photoprocesses occurring between the lower and upper limits of resolution of the instrumentation. In the case of CO escape from rHb1 at pH 6.0, Φ is equal to Φ_{bm} to account for CO molecules which undergo geminate rebinding instead of escaping the protein matrix.

$$\frac{E_{hv}\phi_2}{\Phi} = -\Delta H_2 + \Delta V_2\left(\frac{C_p\rho}{\beta}\right) \quad (2.9)$$

The photoacoustic traces for all experiments in which a shift between sample and reference acoustic tracers were observed were deconvoluted using Sound Analysis 1.50D software (Quantum Northwest).

2.2.3 Time-resolved transient absorption spectroscopy

2.2.3.1 Properties of ligand rebinding in heme proteins

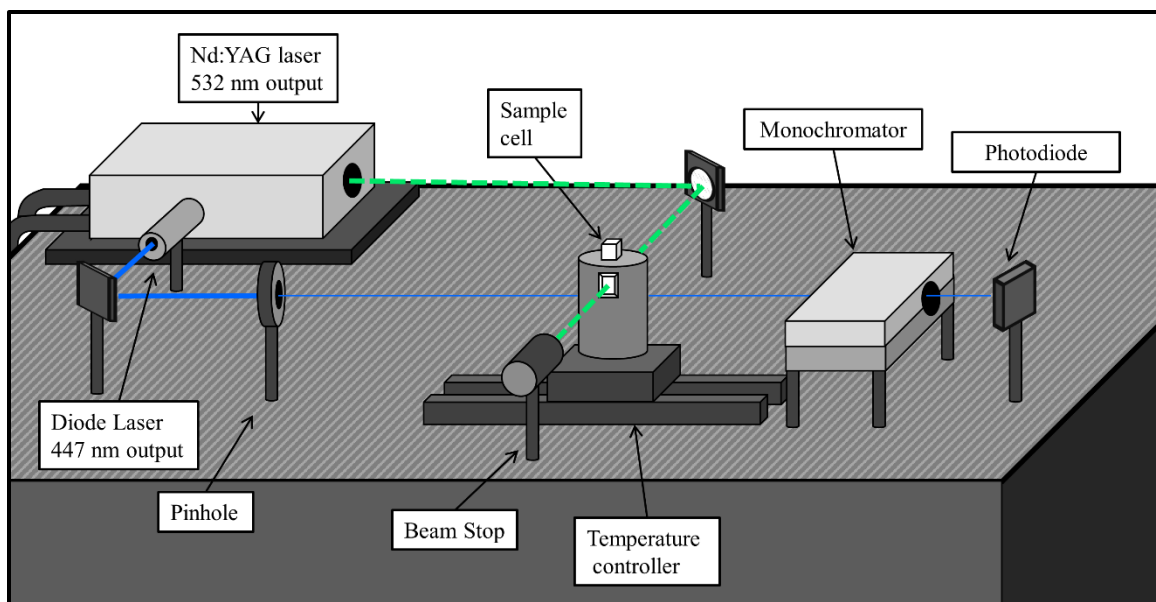


Figure 2.1 Instrument setup for TA studies of ligand rebinding to heme proteins.

Kinetics and quantum yields for bimolecular rebinding of O₂ and CO were measured using a home-built transient absorption instrument. The instrument setup is shown in Figure 2.1. Samples were placed in a 1 cm x 0.2 cm quartz cuvette. Photo-dissociation of the Fe-O₂/Fe-CO bond was achieved using the 532 nm output from an Nd:YAG laser (7 ns pulse, Surelite I-10, Continuum). The probe beam, a 447 nm diode-pumped solid state laser (MDL-III-447, Changeun New Industries Optoelectronics Tech Co. Ltd.), was propagated through the center of the cell perpendicular to the pump beam and through a monochromator (Jobin-Yvon H20). The changes in the probe beam intensity were detected using an amplified photodiode (PDA 10A, Thorlabs). Traces were recorded and stored in a digital oscilloscope (Wave Surfer 42Xs, 400 MHz).

Kinetics for bimolecular rebinding of O₂ and CO to heme proteins was determined by multi-exponential fitting of transient absorption traces using Origin Pro 8 (OriginLab Corp.). The quantum yield for the bimolecular rebinding of O₂ or CO (Φ_{bm}) was determined by comparison to a reference compound according Equation 2.10:

$$\Phi_{bm} = \frac{\Delta A_S \Delta \epsilon_R \Phi_{ref}}{\Delta A_R \Delta \epsilon_S} \quad (2.10)$$

where ΔA_S and ΔA_R are the change in absorbance occurring at the probe wavelength (447 nm) as a result of photolysis of the iron-ligand bond for the sample and reference compounds, $\Delta \epsilon_S$ and $\Delta \epsilon_R$ are the differences between the molar attenuation coefficient (ϵ) for the deoxy and ligand-bound heme proteins at the probe wavelength as determined by UV-vis spectroscopy, and Φ_{ref} is the quantum yield for bimolecular rebinding of the photodissociated ligand to the reference compound. The CO-bound horse myoglobin was used as reference compound because of the high value ($\Phi_{bm} = 0.98$) and temperature independence of the bimolecular quantum yield.

Nanosecond timescale kinetics and quantum yields for O₂ rebinding to human hemoglobin were determined at 25°C using the Ultrafast Systems HELIOS instrument in conjunction with a Ti:Sapphire laser (Coherent Inc.) with a 400 nm output and ~35 fs pulse width. Laser power was <50 nJ. Kinetic traces were analyzed via the maximum entropy method (MEM) using MemExp 4.0 software (44) (45) operating in Simple mode.

2.2.3.2 Characterization of the 2-nitrobenzaldehyde pH-jump

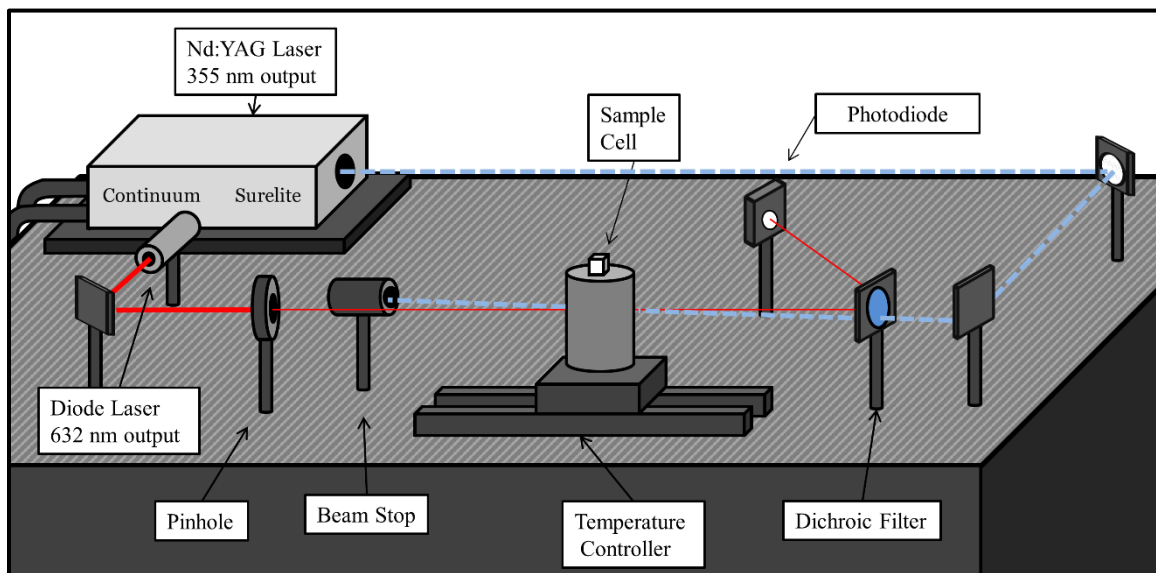


Figure 2.2 Instrument setup for characterization of 2-nitrobenzaldehyde pH-jump using TA.

Transient absorption spectroscopy was used to characterize the pH-jump achievable by photolysis of 2-nitrobenzaldehyde (2-NBA) using a pulsed laser operating at 355 nm. 2-NBA was solubilized in deionized water and diluted to a concentration of 1.0 mM. Concentration was confirmed by UV-vis spectrophotometry using values of $\epsilon_{405} = 11.9 \text{ M}^{-1} \text{ cm}^{-1}$ and $\epsilon_{366} = 224 \text{ M}^{-1} \text{ cm}^{-1}$. The 2-NBA solutions were protected from ambient light using opaque storage containers to prevent undesired photolysis. Trisodium 8-hydroxypyrene-1,3,6-trisulfonate (pyranine) or 2,6-Dibromo-4-[7-(3,5-dibromo-4-hydroxy-2-methyl-phenyl)-9,9-dioxo-8-oxa-9 λ 6-thiabicyclo[4.3.0]nona-1,3,5-trien-7-yl]-3-methyl-phenol (bromocresol green [BCG]) was added to the 1.0 mM 2-NBA solution at a concentration of 50 μM . The compounds pyranine and BCG were used to probe the pH of the illuminated within a few microseconds of photolysis of 2-NBA because of their strongly pH-dependent absorption spectra (Figure 2.3).

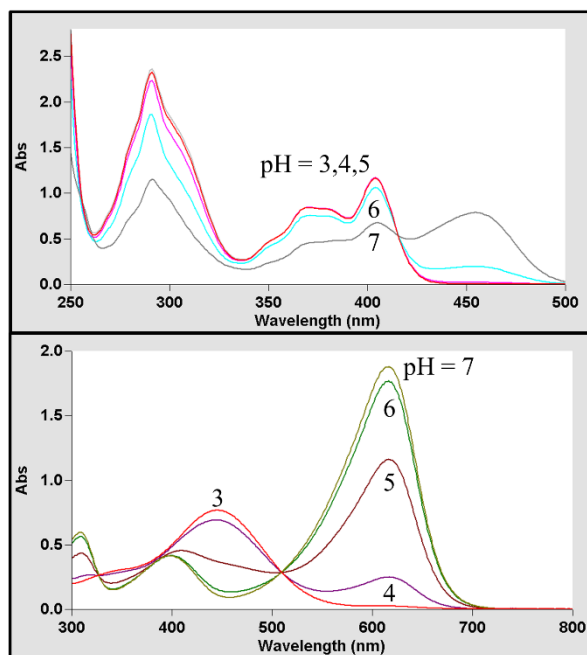


Figure 2.3 (Top) Absorption spectra of 50 μM pyranine in 50 mM sodium phosphate buffer. (Bottom) Absorption spectra of 50 μM bromocresol green in 10 mM sodium phosphate buffer.

The setup of the transient absorption instrument is shown in Figure 2.2. The sample solution containing pyranine/2-NBA or BCG/2-NBA was placed into a 1.0 cm x 0.4 cm quartz optical cell (Starna Cells) in a temperature-controlled sample holder with magnetic stirring capability (TC 125, Quantum Northwest). The probe beam, generated by a 632 nm diode laser (Thorlabs Inc.), was directed through a pinhole and directly through the center of the optical cell. The beam was reflected from a dichroic filter (Thorlabs Inc., additive dichroic filter, blue) into an amplified photodiode (Thorlabs Inc. PDA36A) to allow for measurement of the time profile of the change in beam intensity. The pump beam, a pulsed Nd:YAG laser operating at 355 nm (Continuum Surelite I, 7 ns pulse width) was directed through the opposite side of the dichroic filter and through the center of the sample cell with the illuminated volume of the pump beam overlapping the probe beam.

The value of ϵ for pyranine and BCG at the probe beam wavelength (447 and 632 nm, respectively) was determined as a function of pH (Figure 6.3) from the UV-vis spectra according to the Beer-Lambert law:

$$A = \epsilon cl \quad (2.11)$$

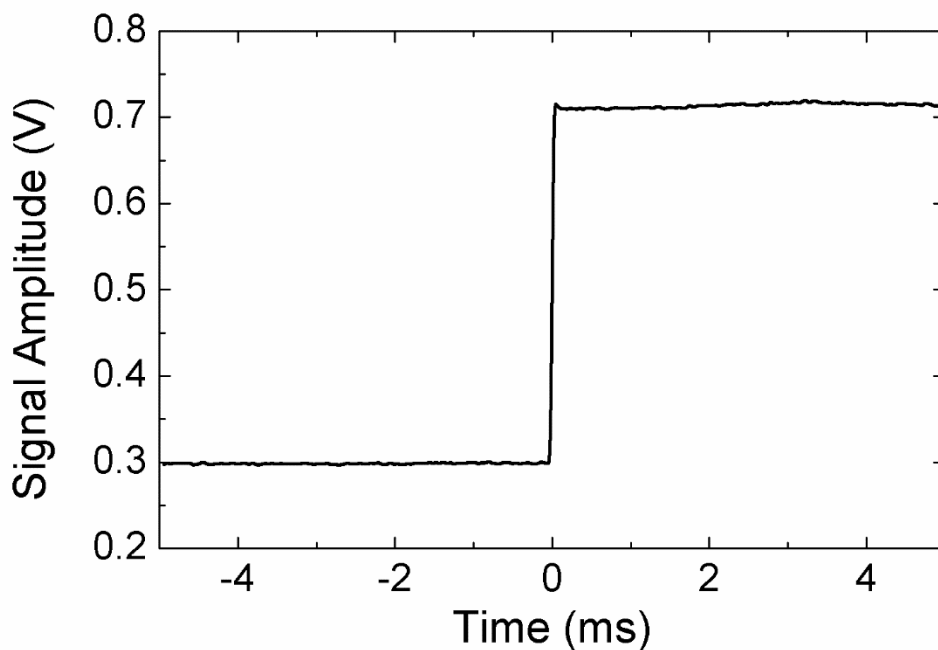


Figure 2.4 Example TA trace for photolysis of 1.0 mM 2-NBA with a total laser power of 15.3 mJ in the presence of 50 μ M bromocresol green in deionized water at 20 $^{\circ}$ C.

where A is the absorbance of the dye at a particular wavelength, c is the concentration of the dye (50 μ M) and l is the path length of the optical cell. A logistic regression was applied to the data to allow for the calculation of pH given a known value of ϵ for pyranine or BCG in a particular solution.

To determine the pH-drop as a result of 2-NBA photolysis, the absorbance before and after the laser pulse were determined from the TA traces (Figure 2.4) according to the following equation:

$$A = \frac{I_t}{I_b} \quad (2.12)$$

where I_t is the intensity of the transmitted light given by the amplitude of the photodiode signal for the sample compound before or after photolysis. I_b is the same quantity for a blank containing only deionized water. I_t and I_b were determined by least-squares fitting of a constant value to the flat portions of the TA trace just before and after the laser pulse at a time of 0 ms. The absorbance was then used to calculate ϵ using the Beer-Lambert law (Equation 2.11) and the logistic fit of the data was used to calculate the pH of the solution within the illuminated volume before and after photolysis.

2.2.4 Circular dichroism spectroscopy

For circular dichroism spectroscopy (CD) measurements, 30 μ M iDNA solubilized in deionized water was placed in 1 mm quartz cuvette. The solution pH values were adjusted by adding a small amount of HCl or NaOH. The spectra were measured using a Jasco J-815 CD spectrometer.

2.2.5 Classical molecular dynamics simulations

Classical molecular dynamics (cMD) simulations of rHb1 WT and H73L as well as CO-bound FHP WT were carried out in order to allow visualization and characterization of side-chain interactions and the formation of transient pockets and channels within the protein structure. Structures of rHb1 WT and H73L mutant proteins free of exogenous

ligands were derived from the crystal structure of 6c rHb1 WT (PDB 1D8U). (46) Structures for CO-rHb1 WT and H73L were produced by homology modeling in YASARA (47) using the amino acid sequence of rHb1 WT and the crystal structure of CN-bound barley nsHb1 as a template (PDB 2OIF) (48) producing a final structure with a Z-score of 0.968. For CO-FHP WT, the crystal structure of FHP containing ketoconazole (PDB: 3OZW) (49) was stripped of exogenous cofactors (FAD, ketoconazole, lipids) and carbon monoxide was added to the heme pocket in close proximity (~ 2.4 Å) to the heme iron using YASARA (47).

Final preparation of the rHb1 simulations including mutation of the distal residue, assignment of His protonation states, solvation in a TIP3P water box with 10 Å margins, and neutralization of the protein system with Na⁺ or Cl⁻ was performed in VMD 1.9.2. (50) In the case of CO-FHP WT, the protein was placed into a cubic water box with 5 Å margins. Classical molecular dynamics (cMD) simulations were carried out in NAMD 2.10 (for rHb1 WT) or NAMD 2.11 (for CO-FHP WT) using CHARMM27 (51) force field parameters on an Intel Core i7-4770 / Nvidia GTX-780 Ti desktop computer running Fedora Linux 23. Systems were first energy minimized, then underwent two rounds of heating and equilibration at before the final cMD production run in the NPT ensemble. Simulations of rHb1 were run for 25 ns for 6c WT and 5c H73L mutant and 30 ns for the 5c WT, CO-bound WT, and CO-bound H73L mutant. All rHb1 simulations excepting the 6c WT were also run with His73 (in WT), His117, and His152 protonated at the δ and ϵ positions becoming positively charged. For brevity we will refer to the cMD simulations where these His residues are protonated as simply “protonated”, and those without as

“deprotonated”. A 10 ns production run of CO-FHP was conducted in the NPT ensemble. The coordinates of the final frame of this simulation were used to generate the initial structure for a simulation in which CO was no longer bound to the heme iron and allowed to move freely within the protein matrix. In addition, a locally enhanced sampling (LES) (52) algorithm was used to duplicate the CO ligand 20 times to allow for the observation of multiple ligand diffusion pathways. A 30 ns production run was carried out for the LES-enabled CO:FHP WT.

General analysis and visualization of the cMD simulations was carried out in VMD 1.9.2. Further analyses of cMD trajectories were performed with MDpocket (53) using a parameter set optimized for detecting transient cavities and channels within the protein interior, similar to that used previously in the analysis of myoglobin. (53)

3 THE ROLE OF IONIC STRENGTH AND PH IN MODULATING THERMODYNAMIC PROFILES ASSOCIATED WITH CO ESCAPE FROM RICE NON-SYMBIOTIC HEMOGLOBIN 1

Reproduced with permission from *J. Phys. Chem. B*, **2017**, *121* (2), pp 351 – 364.

Copyright 2017 American Chemical Society.

3.1 Introduction

Plant hemoglobins belong to a family of heme proteins that are found in most extant species of land plants. They fall into three categories: symbiotic, non-symbiotic, and truncated hemoglobins. (54) Symbiotic (sHb) and non-symbiotic (nsHb) plant hemoglobins maintain the typical 3-over-3 α -helical globin fold found in vertebrate globins such as myoglobin and hemoglobin, while truncated plant hemoglobins exhibit an abbreviated 2-over-2 fold. Plant hemoglobins reversibly bind diatomic gaseous ligands such as CO, O₂, and NO with affinities which reflect their role *in vivo*. For instance, sHbs are essential in the process of transporting oxygen to the symbiotic bacteria known as *rhizobia* which facilitate nitrogen fixation catalyzed by nitrogenase in the root nodules of leguminous plants. sHbs buffer the concentration of O₂ in the root nodule environment, ensuring the optimal O₂ level for the metabolism of *rhizobia* and protection of the nitrogenase active site from oxidation of the iron-molybdenum cofactor. (55) sHbs exhibit a penta-coordinated (5c) heme iron and relatively weak stabilization of the bound exogenous ligand by hydrogen bonding to the distal His; (56) as such they have a K_D for O₂ dissociation of about 48 nM. (57)

NsHbs bind diatomic gaseous ligands, particularly O₂, with a higher affinity than sHbs with $K_D = 1$ nM in *Oryza sativa* (rice) type 1 nsHb (nsHb1) (58) and 1.6 nM for *Arabidopsis thaliana* nsHb1 (59) primarily owing to the low rate constant for O₂ escape. NsHbs are hexa-coordinate (6c) heme proteins much like the vertebrate globins neuroglobin and cytoglobin and unlike the 5c sHbs, vertebrate hemoglobin, and myoglobin. They exhibit much stronger hydrogen bonding between the distal His and bound diatomic ligand than in sHbs, as reported for the CO-bound forms of *A. thaliana* nsHb1 (60) and *Hordeum vulgare* (barley) nsHb1. (61) Interaction of exogenous ligands with the distal His may have a key role in controlling ligand affinity and ligand migration pathways in non-symbiotic hemoglobins.

Ligand migration in type 1 nsHbs has been studied in nsHb1 from *A. thaliana* (60) and rice. (62) The X-ray structures of rice, (46) barley, (48) and corn nsHb1 (PDB 2R50, unpublished) were resolved and indicate that the distal heme pocket of nsHbs share the hydrophobic cavities found in some vertebrate globins such as myoglobin (63) and neuroglobin (64) where the photo-dissociated ligand may temporarily reside before rebinding to the heme iron. This observation is supported by a quantum yield for geminate recombination of about 0.1. (62) Based on the computational model of a ligated structure of rice nsHb1 (rHb1) two different pathways connecting the distal heme pocket to the bulk solvent were proposed. These pathways may be transient and allow for a rapid diffusion of the diatomic ligands out of the protein matrix. They may also provide a pathway by which NO enters the heme pocket, facilitating NO dioxygenase activity in nsHbs. (62) Mutation of residues in the heme environment has a strong effect on ligand escape. PheB10 in nsHbs (corresponding to Phe40 in rHb1) has been shown to modulate hydrogen bonding between

the distal His and bound ligand by restricting the motions of the distal residue. (15) In addition, replacement of the distal His in rHb1 by leucine or alanine increases the quantum yield for geminate recombination (to ~0.22) and allows for much faster bimolecular recombination to the 5c, deligated protein. (62)

Herein photoacoustic calorimetry and time-resolved absorption spectroscopy were used to determine thermodynamic profiles associated with photodissociation of CO from both a wild-type (WT) and a distal histidine mutant (H73L) of rHb1 under stripped conditions, at high ionic strength (0.50 M NaCl) and at pH 6.0. Kinetic parameters for CO rebinding to rHb1 were also determined. Though CO is not the physiological ligand of rHb1, monitoring CO interactions with rHb1 allowed for characterization of the dynamics and energetics of structural changes associated with ligand migration on sub-millisecond timescales as well as the impact of ionic strength and pH on energetics and dynamics of ligand migration processes. In combination with classical molecular dynamics (cMD) simulations, this approach allowed for identification of structural factors that control ligand migration pathways within the family of nonsymbiotic hemoglobins. A mechanism was proposed whereby small changes in pH and/or temperature modulate the rates of ligand migration in rHb1 as well as structural changes associated with the ligand escape from the protein matrix.

3.2 Results

3.2.1 UV-vis spectra

UV-vis spectra for the WT and H73L mutant are shown in Figure 3.1. In the case of the WT, the absorption spectrum of a freshly prepared sample was consistent with the

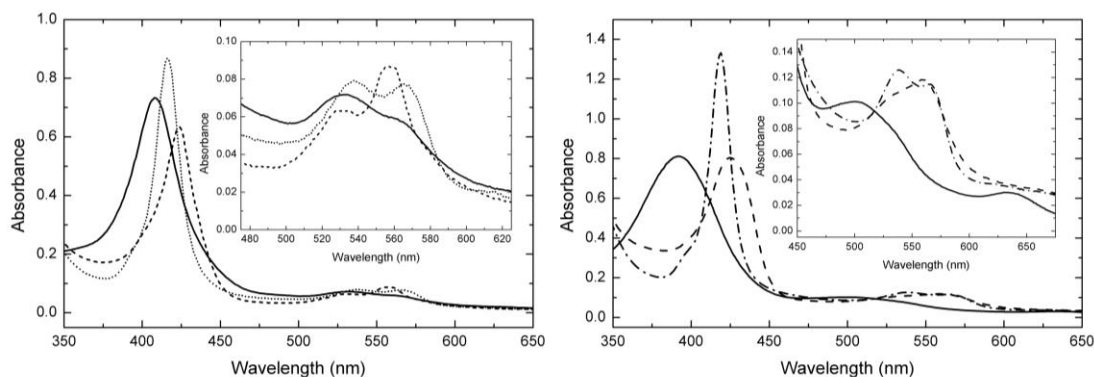


Figure 3.1(Left) Steady-state UV-vis absorption spectra for rHb1 WT in the met form (solid line), deoxy form (dashed line) and CO-bound (dotted line). Conditions: 5 μ M rHb1 WT in 20 mM HEPES buffer, pH 7.5.

(Right) Steady-state UV-vis absorption spectra for H73L rHb1 in the met form (solid line), deoxy form (dashed line), and CO-bound form (dash-dot line). Conditions: 6 μ M rHb1 H73L in 20 mM HEPES buffer, pH 7.5.

formation of the oxy-rHb1 adduct, owing to the extremely high affinity of rHb1 for O₂.

The sample of rHb1 WT in the met form was obtained by oxidizing the heme iron with ferricyanide. The corresponding absorption spectra show the Soret band maximum at 408 nm and two additional Q bands at 532 nm and 562 nm confirming the presence of bis-histidyl coordination in the met form of rHb1 WT. Subsequently, the sample was purged with Ar and reduced by sodium dithionite. The 6c deoxy form of the protein exhibits a Soret band maximum at 426 nm and two pronounced Q bands at 528 nm and 557 nm. In the presence of CO, the Soret band shifts to 417 nm, and two peaks at 537 nm and 566 nm appear as expected for formation of the CO adduct.

The absorption spectrum of the met form of rHb1 H73L exhibits a Soret band maximum at 393 nm and two additional bands of a low intensity at 501 nm and 635 nm characteristic of a 5c high-spin species. The blue shift in the absorption maxima observed for this mutant indicates a decreased polarity of the heme binding pocket. A similar

absorption spectrum was previously reported for His64Ile mutant in Mb. (65) The deoxy form of H73L mutant shows the Soret band at 426 nm and a Q band at 560 nm in agreement with a 5c high-spin heme. The spectrum is similar to that reported previously for a H73L mutant of rHb1. (15) Upon CO association to the H73L mutant, the Soret band shifts to 419 nm and two Q bands are found at 537 nm and 568 nm confirming the formation of a CO bound adduct of the H73L mutant.

3.2.2 Kinetics of CO escape to the surrounding solvent

The energetics and dynamics of structural changes associated with CO photodissociation from rHb1 WT and H73L were monitored under stripped conditions (HEPES buffer, pH 7.0), at high ionic strength (HEPES buffer with 0.50 M NaCl, pH 7.0) and under mildly acidic conditions (HEPES buffer, pH 6.0). The parameters are listed in

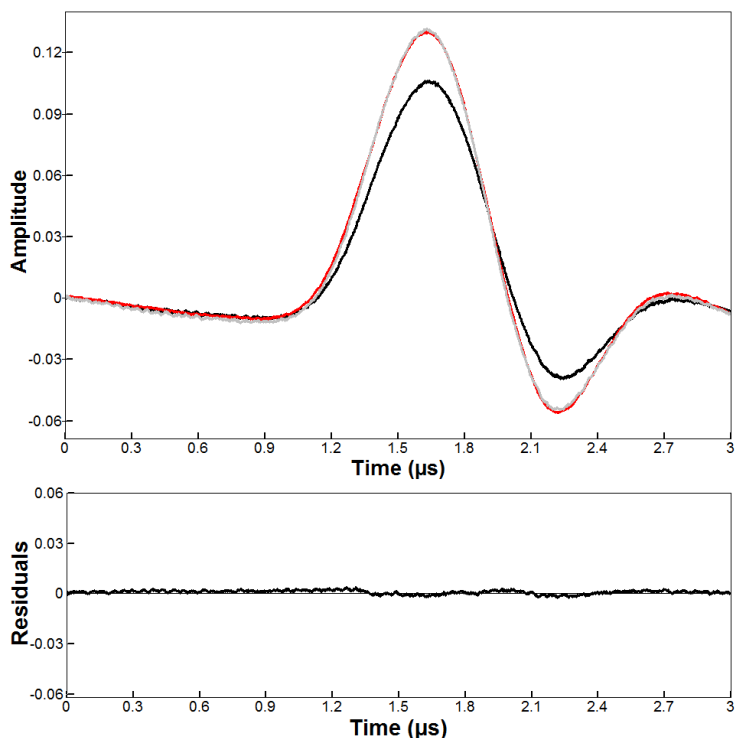


Figure 3.2 PAC traces for CO photorelease from rHb1 WT at pH 6.0 at 12 °C (black line) and heat deposited to the solvent by Fe(III)4SP under same conditions (red line). Simulated trace produced by convolution of component waves in Sound Analysis 1.50D is shown in gray.

Table 3.1. The use of a high ionic strength buffer allows us to estimate the contribution of electrostriction

to the observed volume and enthalpy changes, while monitoring ligand migration under mildly acidic conditions enables probing the role of histidine protonation on the structural changes associated with ligand escape from the heme binding pocket.

The sample photoacoustic traces determined for CO photorelease from rHb1 WT and H73L under stripped conditions and at high ionic strength at pH 7.0 lack a phase shift with respect to the reference trace (data not shown). This indicates that CO escape occurs within the resolution of the instrument (<50 ns). This is consistent with a transient absorption study that reported the time constant for CO escape from rHb1 to be ~14 ns. (62) On the other hand, a phase shift between the sample and reference acoustic traces was

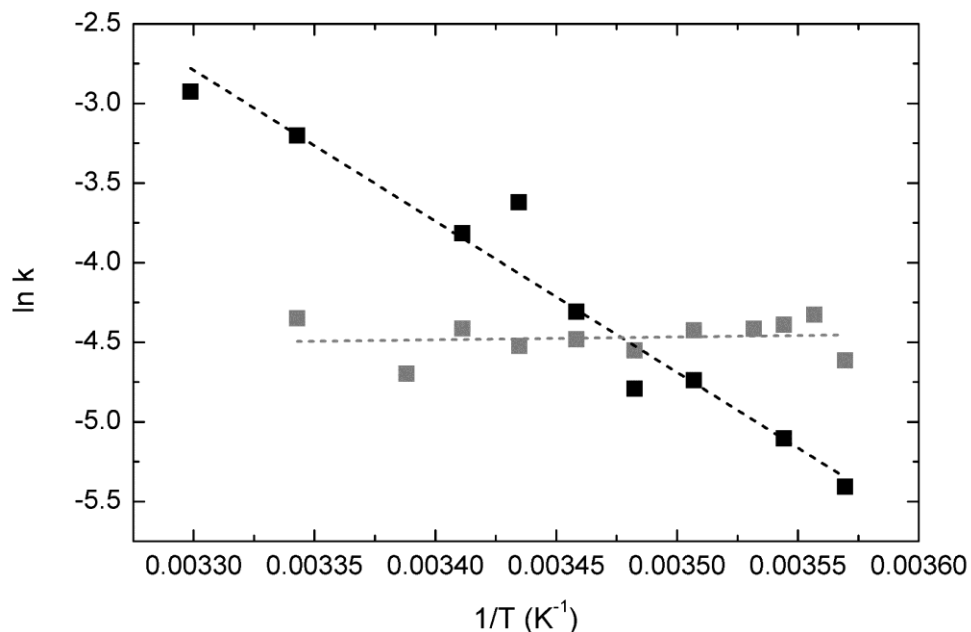


Figure 3.3 Arrhenius plots for CO escape from rHb1 WT (black) and H73L (grey) in 20 mM HEPES, pH 6.0.

observed for CO photorelease from both the WT and H73L mutant at pH 6.0 (Figure 3.3) that indicates slower ligand escape from the protein matrix occurring between 50 ns and

Table 3.1 Observed volume and enthalpy changes associated with photo-dissociation of CO from WT and H73L mutant rHb1.

Conditions		Temp. (°C)	ΔV (mL mol ⁻¹)	$\Delta V_{\text{struc}} + \Delta V_{\text{el}}$ (mL mol ⁻¹)	ΔH (kcal mol ⁻¹)	$\Delta H_{\text{struc}} + \Delta H_{\text{el}}$ (kcal mol ⁻¹)	
WT	Stripped	7 – 14	4.5 ± 0.4	-32.8 ± 0.4	31.1 ± 2.2	8.1 ± 2.2	
		14 – 35	1.2 ± 0.7	-36.1 ± 0.7	6.2 ± 3.3	-16.8 ± 3.3	
	0.50 M NaCl	7 – 35	4.6 ± 0.7	-32.7 ± 0.7	16.0 ± 1.7	-7.0 ± 1.7	
	pH 6.0	Fast	7 – 30	3.5 ± 0.2	3.5 ± 0.2	9.0 ± 2.1	-17.0 ± 2.1
		Slow	7 – 30	-2.2 ± 0.3	-39.5 ± 0.3	-4.8 ± 5.0	-1.8 ± 5.0
		Total	7 – 30	1.3 ± 0.3	-36.0 ± 0.3	5.2 ± 5.0	-18.8 ± 5.0
H73L	Stripped	7 – 35	6.4 ± 1.1	-30.9 ± 1.1	14.5 ± 5.4	-8.5 ± 5.4	
	0.50 M NaCl	7 – 35	11.4 ± 0.3	-25.9 ± 0.3	31.8 ± 1.9	8.8 ± 1.9	
	pH 6.0	Fast	7 – 35	6.1 ± 0.5	6.1 ± 0.5	7.9 ± 5.1	-18.1 ± 5.1
		Slow	7 – 35	9.3 ± 0.6	-27.7 ± 0.4	41.5 ± 6.3	44.5 ± 6.3
		Total	7 – 35	15.4 ± 0.6	-21.6 ± 0.6	49.4 ± 6.3	26.4 ± 6.3

Table 3.2 Thermodynamic and kinetic parameters determined for the PAC slow phase of CO photo-dissociation from CO-rHb1 WT and H73L. Parameters determined using Arrhenius and Eyring plots.

Protein Species	Conditions	τ (16 °C) (ns)	E_a (kcal mol ⁻¹)	ΔH^\ddagger (kcal mol ⁻¹)	$\Delta S^\ddagger * 298 \text{ K}$ (kcal mol ⁻¹)
WT	pH 6.0 HEPES	134 ± 19	18.9 ± 6.6	19.4 ± 6.6	6.8 ± 7.1
H73L	pH 6.0 HEPES	90 ± 15	~ 0 ± 1.1	0.2 ± 1.1	-13.2 ± 1.3

10 μ s. The phase shift observed for the sample acoustic trace with respect to the reference indicates slower ligand escape from protein matrix at pH 6.0. The sample photoacoustic traces were deconvoluted as described in the Materials and Methods section and

corresponding time constants and activation parameters are listed in Table 3.2. Arrhenius plots for the CO escape at pH 6.0 can be seen in Figure 3.3. Ligand escape from the protein matrix at 16 °C occurs with a time constant of 134 ± 19 ns for rHb1 WT and a comparable value of $\tau = 90 \pm 15$ ns was determined for the H73L mutant. A significant activation enthalpy was observed for CO escape from the WT ($\Delta H^\ddagger = 19.4 \pm 6.6$ kcal mol⁻¹) whereas a negligible activation barrier was reported for CO escape from the mutant ($\Delta H^\ddagger = 0.2 \pm 1.1$ kcal mol⁻¹). These data suggest either distinct ligand migration pathways or different conformational changes associated with CO migration in WT and H73L mutant.

3.2.3 Volume and enthalpy changes of CO photorelease from rHb1

For ligand dissociation from heme proteins, the observed reaction enthalpy and volume changes are complex and can be expressed as a sum of several contributions as described the following equations:

$$\Delta H = H_{Fe-CO}^\circ + \Delta H_{struct} + \Delta H_{solv} + \Delta H_{el} \quad (3.1)$$

$$\Delta V = \Delta V_{struc} + V_{CO}^\circ + \Delta V_{el} \quad (3.2)$$

where ΔH_{struc} describes change in enthalpy due to structural changes associated with the transition between the 6c CO-bound and 5c forms of the protein. H_{Fe-CO}° is the enthalpy of the Fe-CO bond which is cleaved upon photoexcitation of the heme group. The determination of this value in heme proteins is complicated somewhat by the contribution of protein structural relaxations to the measured enthalpy for ligand photorelease, (66) but combined MD/DFT calculations on the isolated heme-ligand system (67) seem to match earlier estimates (68) placing the value at 26 kcal mol⁻¹. ΔH_{solv} corresponds to a small

contribution from solvation of the photo-dissociated CO molecule as it leaves the hydrophobic heme pocket (-3 kcal mol^{-1}). (69) ΔH_{el} is a parameter associated with electrostriction of solvent molecules to accommodate charged species which move in or out of contact with the bulk solvent. By determining ΔH in the presence of 0.50 M NaCl electrostrictive contributions to the observed thermodynamic parameters can be estimated. Likewise, the observed reaction volume change contains ΔV_{struc} that accounts for the difference in structural volume between the CO-bound and CO-free states of the protein including hydration of the heme binding pocket. V_{CO}° is the partial molar volume of CO ($37.3 \pm 0.5 \text{ mL mol}^{-1}$) (70), ΔV_{el} is analogous to ΔH_{el} and accounts for the contraction of solvent molecules as they reorient around a charged species.

3.2.4 Temperature dependence of $\Delta H/\Delta V$ for CO escape

The plot of $E_{hv}(\phi-1)/\Phi_{bm}$ vs. C_{pp}/β for CO photodissociation from rHb1 WT under stripped conditions exhibits two distinct linear dependencies with a transition point occurring at a C_{pp}/β value of 7.5 which corresponds to the temperature of 14 °C (Figure 3.4) pointing towards the temperature dependence of the reaction volume and enthalpy. In the low-temperature range ($<14 \text{ }^{\circ}\text{C}$), ligand photorelease occurs with $\Delta H = 31.1 \pm 2.2 \text{ kcal mol}^{-1}$. Accounting for H°_{Fe-CO} (26 kcal mol^{-1}) and ΔH_{solv} (-3 kcal mol^{-1}) gives a value of $\Delta H_{struc} + \Delta H_{el} = 8.1 \pm 2.2 \text{ kcal mol}^{-1}$. Assuming that $\Delta H_{struc} + \Delta H_{el} = -7.0 \pm 1.7 \text{ kcal mol}^{-1}$ measured for ligand dissociation from rHb1 WT in high ionic strength buffer (20 mM HEPES, 0.50 M NaCl, pH 7.0) reflects the enthalpy changes solely due to the structural changes, we can estimate $\Delta H_{el} = 15.1 \pm 2.2 \text{ kcal mol}^{-1}$ for CO photorelease from rHb1 WT under stripped conditions below 14 °C. This endothermic electrostrictive component is

consistent with the decreased exposure of charged residues in the ligand free rHb1, Under stripped conditions at temperatures above 14 °C, $\Delta H = 6.2 \pm 3.3 \text{ kcal mol}^{-1}$ and $\Delta H_{\text{struc}} + \Delta H_{\text{el}} = -16.8 \pm 3.3 \text{ kcal mol}^{-1}$. The increased exothermicity at temperatures over 14 °C is

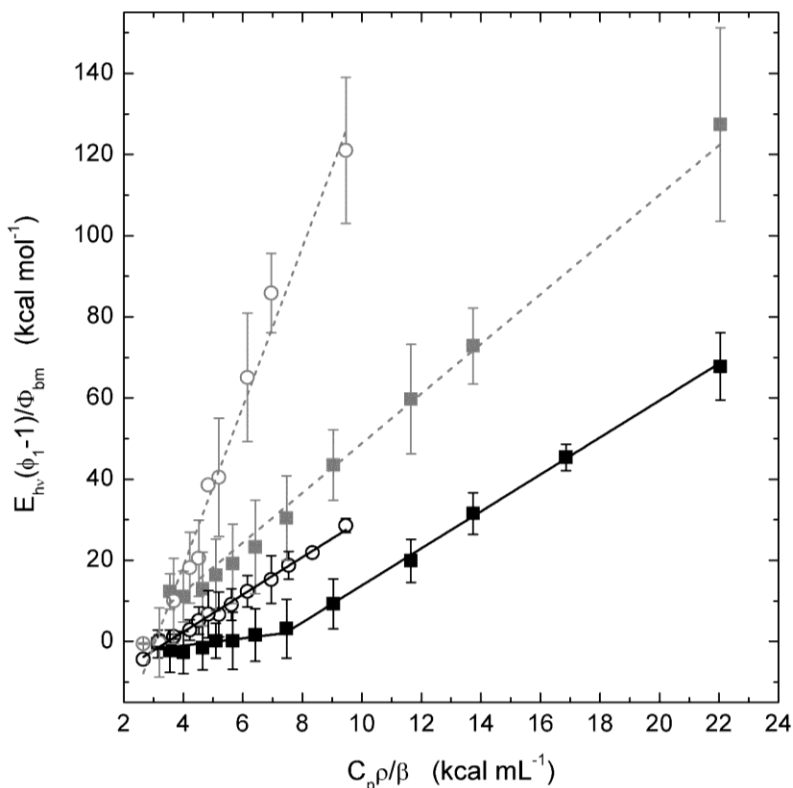


Figure 3.4 Plot of $E_{\text{hv}}(\phi_1-1)/\Phi_{\text{bm}}$ vs. $C_p\rho/\beta$ for CO photorelease from CO-rHb1 WT (black) and H73L (gray) under stripped conditions (squares) and with 0.50 M NaCl (open circles).

consistent with increased solvation of one or more charged residues occurring simultaneously with ligand escape from the protein in the high-temperature range.

The volume change determined below 14 °C is $4.5 \pm 0.4 \text{ mL mol}^{-1}$. This value is identical to that observed for the CO photorelease in the presence of 0.50 M NaCl, suggesting that at low temperature and under stripped conditions the reorganization of the bulk solvent due to electrostriction does not contribute to the observed volume change. Subtracting the partial molar volume of the photo-dissociated CO ligand results in $\Delta V_{\text{struc}+}$

$\Delta V_{el} = -32.8 \pm 0.5 \text{ mL mol}^{-1}$. The observed volume contraction can be associated with the repositioning of the E- and F-helices upon ligand dissociation as evident from the cMD simulations which show a decrease in the distance between the α -carbons of the distal and proximal histidines in the structure of the 5c rHb1 WT compared to the CO-bound protein. The volume contraction may also be indicative of the migration of one or more water molecules into the heme binding pocket following CO release since in the structure of rHb1 a water molecule was found within hydrogen bonding distance of the distal histidine (2.8 Å) and is absent in the structure of CN-bound barley nsHb1. The more negative ΔV_{struc} observed for CO photodissociation from WT rHb1 above 14 °C ($\Delta V_{struc} + \Delta V_{el} = -36.1 \pm 0.7 \text{ mL mol}^{-1}$) is consistent with the increased solvation of charged residue(s) at higher

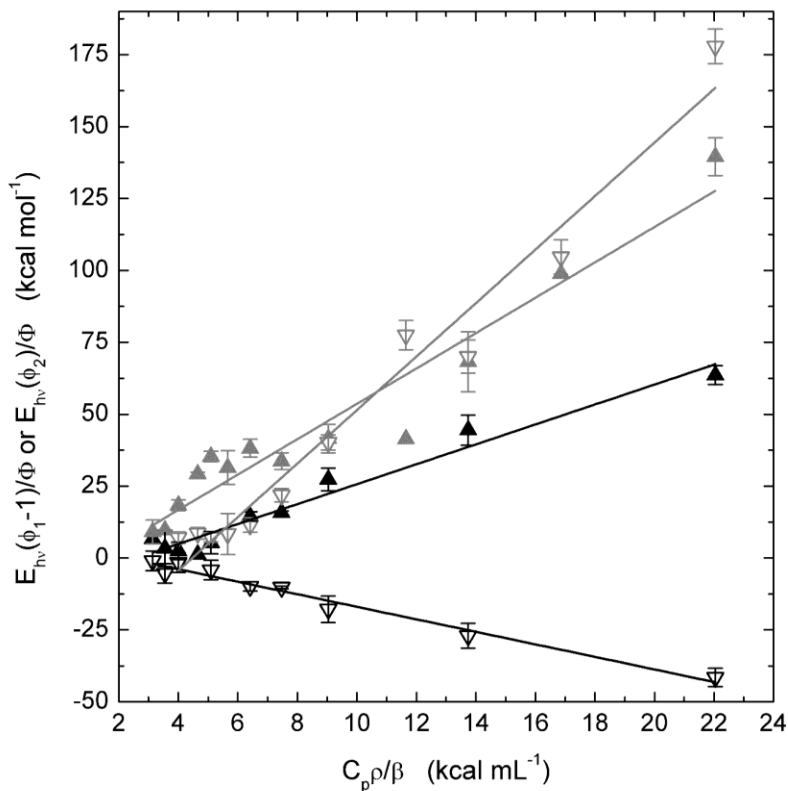


Figure 3.5 Plot of $E_{hv}(\phi_1-1)/\Phi_{bm}$ and $E_{hv}(\phi_2)/\Phi_{bm}$ versus the temperature dependent factor ($C_p \rho / \beta$) for CO photorelease from CO-rHb1 WT (black) and H73L (gray). The data for the fast phase (<50 ns) and slow phase (~50 ns – 10 μ s) are shown as closed triangles and open inverted triangles respectively.

temperature values and/or distinct geometry of the heme binding pocket at increased temperature.

Under mildly acidic conditions (20 mM HEPES, pH 6.0) the temperature dependence of ΔH and ΔV is eliminated (Figure 3.5). Given that the photolysis of the Fe-CO bond occurs within the resolution of our instrument (~50 ns) and that both rebinding of the distal His to the heme iron and bimolecular recombination of CO occur on much longer timescales, (62) the fast process observed at pH 6.0 can be attributed to the photocleavage of the Fe-CO bond and rapid ligand migration within the heme binding pocket. The slow process is consistent with CO escape into the surrounding solvent. Interestingly, the sum of the volume and enthalpy changes for the fast and slow phase observed at pH 6.0 matches well the reaction volume and enthalpy change measured for CO photodissociation at pH 7.0 above 14 °C indicating that overall structural changes coupled to the CO release from the protein are analogous and the decrease in pH impedes the rate of ligand escape from the protein.

In the case of CO photodissociation from the H73L mutant under stripped conditions, the plot of $E_{hv}(\phi-1)/\Phi_{bm}$ vs. $C_p\rho/\beta$ (Figure 3.4) is temperature independent pointing out that the presence of the distal histidine residue is required for the observed temperature dependence of the thermodynamic parameters. The observed volume and enthalpy changes ($\Delta V = 6.4 \pm 1.1 \text{ mL mol}^{-1}$ and $\Delta H = 14.5 \pm 5.4 \text{ kcal mol}^{-1}$) are different from those measured for the CO photodissociation from the WT in the low or high temperature range, suggesting a significant alteration of the overall structure of the CO-bound and/or deoxy form in the H73L mutant. The thermodynamic parameters for ligand

photorelease from the H73L mutant in high ionic strength buffer are also temperature independent with ΔH being $\sim 17 \text{ kcal mol}^{-1}$ more endothermic and ΔV being more positive compared to the H73L mutant under stripped conditions. The sum of the enthalpy changes determined for the fast and slow process of CO photorelease from the H73L mutant at pH 6.0 is endothermic and similar in magnitude to the reaction enthalpy change observed for CO photorelease from H73L at pH 7.0 with 0.50 M NaCl. These data indicate that electrostriction may contribute to the observed $\Delta V/\Delta H$ that occurs in the H73L mutant under stripped conditions, and likely does not occur under mildly acidic conditions.

3.2.5 Kinetics for bimolecular CO rebinding

In addition to characterizing thermodynamic and kinetics parameters for ligand photolysis and escape from CO-rHb1 WT and H73L, we determined kinetics and quantum

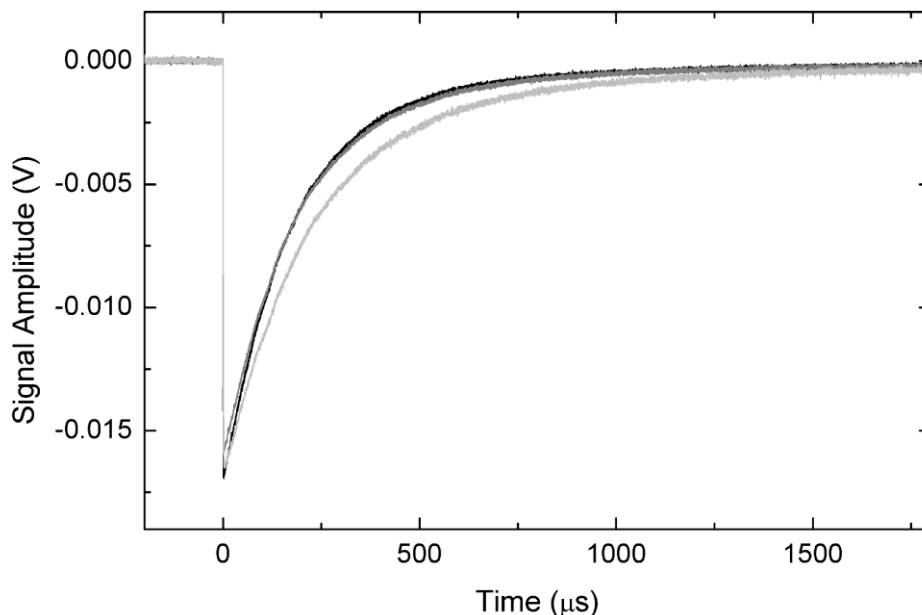


Figure 3.6 Representative TA traces determined for rebinding of CO to deoxy-rHb1 WT under stripped conditions (black), with 0.50 M NaCl (grey) and at pH 6 (light grey) at 20 °C.

yields for bimolecular CO rebinding to 5c deoxy-rHb1. Example TA traces are shown in Figure 3.6. Formation of the 6c species by rebinding of the distal His to the heme iron does not interfere with CO kinetics under experimental conditions used here since it occurs on longer timescales (~ 20 ms). (62) We observe rate constants of $\sim 5 \mu\text{M}^{-1} \text{s}^{-1}$ and $140 \mu\text{M}^{-1} \text{s}^{-1}$ for the rebinding of CO to WT and H73L rHb1 at 20°C , respectively. These kinetic parameters are similar to those previously determined for CO recombination with rHb1 WT. (15) Rate constants and activation parameters for bimolecular recombination are independent of ionic strength or pH decrease as demonstrated in Table 3.3.

The quantum yields measured for bimolecular rebinding (Φ_{bm}) of CO to rHb1 WT and H73L as a function of temperature are shown in supplementary data (Figure 3.7). The temperature dependence of Φ_{bm} was observed previously in other heme proteins such as human hemoglobin. (71) We observe that under stripped conditions Φ_{bm} for bimolecular

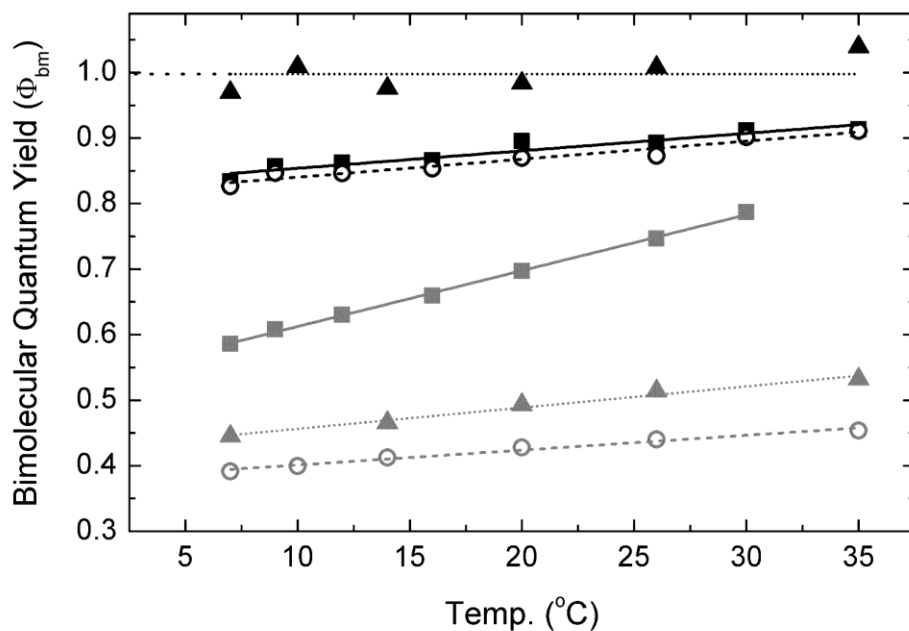


Figure 3.7 Quantum yields for bimolecular recombination of CO to rHb1 WT (black) and H73L (grey) under stripped conditions (squares), with 0.50 M NaCl (open circles), and in pH 6.0 HEPES buffer (triangles).

rebinding at 20 °C is 0.88 for the WT and 0.70 for the H73L mutant. These values are very close to those previously reported by Bisht et al. (62) The small discrepancy between Φ_{bm} for bimolecular rebinding of CO to H73L determined here (0.70 at 20 °C) and that previously measured (~0.78 at 20 °C) is likely due to the different solvent used; 20 mM HEPES instead of the 20 mM phosphate buffer used by Bisht et al. (62) The use of high ionic strength buffer does not significantly affect Φ_{bm} in the WT, while it decreases to 0.42 at 20 °C for the H73L mutant. Mildly acidic conditions have opposite effects on the Φ_{bm} for ligand rebinding in WT and H73L mutant as Φ_{bm} in the WT is increased to unity across the measured temperature range and decreased to 0.49 at 20 °C in the H73L.

Table 3.3 Rate constants and activation parameters determined from Arrhenius and Eyring plots for bimolecular recombination of CO to deoxy-rHb1 WT and H73L. Stripped and 0.50 M NaCl studies were conducted in 20 mM HEPES at pH 7.0.

Protein Species	Conditions	k_{bm} (20 °C) ($\mu\text{M}^{-1} \text{s}^{-1}$)	E_{a} (kcal mol^{-1})	ΔH^{\ddagger} (kcal mol^{-1})	$\Delta S^{\ddagger} * 298 \text{ K}$ (kcal mol^{-1})
WT	Stripped	5.0 ± 0.5	8.5 ± 0.4	8.0 ± 0.4	-8.4 ± 0.4
	0.50 M NaCl	4.7 ± 0.4	9.2 ± 0.2	8.6 ± 0.2	-7.8 ± 0.2
	pH 6.0 HEPES	4.5 ± 0.6	9.1 ± 0.3	8.5 ± 0.3	-7.9 ± 0.3
H73L	Stripped	140 ± 9.0	6.1 ± 0.2	5.6 ± 0.4	-8.9 ± 0.4
	0.50 M NaCl	135 ± 17.0	6.0 ± 0.3	5.4 ± 0.3	-9.1 ± 0.3
	pH 6.0 HEPES	123 ± 2.3	5.5 ± 0.5	4.9 ± 0.5	-9.6 ± 0.5

3.2.6 Classical molecular dynamics simulations

Classical molecular dynamics simulations were carried out on 6c rHb1 WT, 5c rHb1 WT, 5c rHb1 H73L, CO-rHb1 WT, and CO-rHb1 H73L in both the deprotonated and protonated forms. Analysis of the cMD trajectories reveals significant differences in

tertiary structure, side chain orientations/interactions, and the positions and volumes of transient cavities and channels depending on ligation state, distal residue mutation, and histidine protonation (Table 3.4).

The EF region interhelical distance ($r_{\alpha-\alpha}$), determined as distance between the α -carbons of proximal His107 and the α -carbon of the distal residue (His or Leu) and averaged across the trajectories was used to evaluate the changes in the EF region geometry. For the deprotonated 6c WT, 5c WT, and 5c H73L simulations, we observe $r_{\alpha-\alpha}$ values of 12.4, 12.7, and 12.6 Å, respectively. In these forms, positively-charged residues on the E and F helices are able to form salt bridges with the negatively-charged heme

Table 3.4 A selection of data from analysis of cMD trajectories, including average distance between the proximal His and distal residue α -carbons ($r_{\alpha-\alpha}$), average distance between ζ -nitrogen of Lys69 and the heme-6-propionate group carboxyl carbon, and average distance between guanidino carbon of Arg103 and heme-7-propionate group carboxyl carbon. Data derived from then H73L mutant simulations are highlighted in gray. Values of $r_{\alpha-\alpha}$ are presented with standard deviations derived from at least 2000 MD snapshots. Multiple values indicate multiple stable conformations, with approximate percentage of frames in the closer conformation in the last 2000 frames of each simulation given in parentheses.

Species	$r_{\alpha-\alpha}$ (Å)	$r_{K69\text{-propionate}}$ (Å)	$r_{R103\text{-propionate}}$ (Å)
Hexa-coordinate rHb1 WT	12.4 ± 0.2	3.7	4.0
Penta-coordinate rHb1 WT	12.7 ± 0.5	3.6	4.1
Penta-coordinate rHb1 WT with H73, H117, H152 Protonated	12.6 ± 0.5	7.0	4.0
Penta-coordinate rHb1 H73L	12.6 ± 0.5	3.7 (54%) / 8.7 (46%)	4.1
Penta-coordinate rHb1 H73L with H117 & H152 Protonated	12.2 ± 0.6	3.7 (69%) / 7.1 (31%)	4.2
CO-rHb1 WT	14.4 ± 0.3	8.5	7.0 (52%) / 11.6 (31%)
CO-rHb1 WT, H73, H117, H152 Protonated	15.0 ± 0.5	12.0	13.2
CO-rHb1 H73L	12.8 ± 0.4	3.5	3.9 (69%) / 8.4 (31%)
CO-rHb1 H73L with H117 & H152 Protonated	13.1 ± 0.4	3.5 (56%) / 8.2 (44%)	4.1

propionate groups. Residues which form salt bridges with the heme-6-propionate group include Lys69 and Tyr111 while the heme-7-propionate group interacts primarily with Arg103 and Thr107. The residues Lys69 and Arg103 remain within ~ 4 Å of the heme propionates across the entire simulation, close enough to form salt bridges. For the CO-rHb1 WT in the deprotonated and protonated forms, $r_{\alpha-\alpha}$ is increased by 2.0 and 2.6 Å, respectively, compared to the 6c WT. In deprotonated CO-rHb1 WT the increased separation of the E and F helices can be associated with the accommodation of the CO

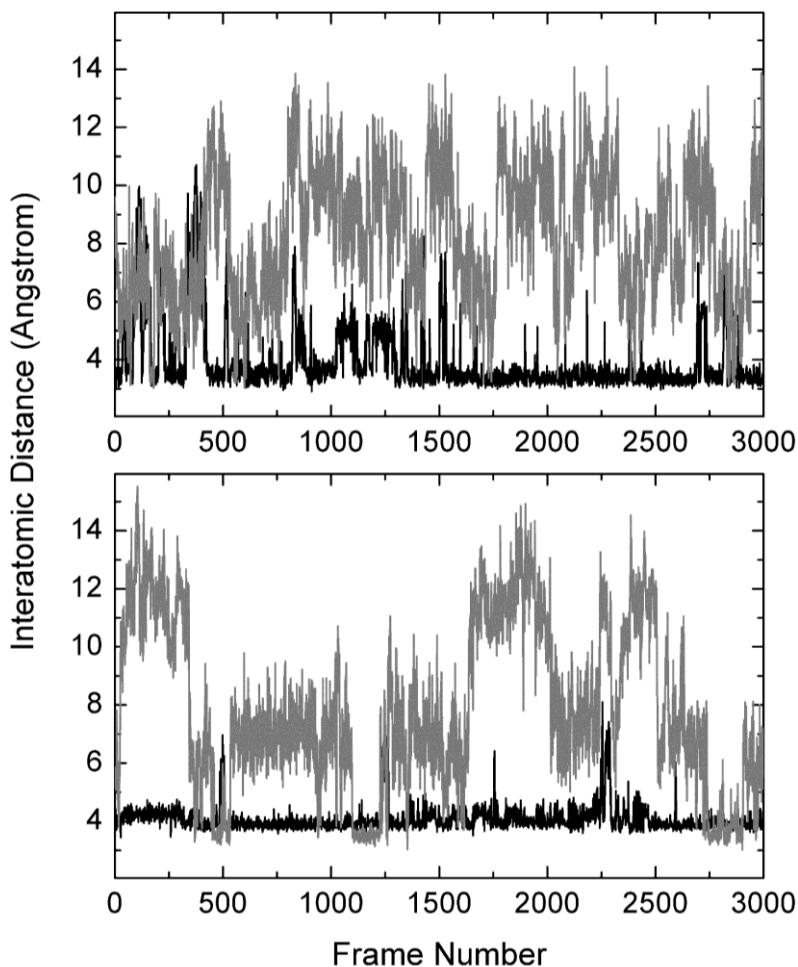


Figure 3.8 Top Panel: Distance between ζ -nitrogen of Lys69 and carboxyl carbon of heme-6-propionate group during cMD trajectory of penta-coordinate WT rHb1 (black line) and CO-rHb1 WT (grey line).

Bottom Panel: Distance between guanidine carbon of Arg103 and carboxyl carbon of heme-7-propionate group during cMD trajectory of penta-coordinate WT rHb1 (black line) and CO-rHb1 WT (grey line).

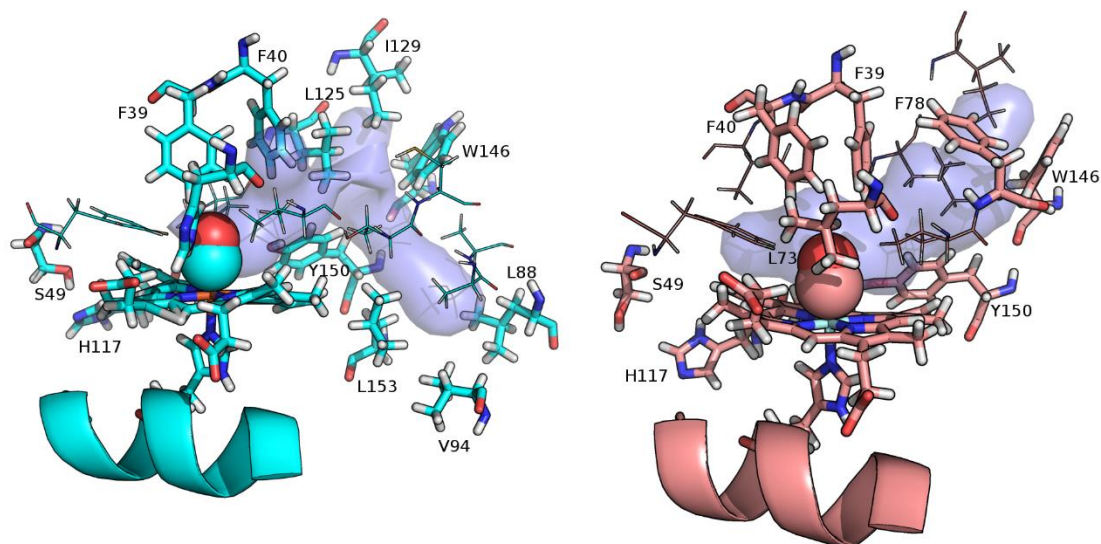


Figure 3.9 Channels determined in MD simulation of deprotonated CO-rHb1 WT (left) and deprotonated CO-rHb1 H73L (right) along with critical residues and an F-helix fragment. Critical residues bordering the channels are shown as stick representations.

ligand in the heme binding pocket and a positioning of the distal His which allows the hydrogen on N_{ϵ} to hydrogen bond with the CO ligand. An analogous increase is observed when comparing the crystal structure of 6c rHb1 WT (PDB: 1D8U) (**46**) with CN-bound barley nsHb1 (PDB: 2OIF). (**48**) In the case of protonated CO-rHb1 WT, the protonated distal His swings out of the heme pocket into a conformation in which the distal His side chain is exposed to the bulk solvent and the CD loop has a different conformation than in the deprotonated protein. Concomitantly, Phe55 and Phe57 move deeper into the distal heme cavity, taking up some of the space vacated by the distal His. In deprotonated CO-rHb1 WT the increased interhelical distance leads to weaker interactions between the heme propionate groups and nearby charged residues allowing Lys69 and Arg103 to adopt more solvent-exposed conformations farther away from the heme propionate groups (8.5 and 7.0/11.6 Å respectively) as shown in Figure 3.8. Lys69 and Arg103 take up further positions in the protonated CO-bound WT (12.0 and 13.2 Å) since the positively-charged

distal His residue repels these positively-charged residues. This idea is supported by the closer interactions of Lys69 and Arg103 with the heme propionate groups in the CO-bound H73L mutant (3.5 and 3.9/8.4 Å), in which the distal residue is neutral and $r_{\alpha-\alpha}$ is smaller.

Further analysis of the cMD trajectories was carried out with the aim of identifying both long-lived cavities and transient channels within the protein structure using Fpocket software (72) and its MDpocket extension. (53) MDpocket analysis of the cMD trajectories for CO-rHb1 WT shows the presence of a channel which leads from the distal heme pocket to the exterior of the protein, passing roughly between the G and H helices (Figure 3.9, Left). The distal heme cavity portion is bordered primarily by Phe39, Phe40, Ile43, Phe54, Val77, and Phe78 while the rest of the channel is surrounded primarily by Leu125, Leu126, and Trp146. An analogous channel is present in CO-bound rHb1 H73L (Figure 3.9, Right). These channels are similar to those previously identified in MD simulations of ligated rHb1 WT and H73L (62) and likely contribute to the fast CO escape from rHb1 (<50 ns) observed with PAC at pH 7.0. Interestingly, the MDpocket analyses of protonated CO-bound rHb1 WT and H73L do not exhibit this channel, suggesting restricted CO escape from the protein matrix and demonstrating that protonation of histidines within rHb1 modulate hydrophobic channels which form pathways of ligand escape.

3.3 Discussion

3.3.1 Origin of the temperature dependence of thermodynamic parameters

The observed temperature dependence of the enthalpy and volume changes associated with ligand photodissociation from WT rHb1 under stripped conditions is

somewhat intriguing. The volume change observed in the low temperature range (7 to 14 °C) is $3.3 \pm 0.7 \text{ mL mol}^{-1}$ larger than that observed in the high temperature range (14 to 35 °C) whereas the enthalpy change associated with CO photodissociation from rHb1 decreases above the transition temperature of 14 °C, with $\Delta H = 31.1 \pm 2.2 \text{ kcal mol}^{-1}$ below 14 °C and $6.2 \pm 3.3 \text{ kcal mol}^{-1}$ above 14 °C. A similar temperature dependence of the volume change was reported by Sakakura et al. (73) for CO photodissociation from myoglobin ($\Delta V = 16.8 \text{ mL mol}^{-1}$ at 0 °C and $\Delta V = 14.7 \text{ mL mol}^{-1}$ at 20 °C). Recently Fago et al. (74) have observed that O₂ association to neuroglobin is endothermic ($\Delta H = 12.7 \text{ kcal mol}^{-1}$) below 18 °C and exothermic ($-15.7 \text{ kcal mol}^{-1}$) above 18 °C. The difference in the enthalpy change observed by Fago et al. ($\Delta\Delta H = 28.4 \text{ kcal mol}^{-1}$) is very close to what we observe in rHb1 ($\Delta\Delta H = 24.9 \pm 3.3 \text{ kcal mol}^{-1}$). The authors associated the observed temperature dependence of enthalpy change to the temperature dependent oxygen-linked network of electrostatic interactions.

Examination of the crystal structure for 6c rHb1 (PDB 1D8U) (46) and 6c corn nsHb1 (PDB 2R50) reveals a network of electrostatic interactions formed by salt bridges between the heme propionate groups and residues on the E and F helices. The heme-7-propionate side chain, which is adjacent to the EF loop, forms hydrogen bonds with the F-helix residues Thr107 and Arg103 while the heme-6-propionate side chain, which is adjacent to the CD loop, forms hydrogen bonds with Lys69 and Tyr111 on the E and F helices respectively. In the structure of barley CN-nsHb1 (PDB 2OIF) (48) these interactions are not observed suggesting that the hydrogen bond network surrounding the propionate groups is significantly weaker or absent. The potential interaction of the 6-propionate side chain with nearby residues is particularly relevant due to its position adjacent to the distal heme cavity and the putative ligand migration pathway. (62) The presence of a ligation-dependent extended electrostatic network raises the question of

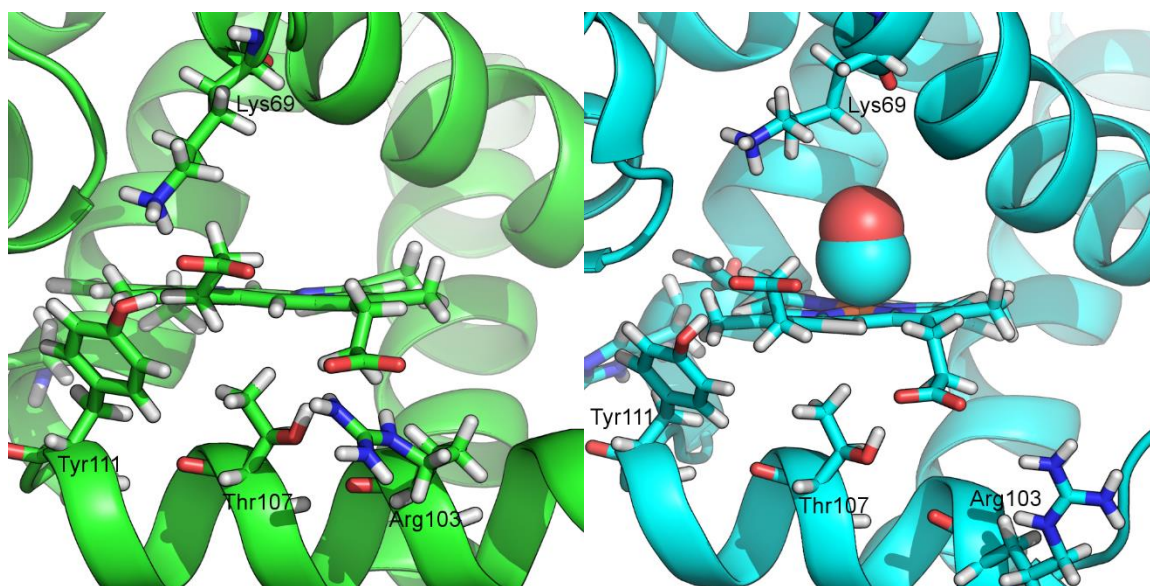


Figure 3.10 Representative positions of charged residues and heme propionate groups taken from cMD simulations of penta-coordinate WT (left) and CO-bound WT rHb1 (right) with His residue deprotonated. Proximal and distal histidines are not shown.

whether it is responsible for the temperature dependence of the observed thermodynamic parameters, as suggested by Fago et al. (74) (75)

The cMD simulation of deprotonated 5c rHb1 WT reveals a network of salt bridges between the heme propionate groups and local charged residues which is analogous to the electrostatic network observed in the crystal structure of 6c rHb1 but is absent in the cMD simulation of CO-rHb1 WT (Figure 3.10). In addition, $r_{\alpha-\alpha}$ decreases by approximately 2.0 Å in the 5c WT compared to the CO-bound WT (Table 3.4, Figure 3.11) suggesting a contraction of the EF helical region due to the transition between CO-bound 6c rHb1 WT and ligand free 5c rHb1 WT. This is similar to the difference seen in the 6c rHb1 WT and

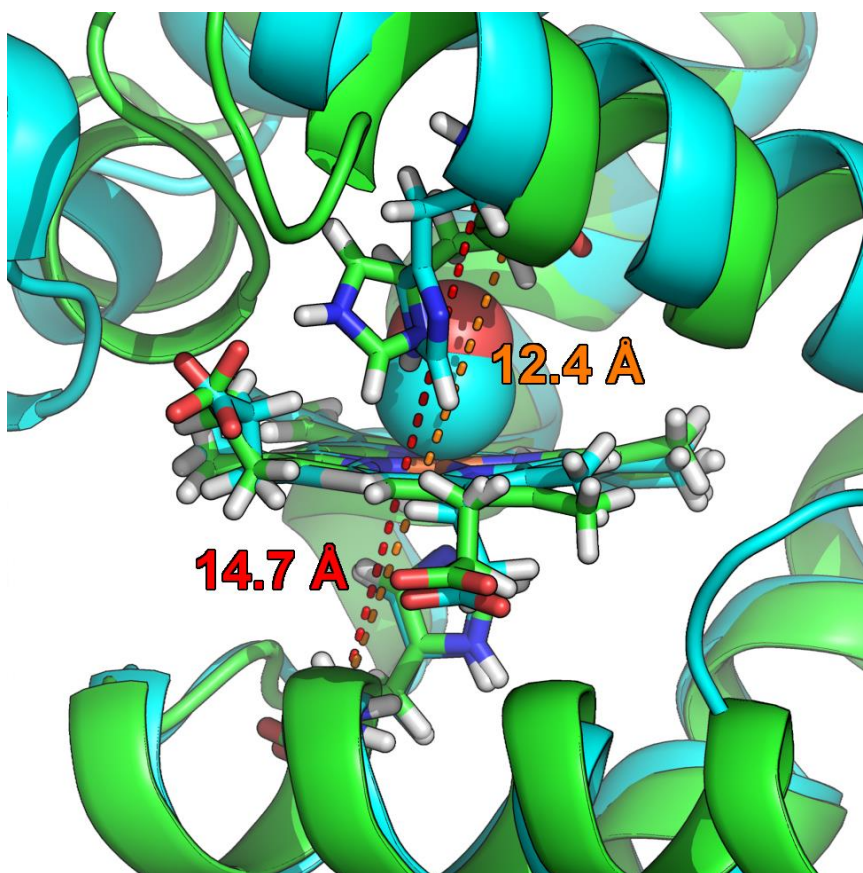


Figure 3.11 Overlay of EF region of deprotonated penta-coordinate rHb1 WT (green) and deprotonated CO-bound rHb1 WT (cyan) cMD simulations. Interhelical distance ($r_{\alpha-\alpha}$) of penta-coordinate WT is given by orange dotted line and text, while that of the CO-bound species is given by the red dotted line and text.

CN-barley nsHb1 crystal structures where $r_{\alpha-\alpha}$ is smaller by 2.5 Å in the former structure. The contraction of the EF region observed in the MD simulation may be correlated with the negative volume change we observe in PAC, where a value of $\Delta V_{\text{struc}} + \Delta V_{\text{el}} = -32.8 \pm 0.4 \text{ mL mol}^{-1}$ was determined for CO photolysis from rHb1 WT at pH 7.0 and below 14 °C. cMD simulations of the protonated CO-bound and 5c rHb1 WT indicate somewhat larger reorganization of the heme cavity upon ligand dissociation with a difference in the values of $r_{\alpha-\alpha}$ of 2.4 Å that is consistent with the more negative volume contraction observed in PAC at pH 6.0 ($\Delta V_{\text{struc}} + \Delta V_{\text{el}} = -36.0 \pm 0.3 \text{ mL mol}^{-1}$). Interestingly, a similar value was determined above 14 °C at pH 7.0 ($\Delta V_{\text{struc}} + \Delta V_{\text{el}} = -36.1 \pm 0.7 \text{ mL mol}^{-1}$) indicative of similar heme cavity reorganization at pH 6.0 and at high temperature and neutral pH.

Contraction of the EF helical region and reorientation of the charged residues around propionate groups also has an impact on enthalpy changes determined by PAC. In the low temperature range we observe $\Delta H_{\text{el}} = 15.1 \pm 2.2 \text{ kcal mol}^{-1}$, consistent with the endothermic enthalpy change due to the decreased solvation of charged residues forming salt bridges. (76) Above 14 °C a negative $\Delta H_{\text{el}} = -9.8 \pm 3.3 \text{ kcal mol}^{-1}$ was determined and is consistent with increased exposure and partial solvation of charged residues in the bulk solvent. (77) Given the above observations we propose that the aforementioned electrostatic network is absent in the CO bound form and its formation is triggered by the ligand photodissociation in the low temperature range (<14 °C) but the network is absent in 5c rHb1 WT at higher temperatures (>14 °C) at pH 7.0. Structural evidence from our cMD simulations suggests that the formation of salt bridges between the heme-6-propionate group and Tyr111/Lys69 as well as the heme-7-propionate group and

Arg103/Thr107 are responsible for the enthalpy change we see below 14 °C. We posit that the contraction of the EF helical region upon CO photorelease places these residues in close proximity to the heme propionate groups, facilitating the formation of salt bridges. The contribution of heme propionate groups to the thermodynamics of CO photodissociation from sperm whale CO-myoglobin (CO-swMb) has been previously proposed by Peters et al. (78) An enthalpic contribution of -7 kcal mol⁻¹ was attributed to breakage of a salt bridge between Arg45 and the heme-6-propionate group, a value similar to that observed in rHb1. However, later photoacoustic studies on CO-swMb by Sakakura et al. (79) contradict this finding. It is therefore ambiguous whether a direct analogy can be drawn between the ligand triggered electrostatic network reorganization in swMb and rHb1.

The observed thermodynamic parameters for CO photodissociation from the H73L mutant do not show a temperature dependence of ΔH or ΔV , suggesting distinct or weaker electrostatic interactions including the heme propionate groups in the absence of distal histidine. The structural differences between CO-rHb1 WT and H73L are immediately apparent given the difference in $r_{\alpha-\alpha}$ (14.4 and 12.8 Å, respectively), a smaller $\Delta r_{\alpha-\alpha}$ between CO-rHb1 H73L and 5c rHb1 H73L (0.2 Å) as compared to CO-rHb1 WT and 5c rHb1 WT (1.7 Å) as well as the absence of salt bridges in the former (Table 3.4). These data are supported by the observed volume change for the H73L mutant ($\Delta V_{\text{struc}} + \Delta V_{\text{el}} = -30.9 \pm 1.1$ mL mol⁻¹) that is smaller compared to WT ($\Delta V_{\text{struc}} = -32.7 \pm 0.4$ mL mol⁻¹). Using, $\Delta H_{\text{struc}} + \Delta H_{\text{el}} = -8.5 \pm 5.4$ kcal mol⁻¹ for CO photodissociation from the H73L mutant, $\Delta H_{\text{el}} = -17.3 \pm 5.4$ kcal mol⁻¹ is determined. This value is exothermic, similar to that determined for the WT above 14 °C ($\Delta H_{\text{el}} = -9.8 \pm 3.3$ kcal mol⁻¹) suggesting no change in

the electrostatic network upon ligand dissociation. This is supported by our cMD trajectory which shows that Lys69 and Arg103 are mostly in close proximity to the heme propionate groups in both the 5c and CO-bound forms of the H73L mutant (Figure 3.8).

Overall, from our computational and experimental data for rHb1 we associate the temperature dependence of the reaction volume and enthalpy changes with i) a conformational change of the EF helical region upon ligand photolysis which places the heme propionate groups into proximity with nearby charged residues and ii) a temperature dependent formation of salt bridges and an electrostatic network which includes the distal His in rHb1. This is supported by the fact that the observed temperature dependence of $\Delta V/\Delta H$ is eliminated in the presence of 0.50 M NaCl and in the H73L mutant. We have observed a similar temperature dependence of ΔV and ΔH in the case of O₂ photodissociation from human oxy-hemoglobin, but not in the case of CO photodissociation from human CO-hemoglobin (manuscript in preparation). This suggests a common mechanism between the two proteins and a possible link between the temperature dependence of structural changes and the presence of a strong hydrogen bond between the bound exogenous ligand and distal His residue, which can be found in both human oxy-hemoglobin and CO-rHb1 WT. (80) (48)

3.3.2 Effects of histidine protonation on ligand migration

Under mildly acidic conditions (20 mM HEPES buffer, pH 6.0) a decrease in the rate of ligand escape from the protein matrix was observed likely through the alteration of ligand migration pathway due to the protonation of one or more histidine residues. Histidine can be protonated at either nitrogen; typically, N_ε has a higher pK_a and remains

protonated at neutral pH, while N_δ is deprotonated. (81) In heme proteins with distal His residues coordinating the bound ligand, it is typically a protonated N_ε which donates a hydrogen bond to the proximal atom of the diatomic ligand while N_δ harbors a lone pair of electrons, leaving the overall residue neutral. The distal histidine in both CO-swMb (82) and ligated barley nsHb1 (48) follow this pattern. In general, the pK_a value of histidine residues in proteins covers a wide range with an average value of 6.6 ± 1.0 and is affected strongly by the residue environment. (83)

We have determined the pK_a of the distal His in oxidized rHb1 WT according to the method of Nienhaus et al to be 6.5 ± 0.05 (Figure 3.12) (84). Using this value, we estimate that the distal His is ~76% protonated in HEPES buffer at pH 6.0. Other than the distal His, rHb1 contains three other His residues: His108, His117, and His152. His108 is the proximal residue which coordinates the heme iron. In heme proteins this residue is solvent-restricted and highly acidic (pK_a ~ 4) (85) so we do not expect it to be protonated in rHb1 at pH 6.0. His117 and His152 are found at the C-terminal end of the B-helix and at position 10 on the H-helix, respectively. Analysis of our cMD simulations show these residues to be solvent-exposed which typically leads to a pK_a value between 6.0 and 8.0 in globular proteins (83) and in human hemoglobin. (86) This suggests that His117 and His152 undergo a change in protonation during transition from pH 7.0 to pH 6.0.

Studies of heme proteins with distal His residues, including swMb, human hemoglobin, and rHb1, have established that the distal His is able to adopt at least two conformations: one in which the distal His is located within the heme pocket and obstructs the pathway for ligand escape and one in which the distal His swings out of the heme pocket forming an open channel for diffusion of gaseous ligands and solvent molecules between the heme pocket and the bulk solvent. This model is commonly called the distal His gating mechanism. The equilibrium between the “closed” and “open” states is strongly affected by protonation of the distal His, as the positively-charged distal residue is able to form enthalpically favorable electrostatic interactions with water molecules in the bulk solvent, strongly favoring the open state. This mechanism has been observed in resonance Raman spectra of the heme site in barley CN-in which it was shown that at acidic pH the distal His is able to become protonated and adopt an open conformation (**61**) It has also

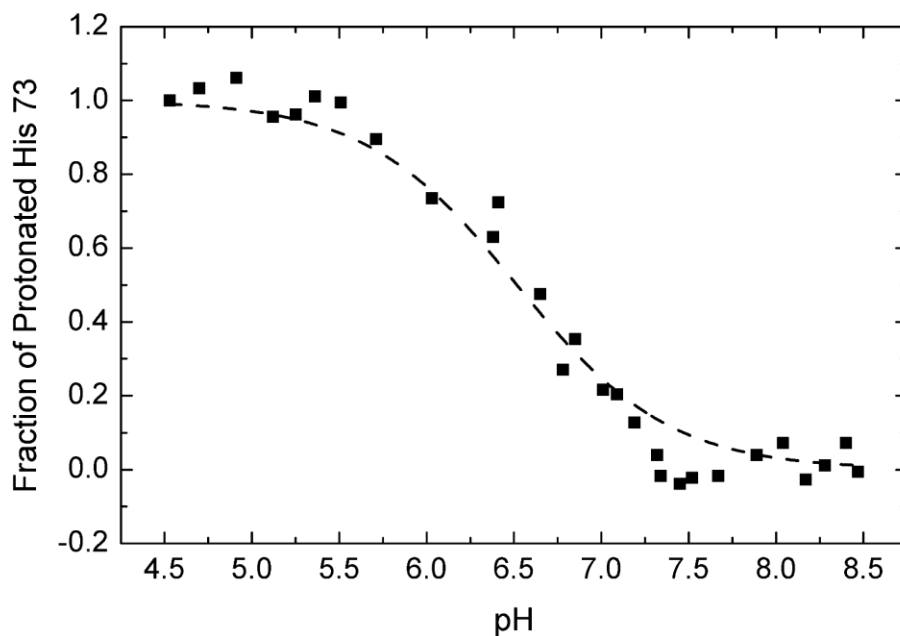


Figure 3.12 Fraction of protonated His 73 in oxidized rHb1 WT as determined by shift in Soret band wavelength according to the method of Nienhaus et al. (**84**)

been observed previously in *A. thaliana* CO-nsHb1, (27) in CO-swMb by IR spectroscopy (87) and in human hemoglobin. (80) The adoption of the open conformation is universally associated with faster ligand diffusion from the protein interior, which is inconsistent with our data. Thus, slower CO diffusion out of the protein under mildly acidic conditions in rHb1 is not due to protonation of the distal histidine and subsequent opening of the distal His gate. Protonation of His117 and His152 are most likely responsible for the observed effect on ligand migration kinetics and energetics.

The opening of the distal His gate has been determined to lead to an open channel for ligand diffusion between the distal heme cavity and the bulk solvent in *A. thaliana* nsHb1 at pH 5.5, (27) which contradicts our results for rHb1 WT. *A. thaliana* nsHb1 and rHb1 share a relatively high sequence identity (64%), however key residues in and near the active site differ between the two proteins. The distal heme cavity residue Phe40 (in rHb1) which is adjacent to the distal His and crucial for modulating interactions between the distal His and bound ligand, is conserved between rice and *A. thaliana* nsHbs. However, the preceding residue is a phenylalanine in rHb1 and a leucine in *A. thaliana* nsHb1. The presence of bulky Phe39 may stabilize the conformation of Phe40 in rHb1 and thus restrict ligand migration through the His gate in this protein. In addition, Ser49 in rHb1 has been identified to have protonation-dependent interactions with the nearby His117 (*vide infra*). The residue in *A. thaliana* nsHb1 which corresponds to Ser49 is Thr45, a bulkier residue which may not participate in the same electrostatic interactions.

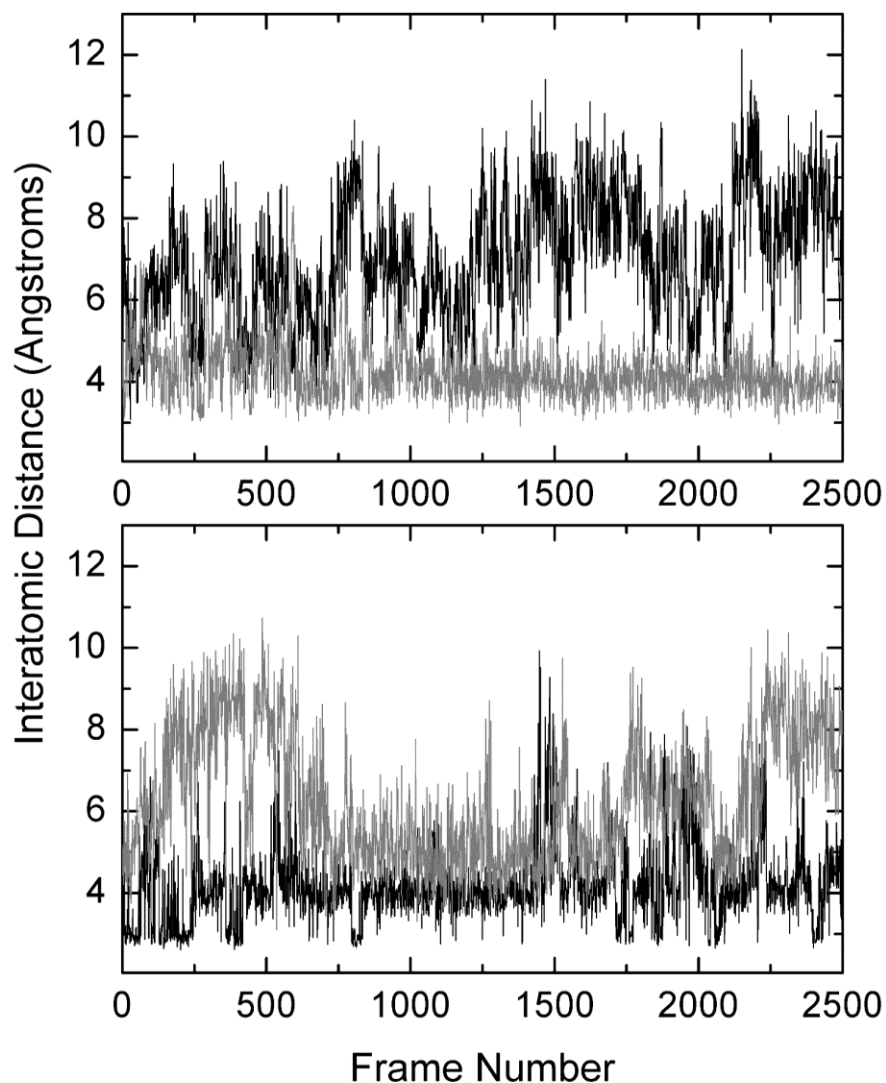


Figure 3.13 Distance between alcohol oxygen of Ser49 and N_{δ} of His117 during cMD trajectories of penta-coordinate rHb1 WT (top) and penta-coordinate rHb1 H73L (bottom) without (black line) and with (grey line) protonation of His73, His117, and His152.

PAC results reveal that CO escapes from WT rHb1 and H73L at pH 7.0 in less than ~50 ns. Such fast ligand escape from the protein matrix points towards the presence of the ligand migration pathway in the structure of WT rHb1 and H73L rHb1. The channels identified in the structure of CO-bound WT and H73L using MDpocket may represent a direct pathway for a fast ligand escape at neutral pH (Figure 3.9). Interestingly, these channels are not seen in the structure of protonated CO-bound WT or H73L, where the CO

escape is slower. Examination of the cMD simulations for 5c rHb1 WT and 5c rHb1 H73L with and without protonated histidines shows that the distance between the alcohol oxygen of Ser49 and N δ of His117 is strongly dependent on histidine protonation. In the simulated structure of deprotonated 5c rHb1 WT, the side chains of neutral His117 and Ser49 are distant; whereas these residues are in the hydrogen bond distance in protonated 5c rHb1 WT. (Figure 3.13, Top). The protonation of His 117 leads to rotation of the C-helix away from the heme iron, alteration of the CD loop, and reorientation of the side chains of distal

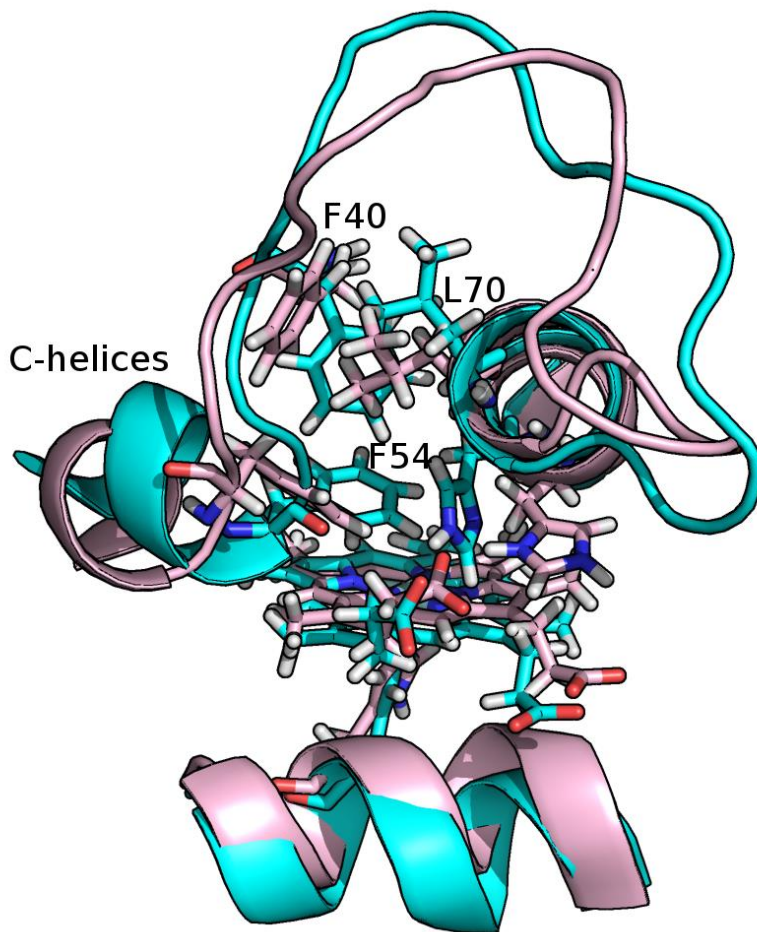


Figure 3.14 Overlay of EF region and CD loop of deprotonated 5c rHb1 WT (cyan) and protonated 5c rHb1 WT (cyan) cMD simulations. Residues 40 – 78 of the CD loop and E-helix and residues 102 – 112 of the F-helix are shown in cartoon representation.

Residues F40, F54, and L70, H73, and the heme group are shown as stick representations.

heme cavity residues (Phe40, Phe54, and Leu70) compared to the deprotonated 5c WT (Figure 3.14). Analysis of our MDpocket results shows that these structural changes result in opening of a channel in the vicinity of the CD loop in the protonated 5c rHb1 WT (Figure 3.15, Top Right). Water molecules can be seen freely diffusing between the distal heme cavity and the bulk solvent in the MD trajectory confirming the presence of an open channel. This channel is not observed in the cMD simulation of the protonated CO-bound rHb1 WT (Figure 3.15, Top Left).

The presence of an open channel for ligand diffusion in protonated rHb1 WT and its absence in the protonated CO-bound rHb1 WT suggests that upon ligand photolysis significant structural reorganization must occur prior to CO diffusion from the protein. This is consistent with the slower CO escape (134 ± 19 ns at 20 °C) and higher activation enthalpy ($\Delta H^\ddagger = 19.4 \pm 6.6$ kcal mol⁻¹) observed upon photolysis of CO from rHb1 WT at pH 6.0. ΔH^\ddagger observed for CO release from the WT at pH 6.0 is significantly higher than that previously determined for the WT at pH 7.0 ($\Delta H^\ddagger = 4.3 \pm 0.3$ kcal mol⁻¹) (62) confirming that analogous structural reorganization does not take place in rHb1 WT at pH 7.0. These data indicated that the reorganization of the heme binding pocket in the protonated form of the protein is relatively slow and represents a rate limiting step for CO escape from the protein matrix. The cMD simulations of the protonated 5c rHb1 H73L mutant show the opposite pattern with respect to interaction between Ser49 and His117 as the distance between Ser49 and His117 is larger when His117 is protonated, (Figure 3.13, Bottom). The overall structure of the CD loop is also significantly different (Figure 3.15, Bottom Right) with an almost complete loss of secondary structure in the CD loop with

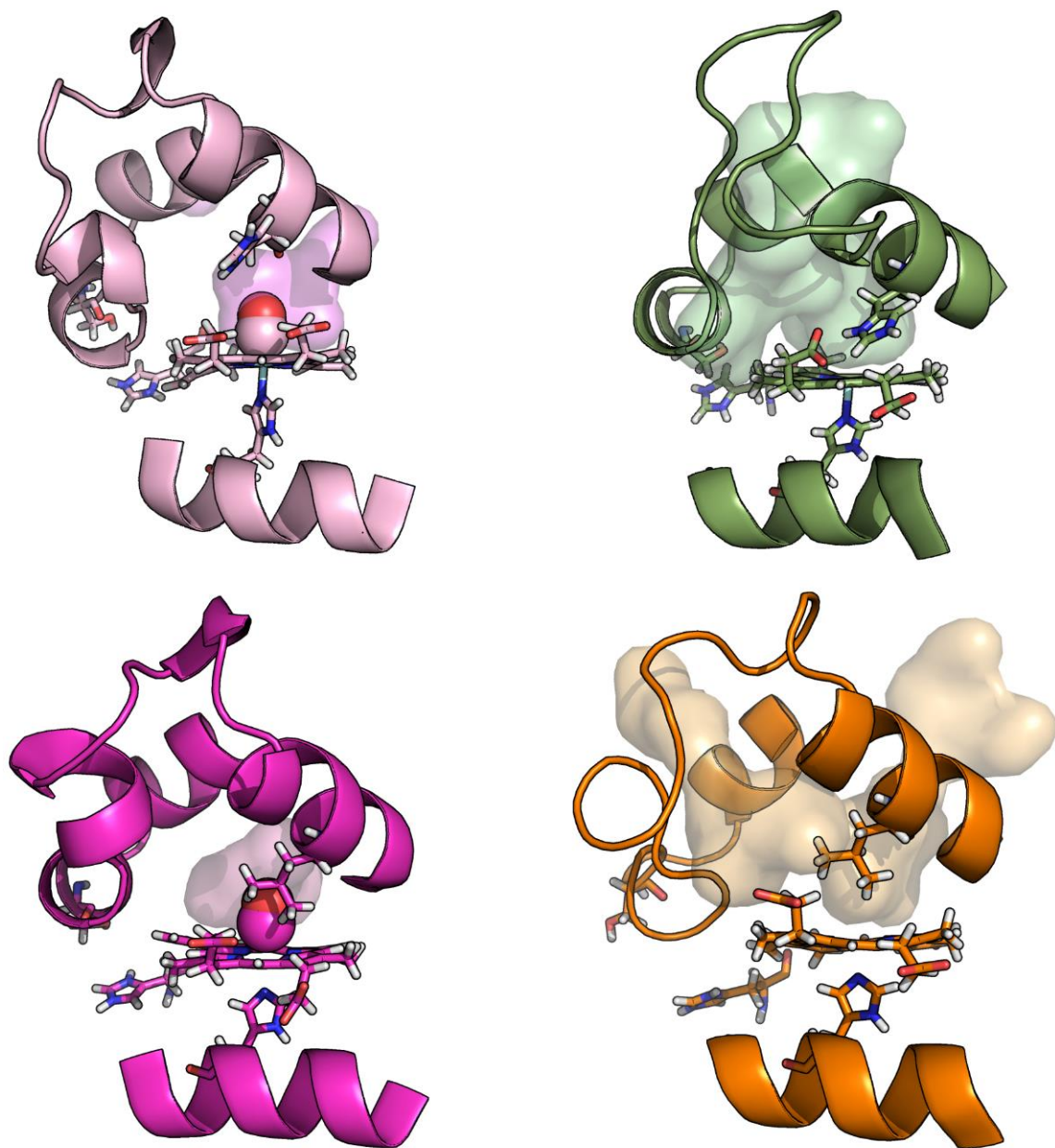


Figure 3.15 CD loop and EF regions of rHb1 with representative cavities determined by MDpocket analysis shown. Carbon monoxide, His73, His108, His117, Ser49 and heme group shown. In all images residues 40 – 78 of the CD loop and E-helix and residues 102 – 112 of the F-helix are shown in cartoon representation.

(Top Left, Pink) CO-bound WT protein with protonated histidines.

(Top Right, Green) Penta-coordinate WT protein with protonated histidines.

(Bottom Left, Magenta) CO-bound H73L protein with protonated histidines.

(Bottom Right, Orange) Penta-coordinate H73L protein with protonated histidines.

respect to the CD loop conformation at pH 7.0. MDpocket analysis of deprotonated CO-rHb1 H73L shows a direct channel that extends from the distal heme pocket to the exterior of the protein which may facilitate the fast ligand escape (<50 ns) we see for the mutant at pH 7.0 using PAC (Figure 3.9, Right). Analogous channel is missing in the structure of protonated CO bound 5c rHb1 H73L. However, in the structure of protonated 5c rHb1 H73L, the CD loop adopts a conformation where the sidechains of residues Phe40, Phe44, Phe54, Leu70, and adjacent residues shift open a new hydrophobic channel in the vicinity of the CD loop, similar to the protonated 5c rHb1 WT. This results in a complete loss of α -helical structure in the CD loop. Concurrently, residues within the protein interior including Trp25, Ile35, Phe39, Met75, and Phe78 reorient to open a channel which extends towards the AB-loop providing a second route for ligand escape to the bulk solvent. This channel is not observed in the cMD simulation of the protonated CO-bound rHb1 H73L (Figure 3.15, Bottom Left), again showing that a tertiary structural reorganization in the vicinity of the CD loop must occur to facilitate ligand escape. This also provides an explanation for slower CO escape from rHb1 H73L at pH 6.0 as determined by PAC ($\tau = 90 \pm 15$ ns at 16 °C). The lower activation enthalpy determined for CO escape from the H73L mutant at pH 6.0 is 0.2 ± 1.1 kcal mol⁻¹ compared to WT rHb1 this points towards a distinct conformational transition in rHb1 WT and rHb1 H73L that leads to the opening of ligand migration pathways. The activation enthalpy value determined here is small lower than the value measured by Bisht et al. at for ligand escape at neutral pH (6.0 ± 0.2 kcal mol⁻¹) but similar to that for rHb1 H74A at neutral pH (0.14 ± 0.03 kcal mol⁻¹).

Overall, we demonstrate that the distal residue and protonation states of histidines in rHb1 have significant impact on rates, energetic barriers, and pathways for ligand migration in rHb1. Protonation of peripheral histidines leads to reorganization of the CD loop and alteration of the EF helical region that modulate the ligand migration pathway and impact the rates for external ligand escape.

A sudden reduction of light exposure causes the cytosolic pH in plant cells to decrease by up to 0.3 units while over longer periods hypoxia can cause the cytosolic pH to decrease by 0.5 – 0.6 units (88). Given a typical cytosolic pH of ~7.2, changes in the protonation of His73, His117, and His152 can occur in a significant number of rHb1 molecules *in vivo* suggesting that the rHb1 conformational dynamic and protein-ligand interactions could be affected by the changes in cytosolic pH. The results of cMD indicate His117 and Ser49 are well-conserved among non-symbiotic hemoglobins (Figure 3.16). Taking into account that expression of rHb1 is upregulated under conditions of etiolation and hypoxia (89) further suggests that it has a role in the cellular response to these conditions. Type 1 nsHbs in general are typically thought to carry out an NO dioxygenase function which protects the cell under etiolated/hypoxic conditions. (90) As we have shown, protonation of rHb1 greatly alters the pathway for ligand migration between the distal heme cavity and the bulk solvent and would clearly affect the NO dioxygenase mechanism, which requires binding of an oxygen molecule to the heme iron followed by

```

Rice_nsHb1/1-166      1 MALVEDNNA - - - VAVSFSEEQEALV LKSWA I LK KDSANI ALRFF LK I FEVAFSASQMF 55
Rice_nsHb2/1-169     1 MALVEGNNVSGGAVSFSEEQEALV LKSWA I M K KDSANI GLRFF LK I FEVAFSASQMF 58
Maize_nsHb/1-165     1 MALAE - - - ADDGAVVFSEEQEALV LKSWAVM KDAANLGLRFF LK VFE I AFSAEQMF 54
Barley_nsHb/1-162    1 - - - MS - - - AEGAVVFSEEKEALV LKSWA I M K KDSANLGLRFF LK I FE I AFSARQMF 51
Rice_nsHb3/1-169     1 - MAANGSNVSRGAVRFTEEQEALV LKSWA I M K NDSAHI GHRFF LK I FEVAFSARQLF 57
Rice_nsHb4/1-167     1 - - - MAFASASNGAVRFTEEQEALV LKSWA I M K DDSANI GHRFF LK I FEVAFSARHLF 54
Cotton_nsHb1/1-163   1 - - - - - - - MATYEGKVFTEEQEALV V KSWTVM K KTAELGLKFF LK I FE I AFSAKKLF 50
Alfalfa_nsHb1/1-160  1 - - - - - - - MGLDTKGFTEEQEALV V KSWNAM K KNSAELGLKFF LK I FE I AFSAQKLF 50
A.thaliana_nsHb1/1-160 1 - - - - - - - MESEGI V FTEEQEALV V KSWVM K KNSAELGLKFF I K I FE I APTTKKMF 50
T.tomentosa_nsHb/1-161 1 - - - - - - - MSSSEVDKVFTEEQEALV V KSWAVM K KNSAELGLKFF LK I FE I AFSAKNLF 51
Cotton_nsHb2/1-159   1 - - - - - - - MGFTEKQEGLV KESWEVLK QD I PHSSLRFFSL I LE I AFGAKNMF 44

Rice_nsHb1/1-166     56 SFLRNSDVP LEKNPK LKTHAMS V F VMTCE AAAQLRKAGKVT VRD T T LKRLGATH LKYG 113
Rice_nsHb2/1-169     59 SFLRNSDVP LEKNPK LKTHAMS V F VMTCE AAAQLRKAGKVT VRD T T LKRLGATHFKY G 116
Maize_nsHb/1-165     55 SFLRSDVP LEKNPK LKTHAMS V F VMTCE AAAQLRKAGKVT VRE T T LKRLGATHLRYG 112
Barley_nsHb/1-162    52 PFLRSDVP LETNPK LKTHAVS V F VMTCE AAAQLRKAGK I T VRE T T LKRLGGTHLYG 109
Rice_nsHb3/1-169     58 SFLRNSDVP LEKNPK LK I HAMA V F VMTCE AAAQLRK TGRVT VRD T T I KRLGSTHFKN G 115
Rice_nsHb4/1-167     55 SFLRNSDVP LEKNPN LK KHAMAV F VMTCE AAAQLRK TGRVT VRD T T I KRLGSTHFKN G 112
Cotton_nsHb1/1-163   51 SFLRDSNVP LEQNTK LKPHAMS V F VMTCE SAVQLRKAGKVT VRESNL K KLGATHFKY G 108
Alfalfa_nsHb1/1-160  51 SFLKDSKVP LEQNTK LKPHAMS V F LMTCE SAVQLRKSGKVT VRESSL K KLGANHFKY G 108
A.thaliana_nsHb1/1-160 51 SFLRDSPI PAEQNP K LKPHAMS V F VMCES SAVQLRK TGVVT VRE T T LKRLGASHSKY G 108
T.tomentosa_nsHb/1-161 52 SYLKDSP I PLEQNP K LKPHAM T V F VMTCE SAVQLRKAGKVT VRESNL KRLGA I HFKNG 109
Cotton_nsHb2/1-159   45 SFLRESEE I PQNPK LKAH AVK V F VMTCE SA I QLREKGEVVAD T T LKY LGTVHVKSG 102

Rice_nsHb1/1-166     114 VGDAHFEVVKF ALLDT I KE E V PADM W S PAMKS AWSEAYDHLVAA I KQEMKPAE - - - - 166
Rice_nsHb2/1-169     117 VGDAHFEVTRF ALLET I KEAVP VDM W S PAMKS AWSEAYNQLVAA I KQEMKPAE - - - - 169
Maize_nsHb/1-165     113 VADGHFEVTGF ALLET I KEALPADM W SLE M K KAWAEAYSQLVAA I KREMKPDA - - - - 165
Barley_nsHb/1-162    110 VADGHFEVTRF ALLET I KEALPADM W GPE M R NAWGEAYDQLVAA I KQEMKPAE - - - - 162
Rice_nsHb3/1-169     116 VSDAHFEVAKF ALLET I KEAVP ASM W S PAMK GAWGEAYDHLVAA I KQGMKPAE - - - - 169
Rice_nsHb4/1-167     113 VSDTHFEVARF ALLET I KDGI PASM W S P E MKNAWGEAYEHLVAA I KEGMKPVALL - - 167
Cotton_nsHb1/1-163   109 VVDEHFEVTKF ALLET I KEAVP - DM W SDE MKNAWGEAYDRLVAA I K IEMKACSQAA - 163
Alfalfa_nsHb1/1-160  109 VVDEHFEVTKF ALLET I KEAVP - EM W S PAMKNAWGEAYDQLVNA I KSEMKPSS - - - - 160
A.thaliana_nsHb1/1-160 109 VVDEHFEVAKY ALLET I KEAVP - EM W S P E M K VAWGQAYDHLVAA I KAEMNLSN - - - - 160
T.tomentosa_nsHb/1-161 110 VVNEHFE - TRF ALLET I KEAVP - EM W S P E M K NAWGEAYDQLVAA I KSEMKPSST - - - 161
Cotton_nsHb2/1-159   103 VKDPHFEVVKF ALLRT I EEA I GEEK V NEE MKNAWGEAYDQLAE A I KAEMKNHHD E T A 159

```

Figure 3.16 Sequence alignment of the top 10 nsHbs in the UniProt database with highest sequence homology to rHb1. The Ser at the C-terminal end of the B-helix (Ser49 in rHb1) and His in the CD loop (His117 in rHb1) are highlighted with red boxes.

diffusion of an NO molecule into the active site. (90) Therefore, the protonation state of His residues in rHb1 could serve as a mechanism by which the protein reacts directly to intracellular pH and indirectly to etiolation/hypoxia. However, the effect of pH on NO dioxygenase activity of rHb1 has not been explored.

3.4 Conclusion

Heretofore we have demonstrated that changes in temperature, ionic strength, identity of the distal residue, and pH of the protein environment can have significant impacts on kinetics, energetics, and ligand migration pathways associated with CO photodissociation from rHb1. An important question is whether these conditions are relevant to those experienced by the protein *in vivo* or merely convenient for observing an interesting but largely irrelevant phenomenon *in vitro*.

The mechanism we have identified that causes the temperature dependence of thermodynamic parameters we observe using PAC may be applicable to other heme proteins. The impact of interactions between the heme propionate groups and adjacent amino acid residues has been explored previously in horse heart myoglobin reconstituted with heme group derivatives which replace the propionate groups with either a methyl ester or ethyl group. (91) It was determined that disruption of a salt bridge network between the heme propionate groups and nearby amino acid residues results in a more open conformation and less restricted ligand access to the distal heme pocket. This suggests that these interactions may have a functional role in modulating the ligand migration pathway between the distal heme pocket and the bulk solvent; however, it is still unclear whether these interactions would occur to a significant degree *in vivo*, given the presence of various ions, exogenous effectors, and cellular crowding conditions.

4 THERMODYNAMIC PARAMETERS FOR O₂ PHOTORELEASE FROM HEMOGLOBIN:EFFECTOR COMPLEXES

4.1 Introduction

Human adult hemoglobin (Hb) is a tetrameric globin which serves as a carrier of oxygen and carbon dioxide in the erythrocytes of a wide variety of vertebrates. As result of exhibiting cooperative oxygen association, Hb has served as a model system for determining the mechanism for cooperative ligand/substrate association to proteins and the mechanisms of action and biological roles of allosteric effectors.

The first theory to explain the mechanism of regulation of ligand affinity in Hb was presented by Perutz using the X-ray structure of oxygen-bound human hemoglobin (oxyHb). (92) The idea, following the theory of Monod, Wyman, and Changeux, (20) attributed the allosteric and cooperative ligand association to Hb to a quaternary structural transition between the high affinity relaxed (R) and low affinity tense (T) states of the protein and subsequent rotation of the $\alpha\beta$ dimers with respect to one another. Endogenous effectors such as 2,3-bisphosphoglycerate were theorized to lower Hb oxygen affinity by shifting the equilibrium between the R and T states towards the low affinity state.

The discovery that drugs such as bezafibrate (BZF) could also lower the oxygen affinity of hemoglobin (21) without causing a shift between the R and T states encouraged further studies of Hb:effector systems and synthesis of structurally analogous compounds with stronger effects including the 2-[4-[[[(Arylamino)carbonyl]amino]phenoxy]-2-methylpropionic acids. (22) Compounds such as BZF and 2-[4-(3,5-dichlorophenylureido)phenoxy]-2-methylpropionic acid (L35) (93) bind to a low affinity

site on the protein surface and a high affinity site within the central cavity of both the R- and T-states of Hb, lowering ligand affinity regardless of quaternary structure. (94), (95) The canonical MWC/Perutz model is not able to account for the observed behavior of Hb in the presence of these synthetic allosteric effectors. It was reported that L35 has similar effects on semihemoglobins – $\alpha\beta$ dimers with one apo subunit and one heme-containing subunit – indicating that the tetrameric organization of the protein is unnecessary for its allosteric regulation. (24) In light of these experimental data, new models such as the tertiary two-state model proposed by Henry et al (25) and the global allostery model proposed by Yonetani et al. (23) have been developed to explain the impact of both endogenous and synthetic heterotropic effectors on the functional properties of hemoglobin. Both models focus on the contributions of the tertiary structure to cooperativity and allosteric regulation of protein interactions with diatomic ligands. However, the exact mechanism by which synthetic effectors such as L35 lower the oxygen affinity of Hb has not been confirmed.

In addition to these new models of cooperativity and allostery, numerous experimental and theoretical studies have demonstrated a disparity between the interactions of CO and O₂ with Hb. The processes of geminate and bimolecular rebinding of O₂ to Hb occur faster than rebinding of CO. In addition, upon photodissociation the ligand migration mechanism seems to be different for O₂ and CO. Birukou et al. have proposed that photodissociated CO does not sample internal hydrophobic cavities, since the decrease of the volume of internal cavities either by presence of Xe gas or through site directed mutagenesis does not alter geminate rebinding rate constants for CO. (96) However, combined molecular dynamics and laser spectroscopy experiments on O₂

photodissociation from the isolated α chains of Hb have shown that O_2 may transiently occupy hydrophobic Xe cavities before rebinding to the heme iron or exiting through the distal His gate. (97) Differences in the tertiary structural dynamics of the protein near the heme pocket upon ligand photodissociation have also been identified. Murakawa et al. (98) used time-resolved resonance Raman spectroscopy to characterize structural changes within the EF helical region associated with O_2 and CO photodissociation. The data show that the structural dynamics of the EF helical region are one order of magnitude faster upon Fe- O_2 bond dissociation. This difference was attributed to the presence of the hydrogen bond between the distal His and O_2 . (16)

Altogether, the discrepancies between O_2 and CO with respect to the exact ligand migration pathway and tertiary structural dynamics upon ligand photodissociation indicate the need for focused study of the unique characteristics of oxyHb. In this study we use transient absorption (TA) and photoacoustic calorimetry (PAC) techniques to characterize kinetic and thermodynamic parameters associated with O_2 photodissociation from human adult hemoglobin in the presence and absence of the allosteric effectors L35 and inositol hexakisphosphate (IHP). Transient absorption techniques are well established in the study of ligand binding to heme proteins, and have been used previously in the characterization of the kinetics of CO (96) and O_2 (99) rebinding to hemoglobin after photodissociation. Photoacoustic calorimetry has previously been used in the characterization of the thermodynamics of ligand photodissociation from heme proteins, including horseradish and soybean peroxidases (100) and *Amphitrite ornata* dehaloperoxidase. (101) Photoacoustic calorimetry has also been used to characterize ligand-dependent differences in the kinetics of ligand photodissociation from oxy- and carbonmonoxymyoglobin; a

kinetic step of ~250 ns was attributed to O₂ escape from the protein matrix, approximately three times faster than CO escape. (102) The thermodynamics of CO photodissociation from carbonmonoxyhemoglobin (CO-Hb) in the presence of the effectors BZF and IHP were also probed. (102) While the binding of BZF to the protein did not significantly affect the observed volume and enthalpy changes (ΔV and ΔH), the binding of the effector IHP was found to have an impact. There was a 10 mL mol⁻¹ decrease of ΔV and a 30 kcal mol⁻¹ decrease of ΔH , which were attributed to electrostriction of charges on the protein surface within ~50 ns of CO photodissociation. Hence, the use of PAC to study ligand photodissociation in heme proteins allows for characterization of the photolysis of the iron-ligand bond, the process of ligand escape from the protein matrix, and structural reorganization associated with ligand photorelease on fast time scales (50 ns to 10 μ s). Together, the use of TA and PAC allows us to gain insight into the mechanism of allosteric regulation of Hb activity and the discrepancy between the thermodynamic and kinetic properties of the O₂- and CO-bound protein upon photodissociation.

4.2 Results

4.2.1 UV-vis spectra

The absorption spectra of stripped met-, deoxy- and O₂-bound Hb in 20 mM HEPES buffer, pH 7.0 are shown in Figure 4.1 Upon O₂ binding to Hb, the Soret band absorption maximum shifts to 414 nm and the alpha and beta band are found at 541 and 577 nm. The addition of 1.60 mM IHP does not cause a change in the Hb absorption spectra (data not shown), while addition of 0.50 mM L35 does not alter the absorption spectrum of met- and

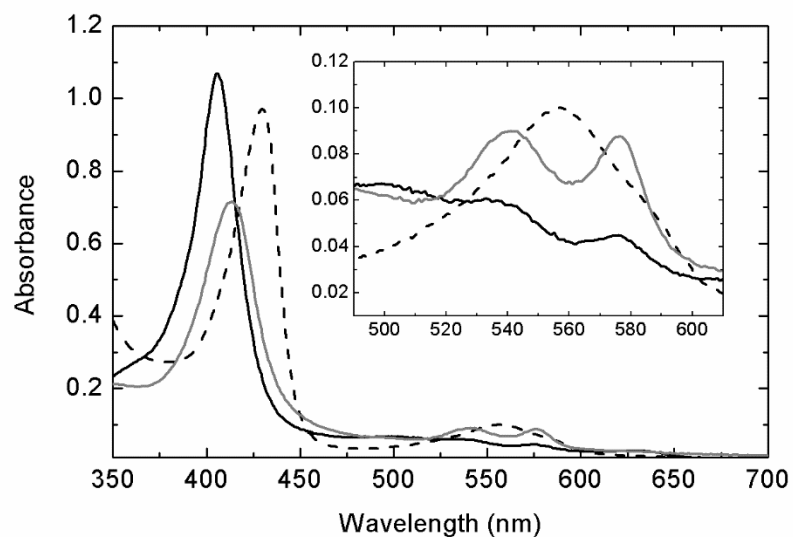


Figure 4.1 Steady-state UV-vis absorption spectra of metHb (solid black line), deoxyHb (dashed line), and oxyHb (solid gray line) in 20 mM HEPES buffer with no effector present, pH 7.0. Inset: Absorbance spectra from 500 – 600 nm showing Q bands.

deoxyHb but leads to a bathochromic shift of the Soret band from 415 to 410 nm in oxyHb (data not shown). This shift may be the result of binding of L35 to a low-affinity site near the heme pocket (95) directly affecting the electronic structure of the heme group, effects on the heme environment which are propagated from the central cavity binding site, or a combination of these factors.

4.2.2 Photoacoustic calorimetry results

The photoacoustic traces for O₂ photorelease from stripped oxyHb in 20 mM HEPES buffer, pH 7.0 are shown in Figure 4.2. The absence of a phase shift between the sample and reference acoustic traces indicates an absence of volume and enthalpy changes occurring approximately 50 ns to 10 μs after ligand photorelease in agreement with the fast ligand escape from the protein matrix reported previously. (97)

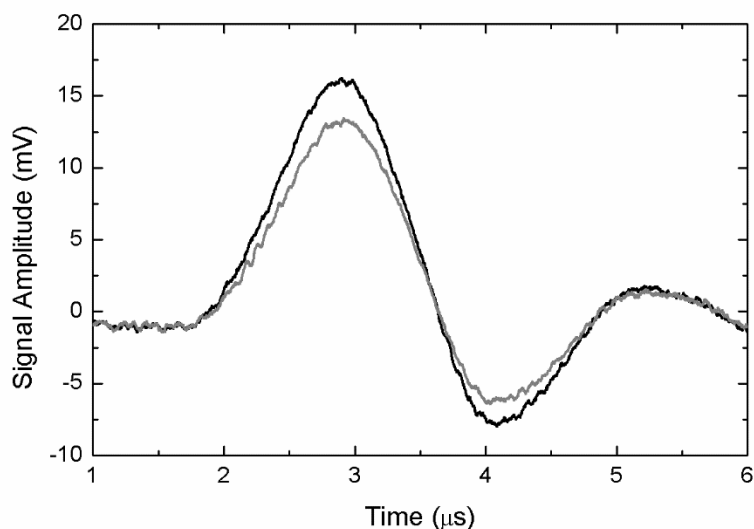


Figure 4.2 PAC traces for O₂ photorelease from stripped oxyHb (black line) and the reference compound Fe(III)4SP (gray line) at 20°C in 20 mM HEPES buffer, pH 7.0.

Figure 4.3 shows the plots of $E_{hv}(\varphi-1)/\Phi_{bm}$ as a function of $C_p\rho/\beta$. The plot of $E_{hv}(S/R-1)/\Phi_{bm}$ as a function of $C_p\rho/\beta$ is linear in the temperature range from 7 to 35 °C for CO photorelease from (CO)₄Hb and for O₂ photorelease from (O₂)₄Hb in the presence of 500 mM NaCl or 100 mM phosphate buffer. Interestingly, the plot of the ratio of the sample and reference amplitude for O₂ photodissociation from Hb under stripped conditions or in the presence of L35 or 20 mM phosphate buffer shows a V-shaped dependence, indicating that the observed volume and enthalpy changes (ΔV and ΔH) are temperature dependent. This transition occurs at 16 °C for stripped oxyHb and at 12 °C for the oxyHb:L35 complex and for oxyHb in 20 mM phosphate buffer. The recovered thermodynamic parameters are presented in Table 4.1.

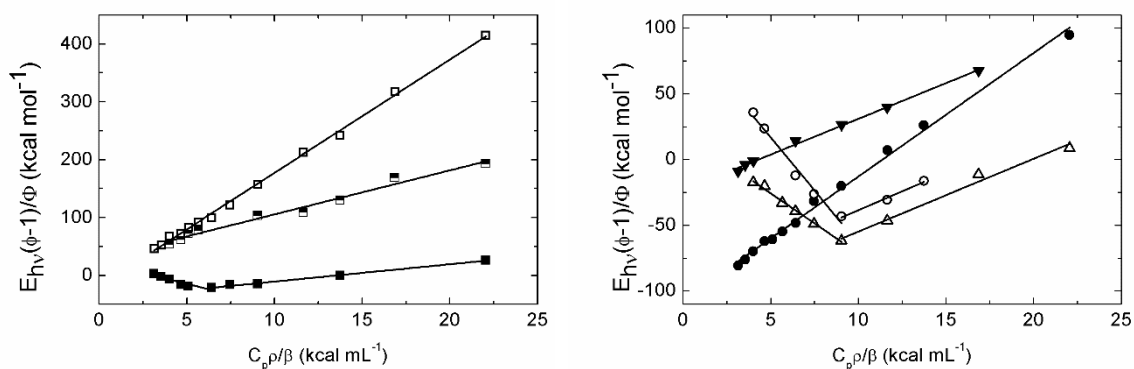


Figure 4.3 (Left) Plot of ratio of sample and reference acoustic trace amplitudes as a function of the temperature dependent factor ($C_p\rho/\beta$) for CO photorelease from stripped CO-Hb (filled squares), O₂ photorelease from stripped oxyHb (open squares) and oxyHb in the presence of 500 mM NaCl (half-filled squares).

Since a low laser power (<50 μJ) was used in PAC measurements, the observed volume changes for oxyHb samples correspond to a transition between the fully ligated Hb(O₂)₄ and the triply ligated Hb(O₂)₃, and can be expressed as:

$$\Delta V = [V_{\text{Hb}(\text{O}_2)_3}^\circ - V_{\text{Hb}(\text{O}_2)_4}^\circ] + V_{\text{O}_2}^\circ + \Delta V_{\text{el}} + \Delta V_{\text{DPH}} \quad (4.1)$$

where the first term of Equation 4.1 represents the difference in structural volume between the triply and quadruply ligated Hb species (ΔV_{struc}). The parameter $V_{\text{O}_2}^\circ$ is the average molar volume of O₂ in water ($32.1 \pm 0.1 \text{ mL mol}^{-1}$), (103) and ΔV_{el} is the change in volume that results from electrostriction of solvent molecules near exposed charges. Its value can be estimated as the difference between ΔV measured for O₂ photodissociation from stripped Hb in low ionic strength buffer (20 mM HEPES, pH 7.0) and from stripped Hb in a high ionic strength buffer (20 mM HEPES with 500 mM NaCl, pH 7.0) since high ionic strength eliminates the effect of electrostriction. We estimate ΔV_{el} to be $-10.8 \text{ mL mol}^{-1}$ for O₂ photodissociation from oxyHb in the low temperature range (7 – 16 °C) and larger, $-33.4 \text{ mL mol}^{-1}$ in the high temperature range (16 – 35 °C). There is also a small contribution

Table 4.1 Volume and enthalpy changes (ΔV and ΔH) associated with CO/O₂ photodissociation from stripped Hb and Hb:effector complexes.

Conditions	Temp. (°C)	ΔV (mL mol ⁻¹)	$\Delta V_{\text{struc}} + \Delta V_{\text{el}}$ (mL mol ⁻¹)	ΔH (kcal mol ⁻¹)	$\Delta H_{\text{struc}} + \Delta H_{\text{el}}$ (kcal mol ⁻¹)
Stripped CO-Hb	7 - 35	21.5 ± 0.9	-5.7 ± 0.9	19.4 ± 1.2	1.9 ± 1.2
Stripped oxyHb	7 - 16	3.8 ± 0.2	-20.5 ± 0.2	62.5 ± 19.4	44.5 ± 19.4
	16 - 35	-18.8 ± 1.8	-43.1 ± 1.8	-67.1 ± 12.3	-85.1 ± 12.3
500 mM NaCl	7 - 35	14.6 ± 2.4	-9.7 ± 2.4	78.1 ± 15.4	57.1 ± 15.4
pH 6	7 - 35	7.0 ± 1.0	-17.3 ± 1.0	56.3 ± 2.0	35.3 ± 2.0
1.60 mM IHP	7 - 35	12.7 ± 1.5	-11.6 ± 1.5	128.3 ± 24.2	110.3 ± 24.2
0.50 mM L35	7 - 12	4.2 ± 1.3	-20.0 ± 1.3	104.9 ± 5.2	86.9 ± 5.2
	12 - 35	-14.7 ± 5.6	-39.0 ± 5.6	-18.2 ± 1.7	-36.2 ± 1.7
20 mM phosphate	7 - 12	4.8 ± 1.4	-19.5 ± 1.4	38.6 ± 18.4	20.6 ± 18.4
	12 - 35	-7.5 ± 0.8	-31.8 ± 0.8	28.7 ± 6.2	10.7 ± 6.2
100 mM phosphate	7 - 35	5.2 ± 0.4	-19.1 ± 0.4	19.3 ± 3.0	1.3 ± 3.0

that results from hydration of the distal heme pocket after ligand escape from the protein matrix.

The rate constant for water entry into the distal heme pocket of CO-Hb has been reported to be 6 μs^{-1} by Esquerra et al., (104) corresponding to a time constant of ~ 167 ns. Normally, a shift in phase between the sample and reference PAC signals would be observed for any processes in this timeframe. Since we do not observe this shift, we conclude that the process of water entry into the heme pocket of (O₂)₃Hb after photodissociation must be faster than in CO-Hb, occurring in <50 ns. On the basis of the average of the fractional occupation for the α and β chains as determined by Esquerra et al. (104) (~0.44) and the partial molar volume of H₂O (18.0 mL mol⁻¹), we calculate a value of 7.8 mL mol⁻¹ for ΔV_{DPH} .

$$\Delta H = \Delta H_{\text{Fe-O}_2}^{\circ} + \Delta H_{\text{solv}} + \Delta H_{\text{struc}} + \Delta H_{\text{el}} \quad (4.2)$$

Equation 4.2 describes the individual contributions to the observed reaction enthalpy change, ΔH . The parameter $\Delta H_{\text{Fe-O}_2}^{\circ}$ is the enthalpy of dissociation of the iron-oxygen bond and ΔH_{solv} is the enthalpy of solvation of O_2 (-2.9 kcal mol). **(105)** Together these contributions are equal to 21 ± 0.07 kcal mol⁻¹. **(106)** There is also a contribution from hydration of the heme pocket (-3 kcal mol⁻¹). **(107)** Since the hydration contribution is small we include this term into the structural enthalpy, ΔH_{struc} . ΔH_{el} is the enthalpy change associated with electrostriction, which we can determine using a method analogous to that for ΔV_{el} , estimating -12.6 kcal mol⁻¹ for the low temperature range (7 – 16 °C) and -142.2 for the high temperature range (16 – 35 °C). ΔH_{struc} is the change in enthalpy associated with structural changes due to the transition from the fully ligated $(\text{O}_2)_4\text{Hb}$ to the triply ligated $(\text{O}_2)_3\text{Hb}$.

For O_2 photorelease from oxyHb under stripped conditions, we observe a temperature dependence of the thermodynamic parameters with a sharp transition at 16°C (Figure 4.3, Left). When we account for the contributions of O_2 molecular volume, electrostriction, distal pocket hydration, enthalpy of the Fe- O_2 bond, and enthalpy of solvation to ΔH and ΔV as outlined in Equations 4.1 and 4.2, we determine ΔV_{struc} to be -9.7 ± 0.2 mL mol⁻¹ and ΔH_{struc} to be 57.1 ± 19.4 kcal mol⁻¹ below 16°C. At higher temperatures ΔH becomes exothermic (-67.1 ± 12.3 kcal mol⁻¹) with a larger value for the enthalpy of electrostriction, ΔH_{el} (-142.2 ± 12.3 kcal mol⁻¹) and a larger volume contraction of (-43.1 ± 1.8 mL mol⁻¹) is observed. In the presence of charged effectors (Cl^- (Figure 4.3,

Left), IHP (Figure 4.3, Right) or in the presence of 100 mM phosphate buffer (Figure 4.3, Right) ΔV and ΔH for O₂ photodissociation are temperature independent.

The thermodynamic parameters determined for photodissociation of O₂ from stripped oxyHb below 16°C are different from those for CO. For ligand photodissociation from the CO-Hb complex, ΔV and ΔH were determined to be 21.5 ± 0.9 mL mol⁻¹ and 19.4 ± 1.2 kcal mol⁻¹, respectively. These values are identical to those previously determined by Peters et al. using PAC, (37) and the volume change is comparable to the value observed upon photodissociation of CO from CO-Mb using X-ray scattering (13 mL mol⁻¹). (108) The value of ΔV is 17.4 mL mol⁻¹ larger for photodissociation of CO from CO-Hb as compared to photodissociation of O₂ from oxyHb, which cannot be accounted for by the difference in partial molar volume between the dissociated ligands, which is only 3 mL mol⁻¹. (103), (109) This difference suggests that the picosecond to nanosecond structural changes associated with O₂ photodissociation from Hb differ from those for CO photodissociation, an observation that is supported by time-resolved resonance Raman spectroscopy studies. (98) For stripped CO-Hb, ΔH (19.4 kcal mol⁻¹) can be accounted for largely by the enthalpy of dissociation of the Fe-CO bond (17.5 kcal mol⁻¹), with the remainder (1.9 kcal mol⁻¹) being attributed to changes in protein structure. (110) For ligand dissociation from stripped oxyHb in the low temperature range, taking into account the electrostrictive contribution estimated to be -12.6 kcal mol⁻¹ and the further contributions outlined in Equation 4.2, we determine ΔH_{struc} to be 44.5 ± 19.4 kcal mol⁻¹. This value is 42.6 kcal mol⁻¹ more endothermic than ΔH_{struc} observed for photodissociation of CO from CO-Hb. This difference in structural energetics again indicates that there is a ligand

dependence of the structural relaxation that Hb undergoes within ~50 ns of ligand photodissociation.

For O₂ photodissociation from the oxyHb:L35 complex, the transition temperature of the V-shaped dependence is shifted from 16 to 12 °C. While the addition of L35 does not have an impact on ΔV measured for O₂ photodissociation in either temperature range, the values of ΔH for O₂ photodissociation in the low and high temperature ranges as compared to stripped oxyHb are more endothermic by 42.4 and 48.9 kcal mol⁻¹, respectively. The presence of 1.60 mM IHP eliminates the temperature dependence of ΔV and ΔH and produces a value of ΔV_{struc} of -11.6 mL mol⁻¹ for O₂ photodissociation from oxyHb. This ΔV_{struc} value is 7.7 mL mol⁻¹ larger than that associated with ligand photorelease in stripped oxyHb and nearly identical to that measured in the presence of 500 mM NaCl. The value of ΔH_{struc} is 110.3 ± 24.2 kcal mol⁻¹, which is 53.2 kcal mol⁻¹ more exothermic than in 500 mM NaCl, suggesting the presence of an additional relatively large endothermic contribution.

The use of 20 mM phosphate buffer, much like 0.50 mM L35, shifts the transition temperature of the V-shaped dependence from 16 to 12 °C. Compared to O₂ photodissociation from oxyHb in stripped conditions, there is no change in the measured value of ΔV_{obs} in the low temperature range, while in the high temperature range the volume contraction is not as large; its value raises from -18.8 ± 1.8 to -7.5 ± 0.8 mL mol⁻¹. Given that electrostriction of a charged species in water leads to a volume contraction, *(III)* *(II2)* this discrepancy can be attributed to the masking of electrostriction by the increased ionic strength of 20 mM phosphate as compared to 20 mM HEPES (40 mM and

3 mM, respectively). This explanation of masking of electrostriction can be extended to the changes in ΔH_{obs} ; in the high temperature range the measured enthalpy change for O₂ photodissociation from oxyHb in 20 mM phosphate buffer is 95.8 kcal mol⁻¹ more endothermic than in the stripped case owing to the reduction of the exothermic contribution of electrostriction. In the low temperature range the use of 20 mM phosphate buffer results in an enthalpy change which is 23.9 kcal mol⁻¹ more exothermic, which is attributable to the ability of inorganic phosphate to act as an effector of hemoglobin. (*II3*) As previously stated, the use of 100 mM phosphate buffer eliminates the V-shaped dependence, ΔV_{obs} for O₂ photodissociation in this buffer (5.2 ± 0.4 mL mol⁻¹) is slightly higher than that measured under stripped conditions (3.8 ± 0.2 mL mol⁻¹), while ΔH_{obs} is 43.2 kcal mol⁻¹ more exothermic at 19.3 ± 3.0 kcal mol⁻¹. According to Equation 4.2, only a small value of 1.3 ± 3.0 kcal mol⁻¹ remains for the enthalpy of structural changes and electrostriction. Interestingly, the ΔH_{obs} measured here is similar to that measured in the case of photodissociation of CO from CO-Hb (19.4 ± 1.2 kcal mol⁻¹), suggesting that the contribution which causes the photodissociation of O₂ from stripped oxyHb to be more endothermic by 43.1 kcal mol⁻¹ is eliminated.

4.2.3 Transient absorption results

The rate constants and quantum yields for geminate and bimolecular rebinding of O₂ to (O₂)₃Hb at 25 °C as determined by the maximum entropy method (MEM) (*II4*) and by exponential fitting are given in Tables 4.2, 4.3, and 4.4. The use of the MEM produces higher values for Φ_{bm} , but allows us to resolve multiple geminate and bimolecular rebinding kinetics; exponential fitting is unable to reliably distinguish more than three

kinetic processes. In the analysis of PAC data and in the discussion below we have used the values of Φ_{bm} produced by exponential fitting.

Under stripped conditions in 20 mM HEPES buffer at pH 7.0, we determine the quantum yield for bimolecular rebinding of O_2 to $(\text{O}_2)_3\text{Hb}$ (Φ_{bm}) to be 0.13. This value of

Table 4.2 Rate constants for geminate rebinding of O_2 to stripped $(\text{O}_2)_3\text{Hb}$ and $(\text{O}_2)_3\text{Hb}$:effector complexes at 25°C as determined by MEM analysis. Conditions: 30 μM Hb, 20 mM HEPES buffer, pH 7.0.

Conditions	k_{gem1} (μs^{-1})	A_{gem1} (%)	k_{gem2} (μs^{-1})	A_{gem2} (%)	k_{gem3} (μs^{-1})	A_{gem3} (%)
Stripped	46 ± 8	8.9	15 ± 2	10.9	N/A	N/A
0.5 M NaCl	54 ± 8	10.4	13 ± 1	8.8	N/A	N/A
1.6 mM IHP	40 ± 5	13.8	11 ± 2	12.4	3	1.6
0.50 mM L35	70 ± 12	11.1	18 ± 4	13.8	6	1.0
20mM phosphate	39 ± 3	16.0	10 ± 1	8.0	N/A	N/A
100mM phosphate	45 ± 9	12.2	14 ± 2	9.9	N/A	N/A

Table 4.3 Quantum yield and rate constants for bimolecular rebinding of O_2 to stripped $(\text{O}_2)_3\text{Hb}$ and $(\text{O}_2)_3\text{Hb}$:effector complexes at 25°C as determined by MEM analysis. Conditions: 30 μM Hb, 20 mM HEPES buffer, pH 7.0.

Conditions	Φ_{bm} (MEM)	k_{bm1} ($\mu\text{M}^{-1} \text{s}^{-1}$)	A_{bm1} (%)	k_{bm2} ($\mu\text{M}^{-1} \text{s}^{-1}$)	A_{bm2} (%)
Stripped	0.17	40 ± 10	13.7	5.7	2.9
0.5 M NaCl	0.26	46 ± 6	5.0	7.5	20.8
1.6 mM IHP	0.22	32 ± 7	14.8	4.9	7.6
0.50 mM L35	0.20	47 ± 6	14.9	6.0	4.6
20mM phosphate	0.20	52 ± 6	15.7	7.2	4.8
100mM phosphate	0.15	31 ± 6	13.1	6.1	1.9

Table 4.4 Rate constants for geminate and bimolecular rebinding of O₂ to stripped (O₂)₃Hb and (O₂)₃Hb:effector complexes at 25°C as determined by fitting to a three exponential decay model. Conditions: 30 μM Hb, 20 mM HEPES buffer, pH 7.0.

Conditions	Φ_{bm} (Exp)	k_{gem} (μs^{-1})	A_{gem} (%)	k_{bm} ($\mu\text{M}^{-1} \text{s}^{-1}$)	A_{bm} (%)
Stripped	0.13	19.9	7.1	42.7	5.6
0.5 M NaCl	0.19	18.1	8.6	27.2	10.0
1.6 mM IHP	0.22	15.4	12.6	44.6	9.4
0.50 mM L35	0.15	20.5	8.2	43.1	6.8
20mM phosphate	0.16	19.9	9.3	52.2	7.0
100mM phosphate	0.12	21.9	7.5	31.4	5.0

Φ_{bm} is identical to that previously measured by Lepeshkevich et al. for rebinding of O₂ to myoglobin (Mb). (*115*) The effects of 0.50 mM L35 and 20 mM phosphate are modest, causing an increase of Φ_{bm} to 0.15 and 0.16, respectively. Inositol hexakisphosphate and 0.5 M NaCl have stronger effects, increasing Φ_{bm} to 0.22 and 0.19 respectively, consistent with the effect of increased ionic strength on Φ_{bm} for the rebinding of CO to Hb. (*116*) Interestingly, the quantum yield measured for O₂ bimolecular rebinding to Hb in 100 mM phosphate buffer ($\Phi_{\text{bm}} = 0.12$) is comparable to that for stripped Hb despite the observed effect of 20 mM phosphate buffer. The increase in Φ_{bm} observed for effector:Hb complexes is concurrent with a decrease in geminate rebinding quantum yield (Φ_{gem}), since $\Phi_{\text{gem}} + \Phi_{\text{bm}} = 1$, indicating that the binding of effectors to oxyHb increases the extent to which dissociated O₂ is able to escape from the protein.

The rate constants for geminate and bimolecular rebinding of O₂ to (O₂)₃Hb as determined by the MEM are shown in Tables 4.2 and 4.3. We are able to resolve two geminate rebinding steps with time constants of approximately 20 and 75 ns in all samples. In the stripped case, we resolve two steps with rate constants of 46 ± 8 and $15 \pm 2 \mu\text{s}^{-1}$ and

corresponding time constants of ~ 22 and ~ 67 ns. The addition of effectors has only a modest effect on the observed geminate rebinding rate constants, except for 0.50 mM L35, which increases the rate constants to 70 ± 12 and $18 \pm 4 \mu\text{s}^{-1}$ with corresponding time constants of ~ 14 and ~ 56 ns. In the case of IHP- or L35-bound oxyHb we are able to observe a third geminate step with a very low fractional contribution of $\sim 1\%$. This relatively slow kinetic process may represent the geminate rebinding of O_2 which has traversed interior hydrophobic channels within the protein before rebinding, as predicted by computational simulations. (97)

We were also able to resolve multiple rate constants for bimolecular rebinding of O_2 to $(\text{O}_2)_3\text{Hb}$ (Table 4.3). For O_2 rebinding to $(\text{O}_2)_3\text{Hb}$ under stripped conditions, we determine rate constants of 40 ± 10 and $5.7 \pm 3 \mu\text{M}^{-1} \text{s}^{-1}$. These parameters are identical to those previously measured by rebinding of O_2 to the α - and β -chains of Hb. (117) While the addition of effectors has no measurable impact on the rates of bimolecular rebinding, the addition of 0.5 M NaCl increases the amount of O_2 rebinding via the slower pathway. The ratio of the fractional percentages of the faster and slower steps ($A_{\text{bm1}}:A_{\text{bm2}}$) shifts from approximately 5:1 under stripped conditions to 1:4 in the presence of 0.5 M NaCl.

4.3 Discussion

Previous spectroscopic studies have demonstrated that upon photodissociation of a single O_2 from the $(\text{O}_2)_4\text{Hb}$ complex, the ligand may rebind to the heme iron in the process of geminate rebinding (118) or escape to the solvent through the distal histidine gate. (96) Concurrently, the protein undergoes a structural relaxation of the heme group where the heme iron shifts out of the heme plane, and a tertiary relaxation of the E and F helices. (98)

These processes are responsible for the thermodynamic parameters we observe using PAC. The ligand may also undergo bimolecular rebinding or a quaternary structural transition from the R to the T state, but these occur outside the range of our PAC instrumentation, typically on the order of hundreds of microseconds. (117)

4.3.1 Temperature dependence of ΔH and ΔV

An important feature of the PAC data is the presence of two different linear trends for oxyHb under stripped conditions with a transition at 16 °C as shown in Figure 4.3. The replacement of 20 mM HEPES buffer with 20 mM phosphate buffer or the addition of the effector L35 shifts the temperature of the transition to 12 °C, suggesting that the presence of phosphate or the binding of the effector L35 to the protein, either within the central cavity near the $\alpha_1\beta_1/\alpha_2\beta_2$ interface or on the surface near the heme cavity of the α subunit, (95) has an impact on the temperature dependence of the observed volume and enthalpy changes. The V-shaped dependence does not occur at pH 6 or in the presence of 500 mM NaCl or 1.6 mM IHP. These data indicate that the thermodynamic parameters observed within ~50 ns of O₂ photorelease are significantly different above and below the transition temperature and are also strongly impacted by pH, ionic strength, and the presence of effectors. In addition, we have observed a temperature dependence of thermodynamic parameters for dissociation of CO from *Oryza sativa* (rice) hemoglobin which is also eliminated in the presence of 0.5 M NaCl or at pH 6. Rice Hb is a type 1 non-symbiotic hemoglobin which exhibits hexacoordination and crystallizes as a symmetrical homodimer. (41) Rice Hb primarily forms monomers *in vitro* at the ~25 μ M concentration used in PAC studies. (41) Therefore, the formation of quaternary structure is not necessary to observe the temperature dependent phenomenon in heme proteins.

From our data, we suggest that the observed V-shaped dependence of our PAC data is the result of temperature-dependent protonation of Bohr groups (particularly His residues) and formation/destruction of salt bridges in the $\alpha_1\beta_1/\alpha_2\beta_2$ interfaces. The temperature dependence of His ionization constants has been previously observed in free His and His derivatives (81) as well as in myoglobin. (119) The protonation state of the His residues, which are important Bohr groups, controls the formation of salt bridges in the intradimer interfaces which affect the structural enthalpy and volume change associated with O₂ photodissociation from Hb. Effectors impact the measured thermodynamic parameters and shift the temperature of the V-shaped dependence (or eliminate it) by interaction with His residues and other Bohr groups in the intradimer interfaces or on the protein surface and by interfering with formation of intradimer salt bridges by specific binding or electrostatic screening. The network of salt bridges has been proposed as an intradimer communication pathway and is known to modulate Hb function, as mutation of the key residue β Gln131 results in lowered oxygen affinity and increased cooperativity. (120)

The strongest evidence to support the link between Bohr groups and the V-shaped dependence comes from our PAC studies of O₂ photodissociation from Hb at pH 6 and in the presence of 500 mM NaCl. At pH 6 there is no V-shaped dependence of the measured thermodynamic parameters. The lack of the dependence suggests that the protonation of amino acid residues plays an important role in observing the V-shape. Histidine is the only residue whose average pK_a value (6.6 ± 1.0) is between 6.0 and 7.0, (83) and many His residues in the intradimer interface (121) and on the protein surface fall into this range, (86) (122) making them partially responsible for the alkaline Bohr effect.

In this view, the thermodynamic parameters we observe for the photodissociation of O₂ from stripped Hb below 16 °C the result of the previously mentioned contributions: O₂ migration from the protein matrix, distal pocket hydration, scission of the Fe-O₂ bond, solvation of O₂, and structural changes within the protein. Increasing the temperature causes a decrease of pK_a values of His residues, leading to increasing deprotonation of these residues and disruption of salt bridges in the intradimer interface. Photolysis of O₂ from Hb in this disrupted state results in the exposure of charged species to the water-filled central cavity of Hb causing a large exothermic contribution to ΔH (-142.2 ± 12.3 kcal mol⁻¹) and a large negative contribution (-43.1 ± 1.8 mL mol⁻¹) to ΔV. These effects have been previously observed for the creation of charges in water using photothermal methods (*112*) and are a result of the reorganization of water molecules to form a hydration shell around the charged species. These effects on ΔH and ΔV are not observed in high ionic strength solution because of the screening of electrostatic interactions; the relevant salt bridges are never formed. It is also not observed at pH 6 because the relevant residues remain protonated throughout the temperature range despite the decrease in pK_a.

The impact of effectors on the observed thermodynamic parameters The exogenous effector L35 has been observed to bind in the α₁β₁ interface of both horse CO-Hb (PDB 2D5X) (*95*) and human deoxy Hb (PDB 2D60), (*95*) similar to the location of bezafibrate binding. (*123*) Here, the molecule interferes with a network of salt bridges between several static water molecules and residues including αLys99, αHis103, αHis122, βGlu101, and βGln131. Upon effector binding one of the chlorines of the L35 molecule is positioned closely to αHis103, which has been identified as a potential contributor to the Bohr effect in Hb. (*121*) The interaction of L35 with αHis103 may be sufficient to lower its pK_a,

causing it to become deprotonated at lower temperatures, contributing to the observed shift of the V-shaped dependence. The other chlorine of the L35 molecule is positioned close to the $\beta\text{Glu101}-\alpha\text{Lys99}$ salt bridge and could prevent its formation, eliminating its contribution to the observed thermodynamic parameters. The carboxyl group of L35 is also positioned closely to αSer131 , a residue which along with the terminal amine of αVal1 forms a chloride binding site and takes part in the chloride-linked Bohr effect. Overall, the mechanisms by which L35 affects the protein are all tied to interactions with protonable residues and disruption of salt bridges in the intradimer interfaces.

The other heterotropic effector in our study, IHP, binds to the $\beta_1\beta_2$ cleft of Hb where positively-charged residues form a favorable environment for the binding of negatively-charged effectors, including the endogenous effector BPG (PDB 1B86). (*124*) The residues βVal1 and βLys82 , which also bind chloride, are primarily responsible for the binding of IHP. The Bohr group βHis146 is also in close proximity.

4.3.2 Ligand dependence of ΔH and ΔV

Analysis of the PAC data raises the question of why we do not see a temperature dependence of stripped CO-Hb, as shown in Figure 4.3, Left. First, we must explain the observed parameters. Our studies on CO photodissociation (Table 4.1) agree with values reported by Peters et al. (*37*) and use empirically determined values for Φ_{bm} across the entire temperature range of our PAC measurement (data not shown). The results of Chen et al. are similar to what we observe for human oxyHb in phosphate buffer (Table 4.1),

though they did not observe a temperature dependence of the thermodynamic parameters ΔH and ΔV , likely due to the use of 50 mM phosphate buffer.

Since we have asserted that under stripped conditions and at temperatures above 16°C oxyHb undergoes a breakage of intradimer salt bridges, we must compare the low temperature oxyHb data to that for CO-Hb. ΔV is $\sim 16 \text{ mL mol}^{-1}$ larger in CO-Hb, which can be partially accounted for by the difference in partial molar volume between the dissociated ligands, 3 mL mol^{-1} . (103) (109) Therefore, in stripped oxyHb we observe that the process of ligand photodissociation is associated with a volume contraction which is 13 mL mol^{-1} smaller in than in CO-Hb. For CO-Hb, ΔH can be accounted for largely by the enthalpy of dissociation of the Fe-CO bond ($17.5 \text{ kcal mol}^{-1}$). (110) For oxyHb in stripped conditions, photodissociation of O_2 is $\sim 40 \text{ kcal mol}^{-1}$ more endothermic in the low temperature range. Including an electrostrictive contribution estimated to be $-16 \text{ kcal mol}^{-1}$ yields a value of 57 kcal mol^{-1} for the remaining processes.

The residual thermodynamic contribution must be assigned to those processes that have not already been accounted for: tertiary structural relaxation and ligand escape from the protein matrix. Mutation studies have shown that in human Hb, the distal His gate serves as the primary route for ligand migration into and out of the protein, (96) so we expect both ligands to contribute similarly to ΔH and ΔV . The ligand dependence of the thermodynamic parameters must therefore be explained by differing tertiary structural relaxation processes.

Given the wealth of structural knowledge of Hb, we can speculate as to the specific tertiary relaxations involved. It is known that the crystal structures of oxyHb and CO-Hb

differences in the distal heme pocket, where O₂ is able to form a hydrogen bond with the distal His. (125) (126) The presence of this hydrogen bond cross-links the E and F helices, restraining their motions. (127) The time-resolved resonance Raman studies of Murakawa et al. (98) demonstrated ligand-dependent spectral changes in ligated Hb, which were speculated to be caused by motions of the EF helical region.

The putative mechanism to explain the ligand dependence of thermodynamic parameters can be summarized thusly: in the absence of effectors which affect Bohr groups on the protein surface and in the intradimer interface, dissociation of a single O₂ molecule from (O₂)₄Hb results in a structural relaxation due to dissociation of the O₂-distal His hydrogen bond and subsequent tertiary relaxation of the EF helical region which is not observed in the case of CO photodissociation.

4.3.3 Bimolecular quantum yield

The quantum yields for bimolecular rebinding of O₂ to (O₂)₃Hb are increased compared to stripped oxyHb in all oxyHb:effector complexes, excluding 100 mM phosphate. This increase of Φ_{bm} indicates an increase in escape of photodissociated O₂ from the heme pocket. The distal HisE7 gate serves as the primary ligand migration pathway in Hb (96) and therefore has a large role in determining Φ_{bm} . Increasing temperature is known to decrease oxygen affinity (increase P₅₀) and weaken the distal His hydrogen bond, which stabilizes O₂ bound to the heme iron. (128) Also, we have observed an increase of Φ_{bm} with temperature (data not shown). The effects of temperature on P₅₀ and Φ_{bm} can both be linked to increased mobility of the distal His side chains due to thermal

fluctuations of the protein structure leading to a weakening of the distal His-O₂ hydrogen bond and subsequent decrease of oxygen affinity and enhancement of escape of photodissociated O₂. Since the allosteric effectors L35, IHP, Cl⁻, and to a lesser extent 20 mM phosphate also decrease oxygen affinity and increase quantum yield, we propose that the underlying mechanism is the same, and that changes in structural dynamics induced by the binding of effectors are ultimately responsible for the observed increase of Φ_{bm} .

The P₅₀ values for oxyHb in the presence of 0.50 mM L35 and a saturating concentration of IHP have been published by Marden et al. (129) If we estimate the P₅₀ for the oxyHb:L35 complex assuming a 55% fractional saturation as we did for our PAC data, we calculate a value of 82.1 mmHg, very similar to the value of 78.0 mmHg published for IHP. It is interesting to note that the values of Φ_{bm} for L35 and IHP (0.184 and 0.185) are also similar. Here we see a parallel between the values of Φ_{bm} and P₅₀; two effectors with different binding sites and radically different structures show a correlation in their impact on both bimolecular quantum yield and oxygen affinity. This correlation suggests that these effectors may be inducing the same change in structural dynamics, i.e., the dynamic states induced by binding of L35, IHP, and perhaps other effectors may be more alike than they are different. This similarity is consistent with the basic principles of the tertiary two-state model. (25) Unfortunately, structural dynamics data for L35-bound Hb is not available, preventing us from directly comparing the effects of organic phosphates to those of bezafibrate-related compounds.

4.3.4 Rate constants for geminate rebinding

The two first order rate constants we resolve (k_{gem1} and k_{gem2}) for oxyHb correspond to the slowest geminate rebinding processes which have been previously observed in oxyHb (117) and CO-Hb in silica gels. (130) It is known that direct geminate rebinding of O_2 to Fe^{2+} can occur in at least one step as fast as 1 ns. (117) It is also known that Hb contains hydrophobic cavities near the distal pocket analogous to those found in Mb (96). Sottini et al. used computational modeling to identify hydrophobic cavity docking sites for CO in the distal pockets of the α and β subunits which were used to explain the multiphasic rebinding behavior of CO in silica gel. (130) The potential role of these cavities was also explored by Lepeshkevich et al., (97) who presented a kinetic model and microscopic rate constants based on laser spectroscopy and molecular dynamics data.

Using these data, we can estimate the rate constants for O_2 geminate rebinding after migrating to and from the closest two systems of cavities and after migrating deeper into the protein matrix, to the Xe6 site. We estimate rate constants of $84 \mu\text{s}^{-1}$ and $23 \mu\text{s}^{-1}$ for the short and long pathways. These values are faster than our values for k_{gem1} and k_{gem2} as shown in Table 4.2. These faster rate constants is possibly a result of the fact that our observed parameters are averages of those for the α and β subunits, while the aforementioned study concerned the isolated α subunit. The correlation between these data provides a potential explanation for our observed geminate rebinding parameters.

This explanation is contradicted by the study of Birukou et al., who concluded from kinetics studies of CO geminate rebinding to Hb mutants that the cavities found in the Hb distal pocket do not provide a location for docking of photodissociated ligands, instead

suggesting that rebinding occurs from positions closer to the heme iron. (96) However, the aforementioned study did not analyze the geminate recombination of O₂ and operated under the assumption that the ligand migration pathway for O₂ and CO should be the same. This assumption regarding O₂ and CO migration may not hold true, given the differences between the two ligand molecules and in structural dynamics of Hb upon photodissociation as observed in our study and others. (98)

The effectors studied mostly have small effects on the geminate rebinding rate constants. L35 shows the largest effect, increasing both rate constants. The impact of L35 supports the existence of a communication pathway between the intradimeric L35 binding site and the distal pocket, where geminate rebinding occurs. Since we have suggested that hydrophobic cavities near the heme pocket are responsible for the observed geminate rebinding kinetics, the impact of effectors on these parameters should be due to an effector-linked modulation of these cavities. However, the crystal structures of L35:Hb complexes by Yokoyama et al. show that binding of L35 does not induce significant tertiary or quaternary structural changes in the tetramer. (95) Once again the modulation of tertiary structural dynamics may provide an explanation.

The binding site of L35 within the central cavity of Hb may give rise to its particularly strong effect on geminate rebinding rate constants. The Xe2, Xe4, and Xe5 cavities have been proposed as interior binding sites for O₂ in the α subunit of Hb (97) with Xe4 being especially important in Mb, which more closely resembles the α subunit. (131) Many of the residues which form these cavities, including Phe98, Leu101, Ser102, Leu105, Thr108, and Leu109 (97) are located on the same helix and within a few residues of Lys99

and His103, both of which have direct interactions with L35 in the horse CO-Hb:L35 crystal structure (PDB 2D5X) (95) and are members of the hydrogen bond network in the intradimer interface of ligated Hb.

Given the above information, we propose a mechanism wherein the binding of L35 to residues in the G-helix (and perhaps others) of the α subunit leads to a modulation of the structural dynamics of the Xe cavities where O₂ may potentially reside upon photodissociation which is communicated through the protein backbone and the intra- and interhelix hydrogen bonds which stabilize the protein structure. The proposed mechanism accounts for the effect of L35 on k_{gem1} and k_{gem2} and agrees with that given to explain thermodynamic parameters associated with O₂ photodissociation, as monitored by PAC. The bezafibrate-based drug L35 also interacts with residues of the β subunit in the intradimer interface such as Asn108, suggesting a mechanism by which the β subunit might also be affected.

4.4 Conclusion

Overall, analysis of the PAC and TA data reveals that thermodynamic and kinetic parameters associated with ligand photodissociation from human Hb are strongly affected by the binding of exogenous allosteric effectors. The V-shaped temperature dependence phenomenon observed for the photodissociation of O₂ from the protein under stripped conditions using PAC is affected by the ionic strength of the solution and the presence of the exogenous effectors L35 and IHP. These effectors also impact rate constants for

geminate rebinding of O₂ suggesting that binding of these effectors has an allosteric effect on the primary ligand migration pathway and the EF helical region.

The temperature-dependent transition which occurs at 16 °C may not occur *in vivo* due to the presence of endogenous allosteric effectors such as 2,3-bisphosphoglycerate and the average human body temperature of 37 °C. This phenomenon may therefore be an evolutionary holdover resulting from the common origin of heme proteins in higher organisms. This idea is supported by the observation of a temperature-dependent transition for photodissociation of CO in *Oryza sativa* (rice) type 1 non-symbiotic hemoglobin (rHb1) using PAC as seen in chapter 3. Though the identity of the photodissociated ligand differs between these studies, the common feature of a strong hydrogen bond between the distal His residue and the bound ligand suggests a mechanism by which the occurrence of the temperature-dependent transition may be preserved.

5 IMPACT OF AZOLE DRUGS ON ENERGETICS, KINETICS, AND LIGAND MIGRATION PATHWAYS OF CO PHOTODISSOCIATION IN BACTERIAL FLAVOHEMOGLOBINS

5.1 Introduction

Bacterial flavohemoglobins (fHbs) are a family of heme proteins found in a large number of modern bacteria. They are composed of an α -helical heme-binding domain with a typical heme globin structure fused to a flavin-binding domain which binds the cofactors NADPH and FADH. It has been well established that fHbs exhibit nitric oxide dioxygenase (NOD) activity which is facilitated by electron-donating cofactors bound to the flavin-binding domain. (*132*) The NOD function has primarily been implicated in modulation of NO signaling and in protection of pathogenic bacteria from NO production by phagocytes within the immune systems of host organisms. (*7*) NO produced by phagocytes can damage the bacterial cell by direct nitrosylation of enzymes and nucleic acids (*133*) or by decomposition to peroxynitrite and other reactive oxygen species (ROS). (*134*) Therefore, NOD activity of fHbs is responsible for enhanced bacterial survival under oxidative stress conditions. (*133*)

Two NOD mechanisms have been proposed for fHbs. In the first, O₂ diffuses into the heme binding pocket and binds to the ferrous heme iron, after which NO may diffuse into the active site where dioxygenation occurs, oxidizing the heme iron to the ferrous form and forming an unstable peroxynitrite intermediate which decays to nitrate (*7*). In the second, NO binds to the ferric heme iron first forming Fe(III)-NO, whereupon it is reduced to Fe(II)-NO and reacts with oxygen to form nitrate (*135*). In both mechanisms, reduction of the heme iron by electron transfer from FADH occurs, possibly involving the heme

propionate groups as previously proposed. (136) (137) Electron migration and diffusion of gaseous diatomic molecules into the heme binding pocket are essential for the NOD activity of fHbs.

This activity has been shown to be strongly inhibited by azole-based antifungal drugs including ketoconazole, miconazole, and econazole. (138) These compounds bind with high affinity to fHbs from *Cupriavidus necator* (FHP) - formerly known as *Ralstonia eutropha* – and *Staphylococcus aureus* (HMP_{sa}). (139) The crystal structures have been determined for ketoconazole, miconazole, and econazole bound to the Fe(III) form of FHP in the absence of gaseous ligands, showing that these drugs are able to enter the distal heme pocket where the imidazole group of the drug forms a coordination bond with the heme iron. (49) This binding location is not expected for the ligand-bound form of the protein, given that the presence of bound diatomic gaseous molecules would prevent coordination of the imidazole group of the drug. This raises the question of how azole drugs interact with the ligand-bound forms of fHbs in general.

Herein we have used photoacoustic calorimetry (PAC) and transient absorption spectroscopy (TA) in combination with classical molecular dynamics (cMD) simulations utilizing a locally enhanced sampling (LES) algorithm to characterize the migration of CO within the protein matrix of wild-type bacterial flavohemoglobins from *C. necator* and *S. aureus* in the presence and absence of ketoconazole and miconazole as well as the binding sites of azole drugs within these proteins. We aim to predict the molecular mechanism of how the binding of azole drugs to fHbs results in inhibition of NOD activity in fHbs in order to allow for the targeting of future drug compounds.

5.2 Results

5.2.1 UV-vis Spectroscopy

The absorption spectra of for met-, deoxy-, and CO-FHP in the absence ofazole drugs are shown in Figure 5.1. The spectra resemble the absorption spectra of other penta-coordinate heme proteins with the Soret band of met-FHP located at 395 nm and additional Q bands situated at 458 nm, 486 nm and 646 nm. Upon heme iron reduction, the Soret band undergoes a bathochromic shift to 437 nm and a new band appears at 563 nm. The Soret band for CO-FHP is narrow with an absorption maximum at 424 nm and two Q bands at 540 nm and 572 nm consistent with heme iron coordination to the proximal histidine with CO at the distal position.

Upon addition of 14 μM ketoconazole, the Soret band for met-FHP undergoes a red shift to 409 nm with a shoulder located at 393 nm (Figure 5.2) indicating that the imidazole group of ketoconazole coordinates to the heme iron (Figure 5.3). This is more evident from the emission spectrum of deoxy-FHP in the presence of ketoconazole that exhibits a Soret

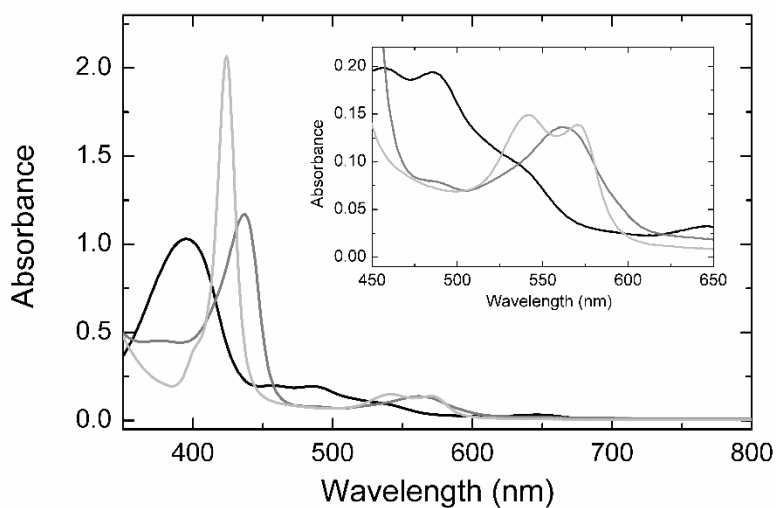


Figure 5.1 UV-vis traces for met-, deoxy-, and CO-FHP in the absence ofazole drugs.

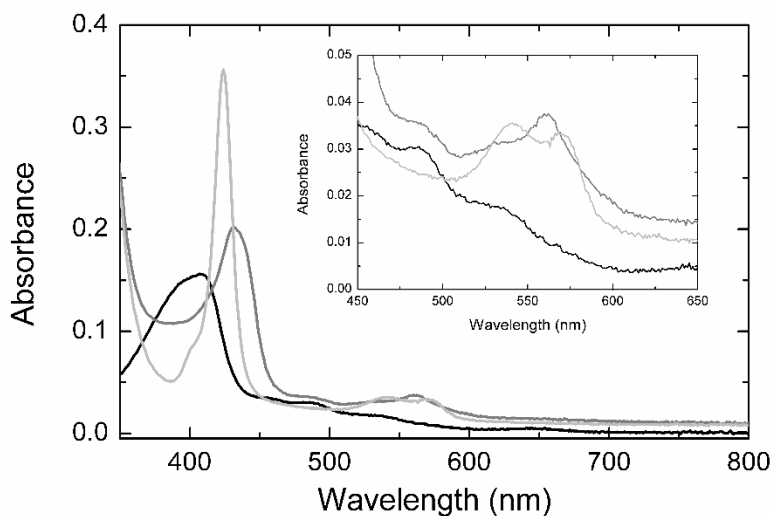


Figure 5.2 UV-vis traces for met-, deoxy-, and CO-FHP in the presence of 14 μM ketoconazole.

band maximum at 430 nm and a Q band at 560 nm with a shoulder at 530 nm. This absorption spectrum is consistent with a fraction of deoxy-FHP containing heme iron in a low spin, hexa-coordinated state, as observed previously for vertebrate hexa-coordinate globins with histidine as the proximal and distal ligands. In addition, binding of CO to

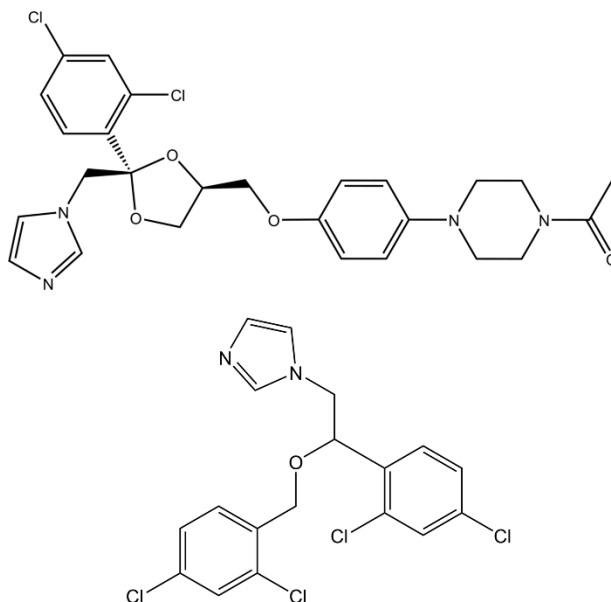


Figure 5.3 Chemical structures of ketoconazole (top) and miconazole (bottom).

deoxy-FHP leads to an absorption spectrum that is identical to that of CO-FHP in the absence of ketoconazole, indicating that the presence of the azole drug has a negligible impact on the electronic structure of the FHP heme group in the presence of CO.

The absorption spectra of FHP measured in the presence of 408 μM miconazole (Figure 5.4) are analogous to those determined for FHP in the presence of ketoconazole. Notably, the absorption spectrum of deoxy-FHP shows a Soret band maximum at 430 nm and two Q bands at 532 nm and 562 nm, indicating that the majority of protein is hexa-coordinate with the imidazole group of miconazole as the sixth axial ligand for the heme iron. This is consistent with the increased fraction of miconazole bound to FHP compared to ketoconazole. Based on the dissociation constants (K_D) that have been determined previously for ketoconazole and miconazole (*139*) it can be estimated that approximately 49% and 99% of FHP is in the drug-bound form, respectively. The absorption spectra of HMP_{sa} in the absence and presence of the azole drugs are analogous to those determined for FHP indicating similar interactions between the azole drugs and the heme iron.

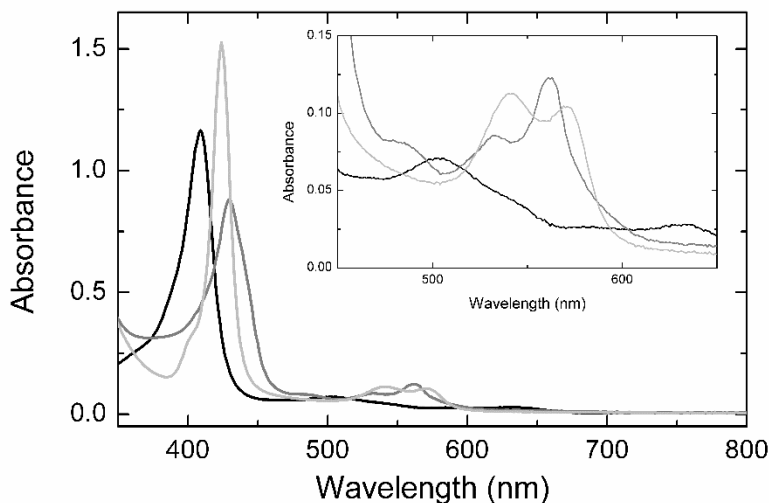


Figure 5.4 UV-vis traces for met-, deoxy-, and CO-FHP in the presence of 408 μM miconazole.

5.2.2 PAC & TA Results

To characterize the impact of azole drug association to the heme distal pocket on the interactions of FHP and HMP_{Sa} with diatomic ligands, we have applied PAC which allows us to monitor the dynamic and energetics of structural changes associated with ligand dissociation from heme proteins on nanosecond to microsecond timescale. Photoacoustic traces for CO photo-release from FHP in the absence of azole drugs are shown in Figure 5.5. The absence of a phase shift between the acoustic wave for the sample and the acoustic wave for the reference indicates that the photolysis of the CO-Fe bond and the subsequent ligand escape from the protein matrix into surrounding solvent is fast ($\tau < 50$ ns). Analogous photoacoustic traces with an absence of the shift between the sample acoustic wave and the reference acoustic wave were determined for CO photo-release from FHP in the presence of ketoconazole and miconazole and for CO photo-release from HMP_{Sa} in the presence and absence of both azole drugs (data not shown).

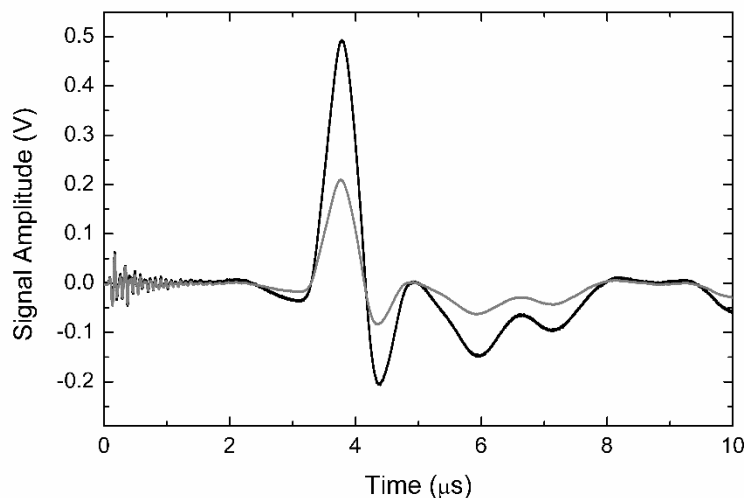


Figure 5.5 Example PAC traces for dissociation of CO from CO-FHP (black) and 4SP reference compound (grey) at 20 °C in 10 mM sodium phosphate and 10 mM potassium chloride buffer, pH 7.5.

As described in the Methods and Materials section, the volume and enthalpy change associated with ligand escape from FHP and HMP_{Sa} can be determined by plotting the ratio of the amplitude of the sample acoustic wave as a function of the temperature dependent factor ($C_p\rho/\beta$) as shown in Figure 5.6 for CO photo-release from FHP in the presence and absence ofazole drugs and in Figure 5.7 for CO photo-dissociation from HMP_{Sa} in the presence and absence ofazole drugs.

For both proteins, the plots were analyzed according to Equation 2.6 and the extrapolated volume and enthalpy changes are listed in Table 5.1. For FHP and HMP_{Sa}, the volume and enthalpy changes accompanying CO photo-release from the heme iron and subsequent ligand escape from the protein matrix are large and positive, pointing towards similar structural changes due to the transition from CO bound, hexa-coordinate protein to ligand free, penta-coordinate protein (see below). CO photo-dissociation in the presence of 14 μM ketoconazole leads to an exothermic enthalpy change of $-9.0 \pm 11.7 \text{ kcal mol}^{-1}$ and

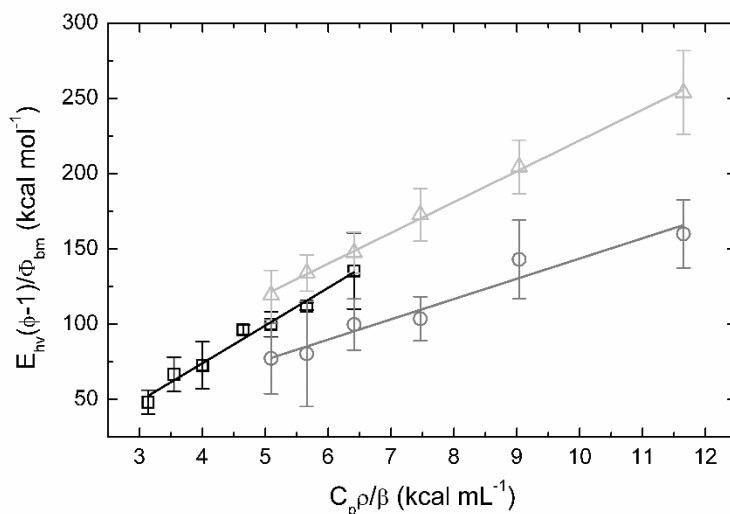


Figure 5.6 Plots of $C_p\rho/\beta$ vs. $E_{hv}(\phi-1)/\Phi_{bm}$ for photo-dissociation of CO from CO-FHP in the absence of drug compounds (black), with 14 μM ketoconazole (gray), and with 408 μM miconazole (light gray).

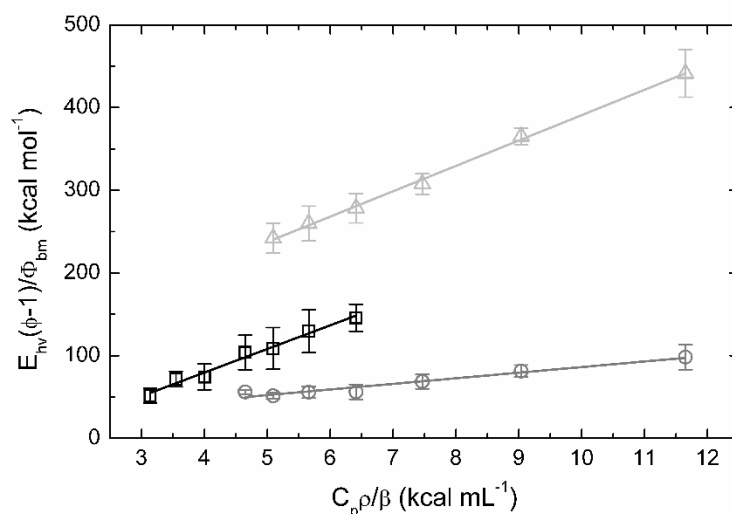


Figure 5.7 Plots of $C_{p\rho/\beta}$ vs. $E_{hv}(\phi-1)/\Phi_{bm}$ for photo-dissociation of CO from CO-HMP_{Sa} in the absence of drug compounds (black), with 14 μ M ketoconazole (gray), and with 408 μ M miconazole (light gray).

a smaller volume change of 13.5 ± 1.5 mL mol⁻¹. Due to a lower solubility of ketoconazole and a lower equilibrium binding constant for ketoconazole ($K_D = 10$ μ M for FHP and K_D

Table 5.1 Thermodynamic parameters determined using PAC for photo-release of CO from CO-bound flavohemoglobins from *Ralstonia eutropha* (FHP) and *Staphylococcus aureus* (HMP_{Sa}) in the presence and absence of ketoconazole and miconazole. Asterisks indicate hypothetical values and correspond to ΔH_{bound} and ΔV_{bound} .

Protein	Drug Identity	Drug Conc. 20 °C (μ M)	Percent Drug-Bound	ΔH (kcal mol ⁻¹)	ΔV (mL mol ⁻¹)	Φ_{bm} (20 °C)
CO-FHP	None	0	0	26.2 ± 7.0	25.0 ± 1.5	0.50
	Ketoconazole	14	49	-9.0 ± 11.7	13.5 ± 1.5	0.41
	Ketoconazole	500*	98*	-42.3*	2.6*	0.32*
	Miconazole	409	99	-17.4 ± 3.4	20.4 ± 0.4	0.64
CO-HMP _{Sa}	None	0	0	34.7 ± 8.0	28.6 ± 1.7	0.31
	Ketoconazole	14	45	-12.9 ± 3.4	7.4 ± 0.4	0.52
	Ketoconazole	500*	98*	-52.6*	-10.3*	0.65*
	Miconazole	409	99	-83.9 ± 5.4	30.7 ± 0.7	0.34

= 12 μ M for HMP_{Sa}), (139) the thermodynamic parameters were determined for a sample with a fraction of protein (~ 49%) having ketoconazole bound. In this case, the observed volume or enthalpy change can be expressed using Equations 5.1 and 5.2:

$$\Delta V = f_{free}\Delta V_{free} + f_{bound}\Delta V_{bound} \quad (5.1)$$

where f_{free} corresponds to the fraction of protein without drug, f_{bound} corresponds to the fraction of protein with the drug bound, ΔV_{free} corresponds to the volume change determined in the absence of drug and ΔV_{bound} corresponds to the volume change for ligand dissociation from the protein with the drug bound. In a similar way, the observed enthalpy change for a protein sample with a fraction of protein having a drug bound can be expressed as:

$$\Delta H = f_{free}\Delta H_{free} + f_{bound}\Delta H_{bound} \quad (5.2)$$

where ΔH_{free} corresponds to the volume change determined in the absence of drug and ΔH_{bound} corresponds to the volume change for the ligand dissociation from the protein with the drug bound.

Using the equations above, the reaction volume and enthalpy change for CO photo-dissociation from FHP or HMP_{Sa} saturated (ΔV_{bound} & ΔH_{bound}) with ketoconazole can be determined; the reaction parameters are listed in Table 5.1. Interestingly, the volume and enthalpy changes associated with CO photo-dissociation from FHP or HMP_{Sa} in the presence of miconazole differ from those determined in the presence of ketoconazole suggesting a difference between the structures of drug-bound FHP and HMP_{Sa} in the deoxy- or CO-bound form. Binding ofazole drugs to both proteins results in a more

exothermic ΔH . ΔV observed for CO photo-dissociation in FHP and HMP_{Sa} is much lower in the presence of ketoconazole with $\Delta\Delta V$ equal to -22.4 and -38.9 mL mol⁻¹, respectively, if we estimate using ΔV_{bound} . Only small changes are observed in the presence of miconazole with $\Delta\Delta V$ equal to -4.6 and 2.1 mL mol⁻¹ for FHP and HMP_{Sa}.

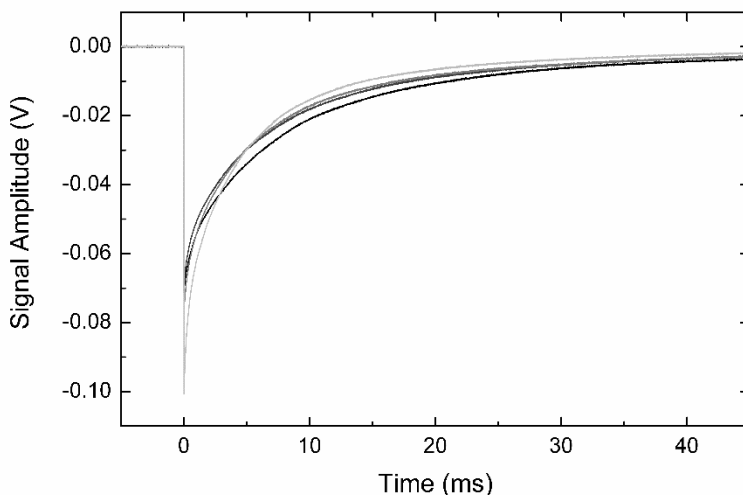


Figure 5.8 Example TA traces for bimolecular rebinding of CO to deoxy-FHP in the absence ofazole drugs at 16 °C (black), 20 °C (dark gray), 26 °C (grey) and 35 °C (light gray).

In addition to characterizing the reaction thermodynamic parameters, the rate constants for bimolecular rebinding of CO to FHP or HMP_{Sa} in the absence/presence ofazole drugs were determined as a function of temperature using TA and the absorption traces detected at 447 nm are demonstrated in Figure 5.8 for CO rebinding to deoxy FHP in the absence ofazole drugs. The absorption traces were analyzed using a multi-exponential decay model and CO rebinding to the heme iron is tri-exponential with rate constants of 2 $\mu\text{M s}^{-1}$, 0.18 $\mu\text{M s}^{-1}$, and 0.06 $\mu\text{M s}^{-1}$. Association of miconazole does not impact the rates for bimolecular ligand rebinding. On the other hand, the rate constants for the ligand binding in the presence of the ketoconazole are approximately two times faster

than in the absence of the drug suggesting that association of ketoconazole opens the heme binding pocket. The heterogeneous ligand rebinding observed here indicates that the protein can adopt multiple conformations under the experimental conditions with each conformation having a distinct rate constant for CO rebinding and/or there are several ligand migration pathways with distinct rate constants for CO rebinding (*vide infra*).

In the case of CO rebinding to HMP_{Sa}, an additional phase with time constant of ~9 μ s was detected. This phase represents a geminate CO rebinding to the heme iron as the time constant for this phase is independent of CO concentration. The presence of such a slow geminate rebinding in this protein indicates that the photodissociated ligand is trapped within the protein matrix likely due to the presence of hydrophobic cavities. These data indicate that the distribution of the hydrophobic cavities is distinct between FHP and HMP_{Sa}. In a similar way as observed for FHP, the presence of azole drugs has only a minor

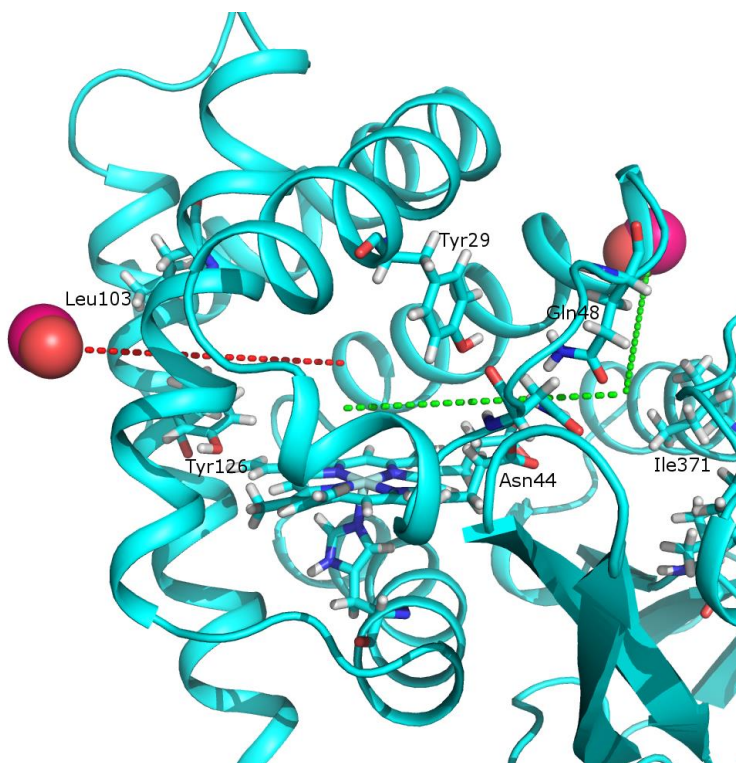


Figure 5.9 Escape pathways found in LES-enabled simulation of CO escape from FHP. Pathways A and E are shown as red and green dashed lines respectively. CO molecules are shown in red and magenta.

impact on the rate constants for CO rebinding to HMP_{sa}, with CO rebinding being faster for ketoconazole-bound FHP.

5.2.3 Classical Molecular Dynamics

5.2.3.1 CO migration pathways within FHP

Using locally enhanced sampling in NAMD 2.11, we were able to observe the dissociation of all 20 enhanced CO ligands from the heme binding pocket. All 20 CO molecules were tracked throughout the 30 ns MD simulation to determine their exit pathway from the protein matrix. 21 separate CO escape events and 2 entries of CO into the protein matrix were observed via six different ligand migration pathways, designated

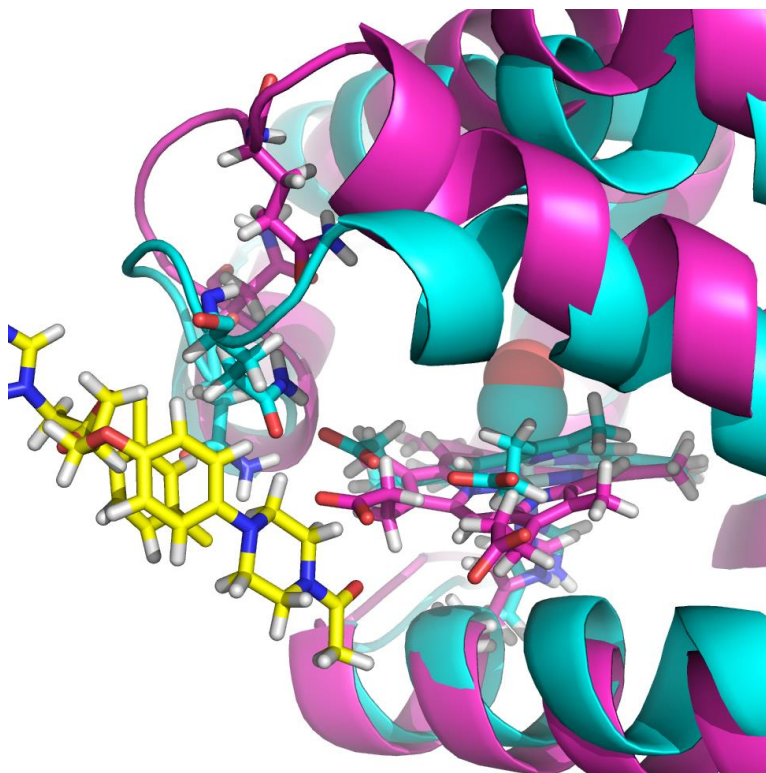


Figure 5.10 Alternate view of the overlay of MD snapshots of CO-FHP with ketoconazole bound (cyan) with the drug-free CO-FHP (magenta) after 20 ns of simulation. For both proteins residues 1 – 130 are shown as cartoon representations and Asn44 and Gln48 are shown as sticks. The ketoconazole molecule is shown with yellow carbons.

A through F. Details about these pathways are found in Table 5.2 and the two pathways with the most escape events are shown in Figure 5.9.

Pathway A leads from the distal heme cavity to the bulk solvent and passes between residues Leu103 and Tyr126 on the G and H helices, respectively. These residues are located towards the “back” of the heme binding pocket, on the side of the heme opposite the propionate groups, and are visible in Figure 5.10. Pathway A is by far the most prominent with 13 of 21 escape events and a single entry occurring this way. Pathway B passes between the A-helix and GH-loop in the vicinity of Thr13, Val16, Leu100, and Ile118 with one escape event and one entry through this path. Pathway C is between the AB-loop and E-helix with two escape events. Pathway D is close to the EF-loop and passes

Table 5.2 Pathways of CO escape observed during 30 ns MD simulation of CO:FHP using locally enhanced sampling with 20 enhanced ligands.

Pathway Designation	Critical Residues	CO Escapes from Globin Domain	CO Entries into Globin Domain	Escape Fraction	Entry Fraction
A	L103, Y126	13	1	0.619	0.5
B	T13, V16, L110, I118	1	1	0.048	0.5
C	G21, Q54	2	0	0.095	0
D	A63, V77, R59	1	0	0.048	0
E	N44, Q48, I371, V395, P398	3	0	0.143	0
F	M1, M75, L78, L129	1	0	0.048	0

between Ala63 and Val77 close to Arg59 with one escape event. Pathway E passes between the heme propionate groups and CD loop and is closest to the canonical “distal His gate”

escape pathway expected for proteins such as hemoglobin. (140) The critical residues for this pathway include Asn44 and Arg48 and the heme-6-propionate group is also nearby. Three escapes are seen to occur this way, with escaped ligands temporarily residing in a hydrophobic area between the globin and flavin-binding domains adjacent to Ile371, Val395, and Pro398. The final pathway F is close to the N-terminus, adjacent to the H-helix and EF-loop with only one escape event.

Due to the high local concentration of enhanced CO ligands in the water box, we also observe the entry of three CO molecules into the flavin-binding domain of FHP. One CO molecule enters the protein matrix from the solvent near Lys224 and Ile169, while the other two escape from the heme binding pocket via pathway E; all three diffuse to a hydrophobic pocket bordered by Phe396, Pro280, Phe259, Ser209, Gly188, Met284, Tyr190, Glu394, Cys368. This location is near the binding site for the flavin group of FADH which was shown previously (49)

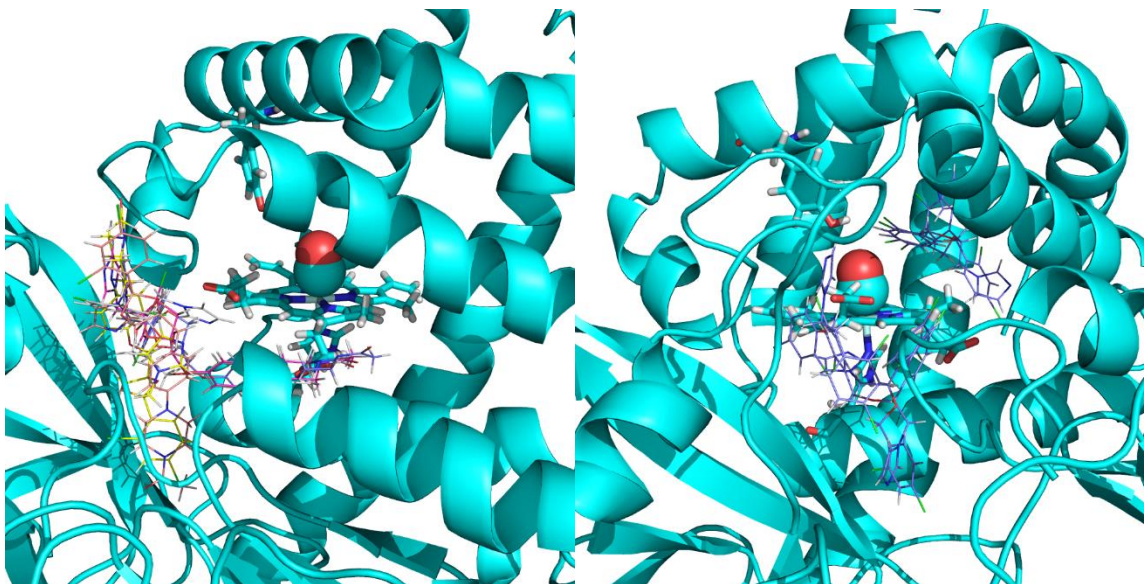


Figure 5.11 Binding locations of ketoconazole (left) and miconazole (right) to CO-FHP predicted by Autodock Vina. Heme, CO, Tyr29 and His85 are shown as licorice and the five drug conformations with highest binding affinity are shown as thin lines.

5.2.3.2 Binding sites of ketoconazole and miconazole in FHP

Autodock Vina (*141*) was used to predict the binding location of the drugs ketoconazole and miconazole to CO-FHP. Predicted locations for binding of ketoconazole and miconazole are shown in Figure 5.11. Ketoconazole is predicted to bind in the hydrophobic cleft between the globin and flavin-binding domains, either directly alongside the heme propionate groups or reaching deeper into the center of the flavin-binding domain. In the former conformation, ketoconazole is in close proximity with the hydrophobic residues Leu88, Ile371, and Val395. The oxygen of the terminal acetyl group of ketoconazole is well-positioned to form hydrogen bonds with Arg59 and Arg375 while the dichlorophenyl group appears to form cation- π interactions with Lys84 and Arg206. This position is adjacent to the binding site of ketoconazole resolved for ligand-free FHP, in which the drug was located partially inside the distal heme pocket with its imidazole group directly coordinating the heme iron. (*49*) After 20 ns of MD simulation with the

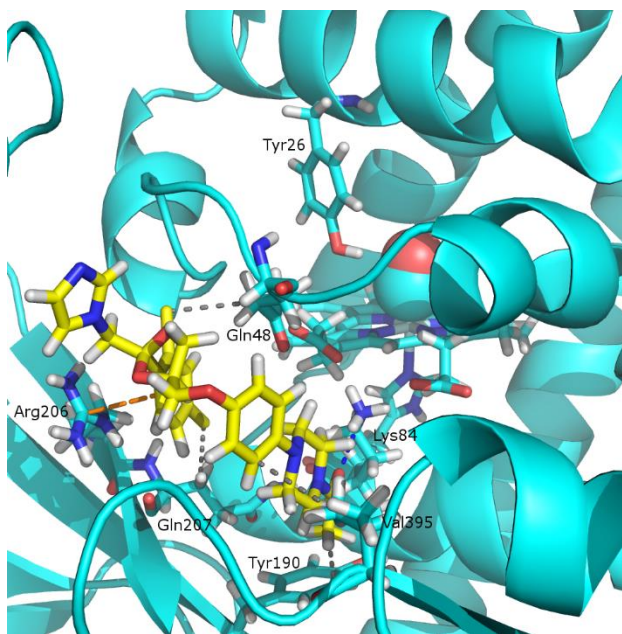


Figure 5.12 A view of the heme binding pocket of CO-FHP with ketoconazole bound after 20 ns of MD simulation. Hydrophobic interactions are shown as gray lines, cation- π interactions are shown as orange lines, and hydrogen bonds are shown as blue lines.

initial position predicted by Autodock Vina, the drug repositions within the interdomain cleft, maintaining its cation- π interaction with Arg206 while forming a hydrogen bond between the oxygen of the terminal acetyl group and Lys84. These interactions are shown in Figure 5.12. In addition, after approximately 15 ns of simulation the CD loop of the globin domain (residues 40 – 55) is seen to move towards the ketoconazole molecule (Figure 5.14). The E helix repositions slightly due to this movement of the CD loop. These residues are directly adjacent to the heme binding pocket and are in close contact with the drug molecule forming a dry hydrophobic interface; however, a layer of water is present between the drug and the flavin-binding domain, causing the bound ketoconazole to have a somewhat aqueous environment overall.

In the case of miconazole, the highest affinity binding sites are located directly within the heme binding pocket in direct contact with the bound CO ligand with lower-affinity sites close to the heme-6-propionate group and the predicted location for

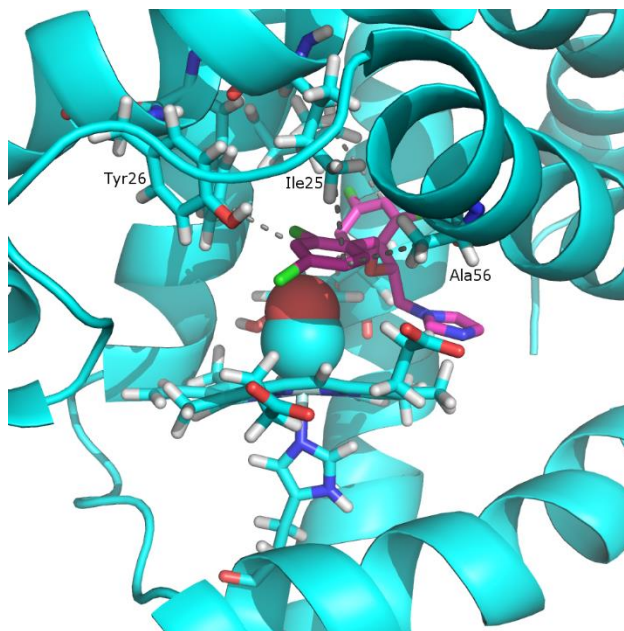


Figure 5.13 A view of the heme binding pocket of CO-FHP with miconazole bound after 20 ns of MD simulation. Hydrophobic interactions are shown as gray lines.

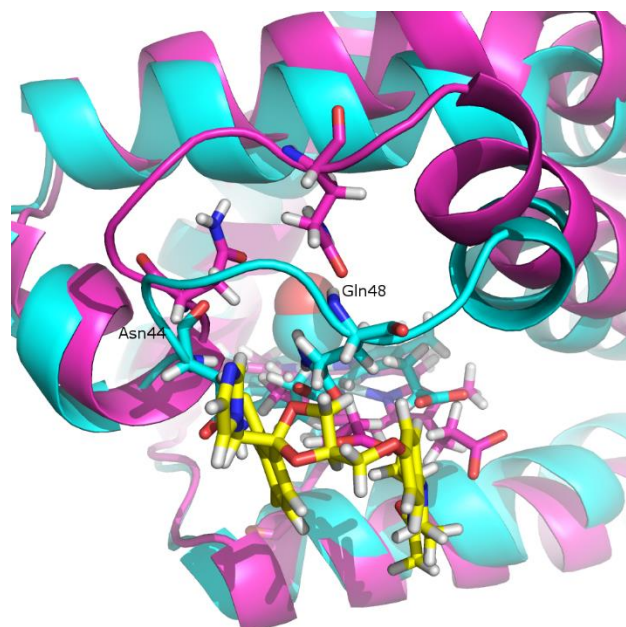


Figure 5.14 Overlay of MD snapshots of CO-FHP with ketoconazole bound (cyan) with the drug-free CO-FHP (magenta) after 20 ns of simulation. For both proteins residues 1 – 130 are shown as cartoon representations and Asn44 and Gln48 are shown as sticks. The ketoconazole molecule is shown with yellow carbons.

ketoconazole binding (Figure 5.11). The highest-affinity binding site predicted by Autodock Vina places miconazole in contact with the hydrophobic cluster which includes Ala56, Leu102, Trp122, and Tyr126. After 20 ns of MD simulation, miconazole repositions slightly to form hydrophobic contacts with Ile25, Phe28, Ala56, Leu102, and Tyr126 as shown in Figure 5.13 with an alternate view in Figure 5.15. Over the course of the simulation the imidazole group of the drug moves from its initial position to being just above the plane of the heme group on the distal side, in close proximity to the heme iron ($\sim 7 \text{ \AA}$). No reorganization of the CD loop is observed in the MD simulation of miconazole-bound CO-FHP, and the environment of the drug molecule is almost entirely hydrophobic.

5.3 Discussion

5.3.1 The effect of azole drugs on ligand migration pathways in FHP

In our LES-enabled simulation of CO:FHP, pathway A passes between residues Leu103 and Tyr126 allowing direct movement of ligands between the distal heme pocket and bulk solvent. 13 out of 21 (62%) CO escape events occur via this pathway. No large scale changes in tertiary structure or major fluctuations of critical residues are associated with the migration of CO molecules into or out of the protein matrix. The positions of the critical residues in pathway A, Leu103 and Tyr126, do not change significantly during the LES-enabled simulation. The position of Leu103 is stable due to it being part of a hydrophobic cluster formed from neighboring residues which include Leu102, Ile106, Trp122, and Ala123. This hydrophobic cluster has been previously identified in the crystal structure of FHP (*142*). The position of the side chain of Tyr126 is stabilized by a hydrogen bond to the backbone oxygen of Tyr95, aside from a brief rotation about the C-O bond to

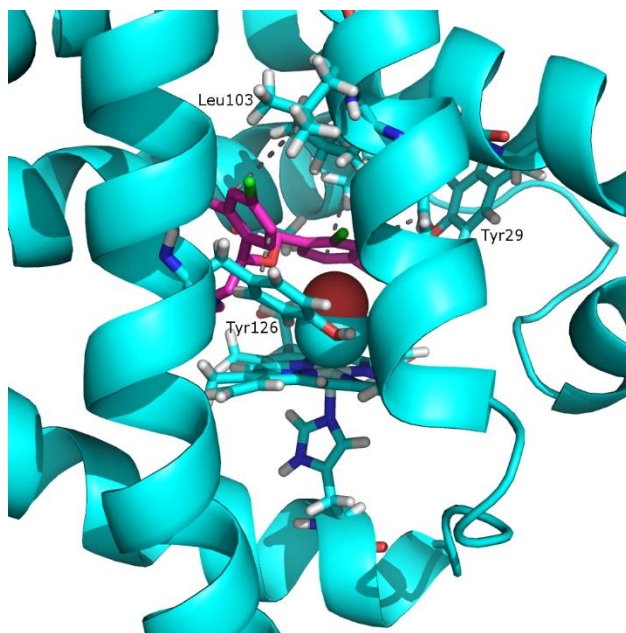


Figure 5.15 An alternate view of the heme binding pocket of CO-FHP with miconazole bound after 20 ns of MD simulation. Hydrophobic interactions are shown as gray lines.

allow the hydroxyl group of tyrosine to briefly hydrogen bond with water molecules in the heme binding pocket. Therefore, the passage of ligand molecules through pathway A does not seem to be dependent on the fluctuations of a gating residue as in the typical distal His gate mechanism in human hemoglobin (**96**), but instead is likely dependent on large-scale dynamic fluctuations of the protein structure combined with subtle movements in the position of the side chains of Leu103 and Tyr126 which lower the energetic barrier for ligand escape. For example, though the overall position of the side chain of Tyr126 is stable, the phenol ring is able to rotate around the C_β-C_γ bond to a great degree, with a range of C_α-C_β-C_γ-C_δ dihedral angles of over 70 degrees.

Pathway E, passing between the CD loop (residues 40 – 55) and heme propionate groups, is the second most common escape pathway and is involved in 3 out of 21 (14%) CO escapes. The geometry of this region is significantly altered compared to more well-known globins such as myoglobin and hemoglobin, however this pathway bears some resemblance to a common pathway in hemoglobin for ligand migration between the bulk solvent and heme binding pocket which passes between the E-helix/CD-loop and heme propionate groups which has been identified in experimental (**16**) and computational studies. (**140**)

Though other pathways for ligand escape are observed, they are collectively responsible for only 4 out of 21 (19%) of CO dissociation events. Given that LES ligands experience significantly lower energetic barriers for migration in the protein matrix than would be expected in reality, it is questionable whether these minor pathways are significantly represented *in vivo*.

Our Autodock Vina results and subsequent MD simulations of azole drugs bound to CO-FHP show that one of the dichlorophenyl groups of miconazole associates with the hydrophobic cluster adjacent to pathway A which includes critical residues Leu102 and Leu103 as shown in Figure 5.13 and Figure 5.15. This positioning obstructs pathway A and reduces the likelihood that a ligand molecule would be able to migrate between the heme binding pocket and bulk solvent while also occupying a large amount of volume within the heme binding pocket. Binding of ketoconazole in the interdomain cleft induces a reorganization of CD loop residues 40 – 55 as shown in Figure 5.14. The driving force for CD loop reorganization is most likely hydrophobic, due to the hydrophobicity of the ketoconazole molecule. CD loop reorganization leads to obstruction of pathway E both due to a shift in the peptide backbone of the loop and the reorientation of residue side chains. For example, the backbone α -carbons of critical residues Asn44 and Gln48 shift towards the ketoconazole molecule by circa 2.5 and 5 Å, respectively, while their sidechains reorient to directly obstruct the migration pathway as shown in Figure 5.14.

5.3.2 The impact of azole drugs on thermodynamic and kinetic parameters

Different thermodynamic and kinetic parameters (in terms of ΔV , ΔH , Φ_{bm} , and rebinding rate constants) were resolved for drug-free, ketoconazole-bound and miconazole-bound fHbs as shown in Table 5.1 and Table 5.3. This makes sense given the different binding locations and interactions we predict for the two drugs binding to FHP based on our Autodock Vina and MD results. The parameters we resolve using PAC (ΔV and ΔH) can be further broken down into several contributions according to the following equations:

$$\Delta H = H_{\text{Fe-CO}}^{\circ} + \Delta H_{\text{struc}} + \Delta H_{\text{el}} \quad (5.3)$$

$$\Delta V = V_{\text{CO}}^{\circ} + \Delta V_{\text{struc}} + \Delta V_{\text{el}} \quad (5.4)$$

In Equation 5.3, $H_{\text{Fe-CO}}^{\circ}$ is equal to the bond dissociation enthalpy of the Fe-CO bond, which is approximately 26 kcal mol⁻¹ according to DFT calculations of the myoglobin heme active center (67). ΔH_{struc} represents energetic changes in the protein structure including breakage/formation of hydrogen bonds or other dipole interactions. ΔH_{el} includes enthalpy changes resulting from electrostriction which arises from the reorganization of solvent molecules due to exposure or removal of charged species from the bulk solvent. In Equation 5.4, ΔV_{struc} incorporates changes in the overall volume of the protein structure and any volume changes occurring due to binding/dissociation of non-gaseous ligand molecules. V_{CO}° is the partial molar volume of the CO molecule (37.3 ± 0.5 mL mol⁻¹) (70)

Table 5.3 Rate constants for “slow” geminate and bimolecular rebinding of CO to flavohemoglobins from *Ralstonia eutropha* (FHP) and *Staphylococcus aureus* (HMP_{Sa}) in the presence and absence of ketoconazole and miconazole. Error values are standard deviations for multiple runs. for All data listed were determined at 20 °C.

Protein	Drug Identity	Drug Conc. 20 °C (μM)	Percent Drug-Bound	k _{gem} (μs ⁻¹)	k ₁	k ₂	k ₃
					(μM s ⁻¹)		
CO-FHP	None	0	0	N/A	2.00 ± 0.07	0.18 ± 0.02	0.06 ± 0.009
	Ketoconazole	14	49		3.43 ± 0.45	0.49 ± 0.13	0.12 ± 0.02
	Miconazole	409	99		2.00 ± 0.10	0.26 ± 0.01	0.05 ± 0.001
CO-HMP _{Sa}	None	0	0	0.11 ± 0.002	2.72 ± 0.05	0.93 ± 0.01	N/A
	Ketoconazole	14	45	0.14 ± 0.02	6.54 ± 0.96	1.5 ± 0.05	N/A
	Miconazole	409	99	0.11 ± 0.004	1.24 ± 0.03	0.31 ± 0.01	N/A

which leaves the protein matrix after photo-dissociation, and ΔV_{el} represents the same electrostriction process as above.

For photo-dissociation of CO from drug-free CO-FHP, the ΔH we measure (26.2 ± 7.0 kcal mol⁻¹) corresponds well with the predicted value of H°_{Fe-CO} (26 kcal mol⁻¹) indicating that the observed enthalpy change is almost entirely due to photolysis of the Fe-CO bond. There may be small contributions from solvation of the CO molecule or other processes that are within the error of the measurement. We do not see any enthalpic evidence for hydrogen bonds between the bound ligand, a bridging water molecule, and TyrB10 as predicted previously for *E. coli* fHb based on QM/MM computations (137) as we would expect an additional endothermic contribution due to breakage of these bonds. These data are consistent with our MD simulation of CO-FHP, where we also do not observe the formation of a bridged hydrogen bond between TyrB10 and the bound CO. Therefore, this interaction likely does not occur in FHP.

The observed $\Delta V = 25.0 \pm 1.5$ mL mol⁻¹ can be explained by the diffusion of the CO molecule into the bulk solvent which provides a positive contribution of ~ 37 mL mol⁻¹. There is also a negative contribution of ~ -12 kcal mol⁻¹ which is most likely due to a water molecule ($V^\circ = 18$ mL mol⁻¹) entering the heme binding pocket subsequent to CO photo-dissociation in $\sim 66\%$ of FHP molecules. Water entry into the heme pocket on fast timescales after ligand photolysis has been observed previously in sperm whale myoglobin (143) and is plausible given the large volume of the heme pocket in FHP (~ 2000 Å³). (49)

The binding of ketoconazole to FHP results in a much more exothermic enthalpy for CO photo-dissociation with $\Delta H_{bound} \sim -42.3$ kcal mol⁻¹. Assuming that H°_{Fe-CO} does not

change, this means that $\Delta H_{\text{struc}} + \Delta H_{\text{el}} = -68.5 \text{ kcal mol}^{-1}$ according to Equation 5.3. It is known from the crystal structures ofazole drugs bound to FHP that the imidazole group is able to coordinate the heme iron on the distal side in the absence of a bound ligand and our computational results predict a location for ketoconazole binding close to the heme binding pocket. Molecular dynamics simulations of a simple model system consisting of a hydrophobic ligand binding to a hydrophobic cavity have predicted a negative enthalpy change for this process due to enthalpically favorable interactions between water molecules displaced to the bulk solvent (*144*). In addition, coordination of the heme iron by imidazole is also associated with a negative enthalpy change. (*145*) Therefore, we attribute the additional exothermic enthalpy of $-68.5 \text{ kcal mol}^{-1}$ observed for CO photo-dissociation from FHP in the presence of ketoconazole to a combination of contributions due to i) migration of the drug into the heme binding pocket (and concurrent breakage of π -cation and hydrogen bonding interactions between ketoconazole and the protein matrix), ii) displacement of water molecules from the heme binding pocket into the bulk solvent and iii) subsequent coordination of the imidazole nitrogen of ketoconazole to the heme iron. Each of these processes yields a favorable negative enthalpy change and our PAC data show that they occur within the lower limit of resolution of our instrumentation, which is $\sim 50 \text{ ns}$. In this context, the decrease in ΔV observed for CO photo-dissociation in the presence of ketoconazole compared to the drug-free protein ($\Delta\Delta V = -22.4 \text{ mL mol}^{-1}$) can be explained by the movement of the drug from partially exposed on the protein surface into the heme binding pocket (a negative contribution) and by displacement of water molecules from the heme binding pocket into the bulk solvent (a smaller, positive contribution). Our data are not consistent with dissociation of ketoconazole from the

protein upon CO photo-dissociation as we would expect to observe a much larger ΔV ; the van der Waals volume of ketoconazole alone is 293 mL mol^{-1} , and there would likely be additional contributions to ΔV from solvation of this bulky hydrophobic molecule.

ΔH for CO photo-dissociation in the presence of miconazole is also more exothermic than in the absence of the drug ($\Delta\Delta H = -43.6 \text{ kcal mol}^{-1}$), with $\Delta H_{\text{struc}} + \Delta H_{\text{el}} = -43.4 \pm 7.0 \text{ kcal mol}^{-1}$. The binding location we have predicted for miconazole based on our computational results is directly within the heme binding pocket, therefore unlike ketoconazole we do not expect to see an exothermic contribution from migration of the drug into the heme binding pocket and displacement of water molecules into the bulk solvent. The value of $\Delta H_{\text{struc}} + \Delta H_{\text{el}}$ we observe for CO photo-dissociation in the presence of miconazole ($-43.4 \pm 7.0 \text{ kcal mol}^{-1}$) is therefore largely attributable to the formation of a coordination bond between the heme iron and the imidazole group of miconazole. There is likely also a smaller negative contribution to ΔH from electrostriction due to reorganization of water molecules within the heme binding pocket around the polar dichlorophenyl groups of miconazole as it repositions to bind the heme iron.

The difference between ΔV values observed for CO photo-dissociation from FHP in the presence and absence of miconazole ($\Delta\Delta V = -4.6 \text{ mL mol}^{-1}$) also supports the idea that the position of the drug does not change greatly and that solvent molecules are not greatly disturbed. The small difference of -4.6 mL mol^{-1} we observe is most likely due to electrostriction of water molecules within the heme binding pocket due to the movement of miconazole. Again, our data do not support the idea that the drug dissociates from the

protein, as we would expect a larger ΔV owing to the van der Waals volume of miconazole, which is 305 mL mol^{-1} .

If we assume that the ΔH for the formation of the coordination bond between the imidazole group of theazole drug and the heme iron is similar for miconazole and ketoconazole, then we can estimate ΔH for migration of the ketoconazole molecule into the heme pocket from the difference between $\Delta H_{\text{struc}} + \Delta H_{\text{el}}$ for photo-dissociation of CO from FHP in the presence of each drug. We estimate $\Delta H = -25.1 \text{ kcal mol}^{-1}$ for this process, which includes ketoconazole dissociation from its initial position in the intra-domain cleft, migration into the heme binding pocket, and expulsion of water molecules.

In the case of HMP_{Sa}, $\Delta H = 34.7 \pm 8.0 \text{ kcal mol}^{-1}$ is observed for CO photo-dissociation in the absence ofazole drugs. This value is higher than that observed for the same process in FHP, in which ΔH was attributed primarily to breakage of the Fe-CO bond. If we assume the value of $H^{\circ}_{\text{Fe-CO}}$ is unchanged between the two proteins, it follows that there is an additional endothermic contribution equal to the difference in ΔH which is $8.7 \text{ kcal mol}^{-1}$. This value is similar to that determined for the energy of the strong hydrogen bond between the distal His and bound O₂ in myoglobin based on density functional theory studies. (17) This suggests that a bridged hydrogen bond between TyrB10, a water molecule, and the bound ligand predicted based on QM/MM studies of *E. coli* fHb (137) can be found in CO-HMP_{Sa} and that this bond is broken subsequent to CO photolysis. ΔV for CO photo-dissociation from HMP_{Sa} ($28.6 \pm 1.7 \text{ mL mol}^{-1}$) is only slightly larger than for FHP, indicating similar structural changes. The migration of CO from the heme pocket

provides a contribution of -37 mL mol^{-1} which is compensated by entry of a water molecule in $\sim 47\%$ of HMP_{Sa} molecules.

In the presence of ketoconazole CO photo-dissociation from HMP_{Sa} becomes more exothermic, the same phenomenon as for FHP; however ΔH is even more exothermic with $\Delta\Delta H = -10.3 \text{ kcal mol}^{-1}$ if we compare ΔH_{bound} for the two proteins. We predict that the processes which contribute to ΔH (ketoconazole migration into the heme binding pocket, expulsion of water molecules into the bulk solvent, and imidazole group coordination of the heme iron) are similar between FHP and HMP_{Sa}, but the differing geometry of the heme binding pocket results in a more exothermic enthalpy change for the first two processes in HMP_{Sa}, possibly due to the expulsion of additional water molecules. The more negative ΔV for CO photo-dissociation from HMP_{Sa} in the presence of ketoconazole as compared to the drug-free protein ($\Delta\Delta V = -38.9 \text{ kcal mol}^{-1}$) is consistent with this concept. The binding position of ketoconazole within the heme binding pocket of HMP_{Sa} may be deeper than in FHP, resulting in the expulsion of additional water molecules and the observation of a more exothermic enthalpy change and more negative volume change than in the case of CO photo-dissociation from ketoconazole-bound FHP.

CO photo-dissociation from miconazole-bound HMP_{Sa} results in a relatively large and exothermic $\Delta H = -83.9 \pm 5.4 \text{ kcal mol}^{-1}$. Accounting for $H^{\circ}_{\text{Fe-CO}}$ and an estimated $\Delta H = 8.7 \text{ kcal mol}^{-1}$ for the bridged hydrogen bond between TyrB10 and the bound CO, we estimate $\Delta H_{\text{struc}} + \Delta H_{\text{el}} = -110 \text{ kcal mol}^{-1}$. This value is more exothermic than that determined for CO photo-dissociation from miconazole-bound FHP ($-43.4 \pm 7.0 \text{ kcal mol}^{-1}$) signifying different structural changes occurring within the protein after CO photolysis.

Previously, we suggested that the more endothermic ΔH observed for CO photo-dissociation from miconazole-bound FHP as compared to ketoconazole-bound FHP was due to miconazole not migrating into the heme binding pocket and displacing some of the water molecules within as ketoconazole does, which results in an exothermic contribution to ΔH . In this case, the more exothermic enthalpy for CO photo-dissociation from miconazole-bound HMP_{Sa} may be due to the opposite phenomenon, i.e. the miconazole molecule does not bind directly within the heme binding pocket in CO-HMP_{Sa} as in CO-FHP. Instead the drug binds to the protein surface near the heme binding pocket and migrates into the protein subsequent to CO photo-dissociation similarly to ketoconazole. The more exothermic ΔH observed for CO photo-dissociation from miconazole-bound CO-HMP_{Sa} would suggest that the drug binds more deeply in the heme binding pocket than ketoconazole causing the displacement of a larger number of water molecules into the bulk solvent. This idea is supported by the previously published crystal structures of ketoconazole and miconazole-bound FHP in which both drugs are coordinated to the heme iron via their imidazole groups. Ketoconazole only partially enters the heme binding pocket, whereas miconazole enters it entirely. In addition, the binding locations for miconazole in FHP predicted by Autodock Vina (Figure 5.11) include lower affinity sites outside the heme binding pocket, close to the predicted sites for ketoconazole binding in FHP. In HMP_{Sa} miconazole may preferentially occupy this site instead of residing within the heme binding pocket as predicted for miconazole-bound FHP.

5.3.3 Mechanism of inhibition of fHbs by azole drugs

The binding sites we have predicted for ketoconazole and miconazole and their impact on ligand migration pathways in ligated FHP are relevant to the NOD activity

of the protein. Based on the proposed mechanisms for the NOD activity of fHbs (7), and the observed obstruction by ketoconazole and miconazole of specific cavities in FHP which our simulations show to be in/near ligand and electron migration pathways, we can predict the mechanism by which binding of each azole drug inhibits NOD activity in fHbs. In the case of ketoconazole, inhibition appears to be due to the repositioning of CD-loop residues 40 – 55 caused by the drug binding in the hydrophobic cleft between the heme globin and flavin-binding domain which obstructs ligand migration via pathway E. It is also likely due to an alteration of the environment in the vicinity of the heme propionate groups which have been predicted to participate in electron transfer between the heme group and bound electron-donating cofactors via structural water molecules based on computational studies in FHP (136) and *E. coli* fHb (137). The predicted locations of these water molecules are occupied by CD-loop residues and the ketoconazole molecule itself in our MD simulation. For miconazole, inhibition of NOD activity is probably due to binding of the drug within the heme binding pocket where it sterically blocks pathway A. In the case of HMP_{sa}, the binding of miconazole adjacent to the heme propionate groups may interfere with electron transfer in a similar fashion as predicted for ketoconazole. Overall, these effects of azole drug binding restrict NO/O₂ molecules from accessing the heme active site and/or hinder electron transfer from bound NADPH and FADH preventing the reduction of the heme iron which is necessary to the NOD catalytic cycle.

It is important to consider whether these putative mechanisms could be relevant for HMP_{sa} and other related fHbs, given that the structures of most fHbs are not available. A sequence alignment of FHP, HMP_{sa}, and the 49 fHbs with the highest sequence homology to FHP available in the UniProt database shows that the critical residues for the two most

popular ligand migration pathways observed in our LES-enabled MD simulation, A and E, are conserved between virtually all of these proteins. This includes Leu103 and Tyr126 for pathway A and Asn44 and Gln48 for pathway E; in one instance Gln48 is mutated to lysine. In addition, the residues which the azole drugs most closely associate with in our MD simulations of drug-bound CO-FHP are also well-conserved between all proteins; Arg206 which forms a cation- π interaction with ketoconazole and Lys84 which forms a hydrogen bond with ketoconazole are entirely conserved. The hydrophobic cluster that miconazole associates with is well conserved, with the most important residues Phe28, Ala56, Leu102, Leu103 and Trp122 being entirely conserved. Therefore, we find it probable that similar mechanisms of inhibition are at play in both FHP and HMP_{Sa} and potentially in many more fHbs. Even though we have suggested that miconazole binds within the heme binding pocket of CO-FHP, but not of CO-HMP_{Sa}, the putative mechanisms of inhibition of NOD activity remain the same in both cases.

5.4 Conclusion

Our results indicate that binding of the azole drugs ketoconazole and miconazole to fHbs from *C. necator* and *S. aureus* results in significant changes in thermodynamic and kinetic parameters associated with interaction of fHbs with diatomic gaseous ligands as determined by PAC and TA. These changes are attributable to translocation of bound azole drugs in the vicinity of the distal heme pocket heme active site with slightly different mechanisms depending on the particular fHb and azole drug combination. The protein structure and ligand/electron migration pathways are also impacted by drug binding as predicted by cMD simulations.

Further development of antibiotic compounds designed to inhibit the NOD activity of fHbs would likely benefit from a focus on obstruction or alteration of electron and ligand migration pathways in these proteins. Specifically, obstruction of pathways A and E or disruption of the electron transfer pathway which involves the heme propionate groups and adjacent structural water molecules.

6 STRUCTURES OF THE KINETICALLY TRAPPED I-MOTIF DNA INTERMEDIATES

6.1 Introduction

A wide variety of DNA structural motifs have been discovered in recent years. The well-known G-quadruplex tertiary structural motif forms from guanosine-rich (G-rich) single-stranded DNA such as that occurring in the G-rich strand of the human telomere (*146*) as well as in the promoter regions of some oncogenes (*147*). G-quadruplexes are strongly stabilized by the presence of monovalent cations and have been theorized to have several roles *in vivo* including regulation of transcription. (*146*) More recently, it has been discovered that cytosine-rich (C-rich) DNA can form a structural motif which is stabilized by intercalated base pairs between positively-charged protonated cytosines and neutral, unprotonated cytosines (Figure 6.1). This structure can form intermolecularly from

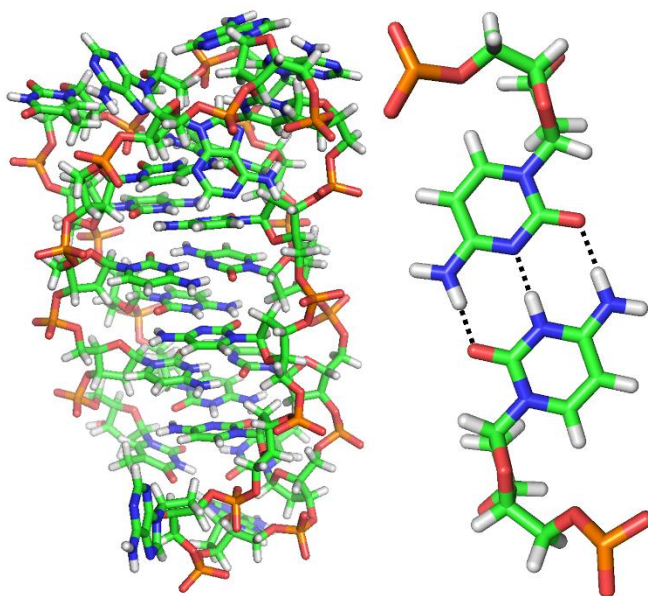


Figure 6.1 (Right) Solution structure DNA i-motif with the sequence 5' d(CCCTA2CCCTA2CCCTA2CCCT)-3' determined by NMR (PDB: 1ELN) (*161*).

(Left) A single hemiprotonated cytosine⁺:cytosine base pair from the i-motif solution structure. Hydrogen bonds are shown as dotted lines.

multiple C-rich strands, forming a tetraplex, or intramolecularly within a single DNA oligomer. This structure is known as the DNA intercalated motif, or i-motif.

The presence of the i-motif has been theorized to occur in the C-rich strand of the human telomere (*148*) which is complementary to the sequence which forms the G-quadruplex, as well as in the promoter regions of oncogenes including c-MYC (*33*). Formation of the i-motif *in vitro* is strongly dependent on pH due to the protonation of cytosine which is necessary to form the characteristic intercalated, hemiprotonated base pairs (*149*). It has been predicted that molecular crowding effects could result in the formation of the i-motif *in vivo* even at the neutral to slightly basic pH which is typical of the cell interior (*32*). Characterization of the kinetics and thermodynamics of i-motif folding is therefore essential to understanding the role of the i-motif in diverse cellular processes.

In this study, the pH-dependent formation of the intramolecular i-motif was probed using photoacoustic calorimetry and circular dichroism spectroscopy. The iDNA sequence utilized was a 21-mer whose sequence was derived from that of the C-rich strand of the human telomere (5-[CCCTAA]₃CCC-3'). In order to monitor the formation of the DNA i-motif using PAC, we must be able to phototrigгер the structural transition. A 2-nitrobenzaldehyde (2-NBA) pH-jump technique was used for this purpose. Photolysis of 2-NBA in the near UV (355 nm in this case) results in the formation of 2-nitrosobenzoate and the release of a proton on very fast timescales (*150*). Using this technique, the pH of solution within the illuminated volume can be decreased very quickly by a fast laser pulse

potentially triggering pH-dependent processes. The combination of PAC and a pH-jump has been used previously to study the pH-dependent unfolding of apomyoglobin (151).

6.2 Results

6.2.1 Parameters of the 2-nitrobenzaldehyde pH-jump

In order to analyze data recovered using fast time-resolved techniques such as PAC, it is necessary to know the pH which results in solution from the photolysis of 2-NBA. The molar attenuation coefficients of pyranine and bromocresol green (BCG) are shown in Figure 6.2. It was determined that pyranine could be used to characterize photolysis of 2-NBA between pH values of 5 – 7, while BCG was effective from pH 3 – 7. Pyranine is more sensitive to small decreases in pH ($\Delta\text{pH} < -2$) while BCG is more sensitive to larger changes ($\Delta\text{pH} > -2$). Transient absorption data from the photolysis of both dye compounds was used to construct Figure 6.3, which shows solution pH within the illuminated volume of the pyranine/2-NBA and BCG/2-NBA after photolysis of 2-NBA at a concentration of 1.0 mM as a function of the cross-sectional power of the laser pulse.

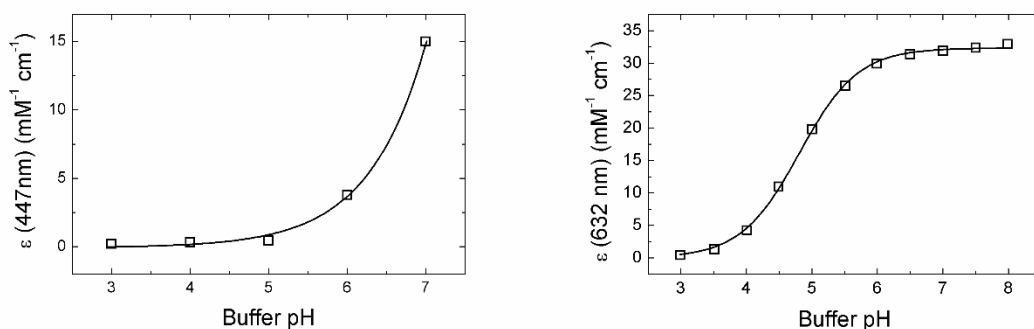


Figure 6.2 (Left) Molar attenuation coefficients as a function of pH for 50 μM pyranine in 50 mM sodium phosphate buffer. Logistic fit of the data points is shown as a solid black line.

(Right) Molar attenuation coefficients as a function of pH for 50 μM bromocresol green in 10 mM sodium phosphate buffer. Logistic fit of the data points is shown as a solid black line.

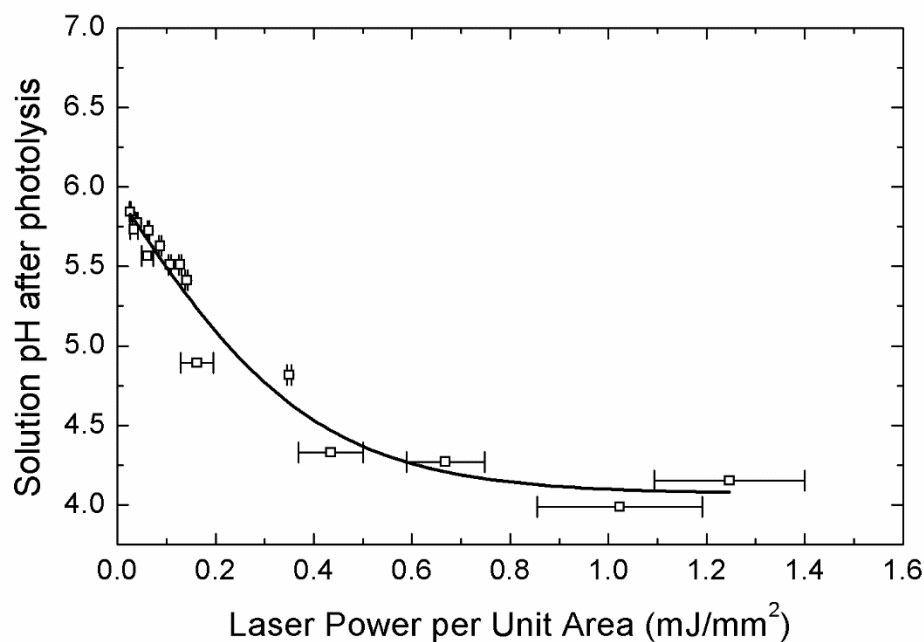


Figure 6.3 pH of the illuminated volume after photolysis of 2-NBA as a function of the cross-sectional power of the laser pulse. Error bars indicate the standard deviation of the laser power determined from the average of 100 laser pulses.

6.2.2 Folding equilibrium determined by circular dichroism

CD spectra were determined for iDNA at thermodynamic equilibrium at a range of pH values (Figure 6.4). It was observed that decreasing pH resulted in an increase of the signal at 287 nm and concomitant decrease of the CD signal at 272 nm. The isosbestic points observed at 245 and 276 nm are suggestive a two-state folding mechanism for the i-motif. The transition of the i-motif as a function of pH with a transition occurring at pH ~ 6 is in agreement with CD spectra previously determined for iDNA (152).

6.2.3 Enthalpy and volume changes determined by PAC

To characterize dynamics and energetics of iDNA folding, we have employed PAC to monitor reaction volume and enthalpy change and identify folding intermediates with lifetime on the nanosecond to microsecond timescale. iDNA folding was phototriggered

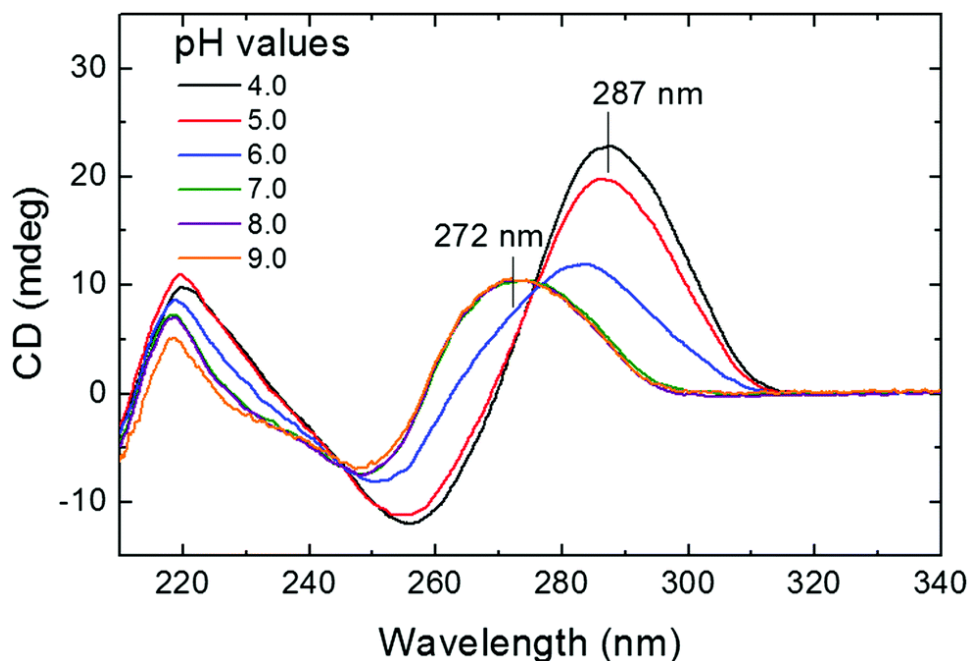


Figure 6.4 Circular dichroism spectra of i-motif DNA (30 μM in deionized water) as a function of the solution pH = 4.0–9.0 at 20 $^{\circ}\text{C}$.

by photolysis of 2-NBA. Under our experimental conditions, the photolysis of 2-NBA leads to a prompt (< 5 ns) pH decrease ($\Delta\text{pH} \sim -2.5$ units). The prompt decrease in pH then initiates folding of the i-motif. The reaction enthalpy and volume change determined for the photolysis of 2-NBA in the absence of iDNA ($\Delta H = -29.2 \pm 6.6$ kcal mol $^{-1}$ and $\Delta V = -5.1 \pm 1.6$ mL mol $^{-1}$) are in agreement with previously published data. (153)

Our PAC traces exhibited a shift between the sample and reference traces (Figure 6.5, Inset), allowing us to resolve two distinct processes, one occurring within 50 ns of the laser pulse and a temperature-dependent process with a time constant of 140 ns at 20 $^{\circ}\text{C}$. The observed enthalpy and volume changes for the fast reaction are $\Delta H = -20.7 \pm 7.0$ kcal mol $^{-1}$ and $\Delta V = 5.3 \pm 1.4$ mL mol $^{-1}$. These values include contributions from the photolysis of 2-NBA, which we can subtract to determine final values for the fast process: $\Delta H_{\text{fast}} = 8.5 \pm 7.0$ kcal mol $^{-1}$ and $\Delta V_{\text{fast}} = 10.4 \pm 1.6$ mL mol $^{-1}$. For the slow process we observe ΔH_{slow}

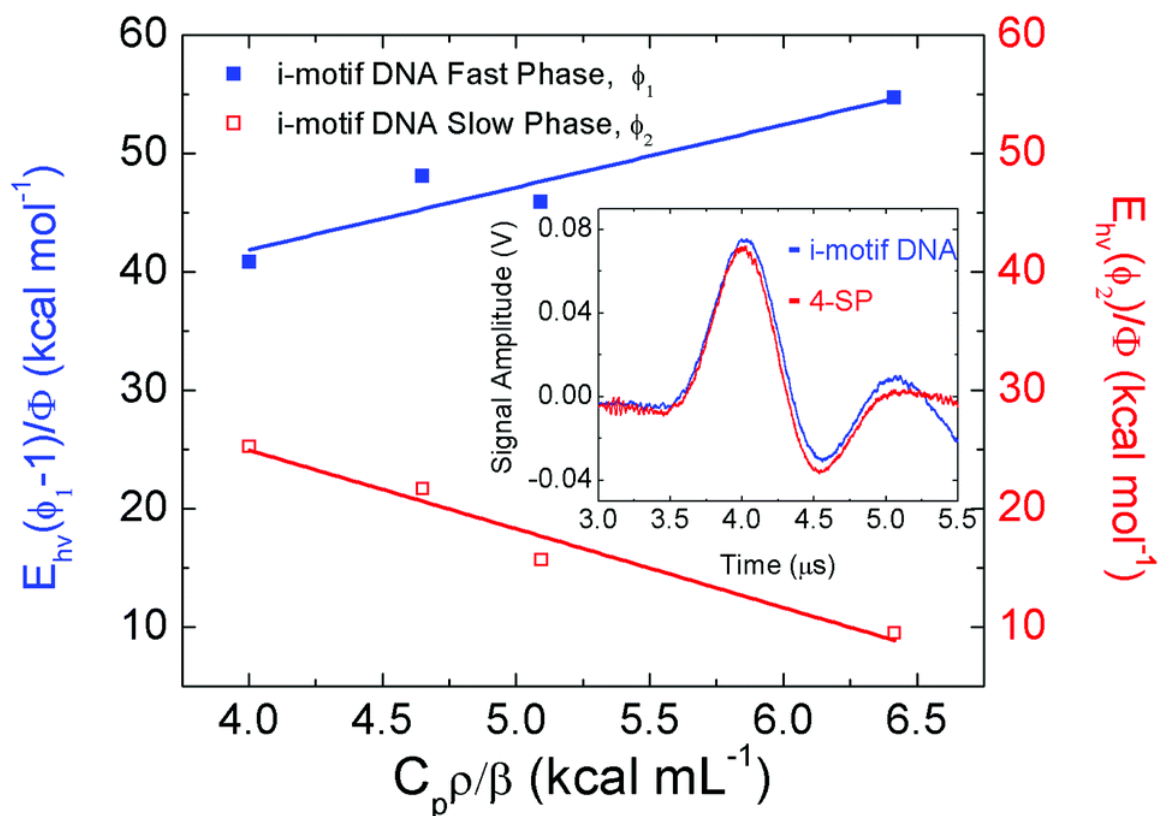


Figure 6.5 Plot of the fast (ϕ_1) and slow (ϕ_2) phases as a function of $C_p\rho/\beta$ in the 16–26 °C temperature range. In the inset, PAC traces for 2-NBA photodissociation in the presence of i-motif DNA sample (blue) and 4SP reference compound (red) at 16 °C.

$= -51.5 \pm 4.8 \text{ kcal mol}^{-1}$ and $\Delta V_{\text{slow}} = -6.6 \pm 0.9 \text{ mL mol}^{-1}$. For the slow process we use an

Arrhenius plot (Figure 6.6) to determine the activation energy (E_a) to be $14.3 \text{ kcal mol}^{-1}$.

6.3 Discussion

Protonation of cytosines within the iDNA oligonucleotide leads to the formation of the intramolecular i-motif structure which has two major forms which differ in chirality: the 5'-endo and 3'-endo structures, with the 5'-endo structure as the major product at

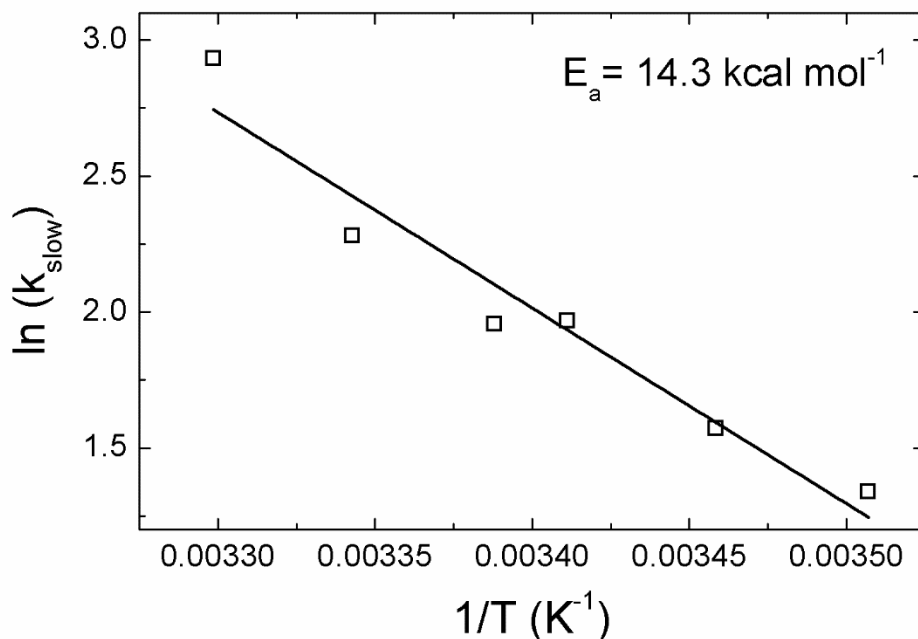


Figure 6.6 Arrhenius plot for the slow kinetic phase determined by PAC.

equilibrium (**154**). Formation of the hemiprotonated cytosine base pairs which stabilize the intramolecular i-motif requires one of the cytosine residues involved to be protonated, which makes the rate of i-motif formation a strongly pH-dependent process. Using 2-NBA, we are able to phototrigger pH jumps of -2.5 units, i.e. from 7 to 4.5. The pK_a of cytosine is 4.58 (**155**) so we expect that dropping the pH to 4.5 causes protonation of ~50% of cytosine residues in the oligonucleotide, ideal for formation of hemiprotonated base pairs. In the sequence 5'-(CCCTAA)₃CCC-3' there are 12 cytosine residues, so we expect six residues to be protonated after the pH jump.

The rate of protonation of the cytosine residues after the pH jump is relevant to determining whether protonation of cytosines in the iDNA oligonucleotide occurs during the fast phase (<50 ns) or slow phase (~140 ns) that we observe in our PAC data. Release of a proton from 2-NBA upon photolysis is very fast (~21 ns) (**150**), while the rate of

protonation of pyridine in solution is on the order of tens of picoseconds (*156*). If we assume the rate of protonation of cytosine is within a few orders of magnitude of that of pyridine, it means that aside from the rate of photolysis of 2-NBA the protonation of cytosine is effectively diffusion-limited. Therefore, we predict that protonation of cytosine residues within the illuminated volume at pH 4.5 occurs within our detection limit of ~50 ns. The enthalpy and volume change we observe for the fast phase ($\Delta H_{\text{fast}} = 8.5 \pm 7.0 \text{ kcal mol}^{-1}$ and $\Delta V_{\text{fast}} = 10.4 \pm 1.6 \text{ mL mol}^{-1}$) are consistent with the expected parameters for protonation of six cytosine residues and subsequent reorganization of the associated solvent shell. We expect an exothermic contribution of $-5.0 \text{ kcal mol}^{-1}$ from the protonation each cytosine (*157*) for a total of $-30 \text{ kcal mol}^{-1}$. For a final observed enthalpy change of $8.5 \pm 7.0 \text{ kcal mol}^{-1}$ there must also be an endothermic contribution of $38.5 \pm 7.0 \text{ kcal mol}^{-1}$. This is likely due to reorganization of water molecules within the solvation shell of the oligonucleotide. Since the random coil iDNA becomes protonated its overall electrical charge is becoming more neutral and water molecules are reorganizing within the proximity of newly protonated cytosine residues, a process with an endothermic enthalpy change and a positive volume change, consistent with our observations.

Nucleation of the i-motif structure requires the formation of at least one hemiprotonated cytosine base pair, an interaction which consists of three hydrogen bonds between one protonated and one unprotonated cytosine residue within an oligonucleotide. Though empirical measurements of the enthalpy of this specific base-pairing interaction are not available, the enthalpy of formation is likely similar to the $-8.0 \text{ kcal mol}^{-1}$ value (*158*) determined for the canonical GC Watson-Crick base pair which also contains three hydrogen bonds. Within the intramolecular i-motif with six protonated cytosines, up to six

cytosine-cytosine base-pairing interactions can be formed for a total maximum contribution of $-48 \text{ kcal mol}^{-1}$ to the observed enthalpy for the folding process. In addition, formation of the i-motif structure results in stacking of the cytosine bases, an interaction with an enthalpy of $-5.0 \text{ kcal mol}^{-1}$ per base pair stack (*159*). Formation of the final i-motif structure results in the formation of 5 base pair stacking interactions for an overall contribution of $-25 \text{ kcal mol}^{-1}$ to the observed enthalpy. According to this model, formation of the fully folded i-motif should provide $\Delta H_{\text{obs}} = -73 \text{ kcal mol}^{-1}$ or $\sim -12 \text{ kcal mol}^{-1}$ per hemiprotonated cytosine base pair. Therefore, the value of $\Delta H_{\text{slow}} = -51.5 \pm 4.8 \text{ kcal mol}^{-1}$ that we determine for the slow process using PAC suggests that within 140 ns of the laser pulse at $20 \text{ }^\circ\text{C}$ we are able to observe the formation of approximately 4.5 hemiprotonated cytosine base pairs and their associated base pair stacking interactions. This is consistent with the nucleation and partial formation of an i-motif structure. The value of ΔH_{slow} we observe is similar to that previously determined by NMR for the intramolecular folding of a similar cytosine-rich strand ($5' \text{-[TCC]}_4 \text{-}3'$) with fewer potential base pairing interactions ($-43 \text{ kcal mol}^{-1}$) (*160*) and for the reverse process of i-motif unfolding using differential scanning calorimetry (66 kcal mol^{-1}) (*159*). The observed volume change ($\Delta V_{\text{slow}} = -6.6 \pm 0.9 \text{ mL mol}^{-1}$) is also logical given that concurrent with the formation of hemiprotonated cytosine base pairs is the collapse of the oligonucleotide into a more compact conformation with a smaller volume as previously observed using small angle X-ray scattering (*149*).

6.4 Conclusion

Our results show that a combined PAC/pH-jump technique utilizing 2-nitrobenzaldehyde can be used to monitor the protonation of the iDNA oligonucleotide, nucleation and partial formation of the i-motif. It has been determined previously that at acidic pH much longer timescales are required for oligonucleotides containing cytosine repeats to reach equilibrium and form the final, lowest-energy i-motif structure (*154*). Therefore, it is likely that the structural enthalpy and volume changes occurring in ~140 ns observed in this study correspond to the formation of i-motif-like intermediates which do not exhibit the final, lowest-energy conformation predicted for this oligonucleotide sequence as determined previously by solution NMR studies (*161*). During the process of i-motif formation the protonated oligonucleotide must sample a large number of conformations before achieving thermodynamic equilibrium.

7 CONCLUSIONS

Herein, we have demonstrated the use of photothermal, transient absorption, computational, and other techniques in the characterization of kinetics and thermodynamics of a variety of processes in biomolecules. In chapters 3, 4, and 5 we present studies on heme proteins from rice, human, *C. necator*, and *S. Aureus* and in chapter 6 we have presented data related to the formation of the intramolecular i-motif in a cytosine-rich DNA oligomer.

In chapter 3 I discussed our data on rHb1 where the use of PAC and TA has allowed us to determine thermodynamic (ΔH and ΔV) and kinetic (CO rebinding rate constants) parameters associated with CO photodissociation and rebinding to the protein. We have also carried out cMD simulations wherein the protonation states of His73, His117, and His152 are controlled. Analysis of this data reveals that protonation of histidine residues within rHb1 can alter the geometry of the EF region and of hydrophobic cavities which serve as ligand migration pathways. This phenomenon may be relevant *in vivo* given that the intracellular pH in plant cells directly responds to conditions experienced by rice plants. In addition, the observation of a temperature dependence of the parameters resolved by PAC (ΔH and ΔV) is novel in the field of heme protein research. Our publication of these results is the first time this phenomenon has been observed and the first time a model has been proposed to explain it, namely that the interaction of the heme propionate groups with nearby charged residues (including Lys69 and Arg103) are dependent on temperature, ionic strength of the solvent, and the protonation states of histidine residues.

In chapter 4 I discuss human hemoglobin, where we observe a strong response of ΔH and ΔV associated with ligand photorelease to the presence of exogenous allosteric effectors and the ionic strength and pH of the sample buffer. We also observe the temperature dependence of these parameters in the case of photodissociation of O₂ from Hb, similar to photodissociation of CO from rHb1. Similarities between the two protein systems, including the presence of a strong hydrogen bond between the bound ligand and distal residue in both proteins, may help to form a theoretical foundation as to why the temperature dependence phenomenon is observed in multiple proteins.

Chapter 5 discusses the impact of the azole drugs ketoconazole and miconazole on the energetic, kinetics, and ligand migration pathways associated with CO photodissociation in fHbs from *C. necator* and *S. aureus*. Analysis of the PAC data in combination with computational results from Autodock Vina and cMD simulations suggests that the binding of azole drugs directly interferes with migration of ligands and electrons to the active site of fHbs, impeding the NOD catalytic cycle. The two primary ligand migration pathways identified in LES-enabled simulations of CO:FHP WT are located in close proximity to the binding sites for the two azole drugs, while ketoconazole and potentially miconazole bind to a hydrophobic cleft between the globin- and flavin-binding domains near the heme propionate groups; previous studies have predicted the heme propionates to be involved in electron transfer. This is the first time a molecular mechanism has been proposed to account for the impact of azole drugs on the NOD activity of fHbs and could be relevant to the design of antibiotics intended to inhibit this widely-distributed and well-conserved class of proteins.

In chapter 6, I discuss results obtained from PAC studies of the pH-jump induced folding of an intramolecular i-motif in a DNA oligomer. We were able to associate the energetics determined at fast time scales with protonation of the DNA oligomer, with partial formation of the i-motif structure occurring within ~140 ns. These results are in agreement with mass spectrometry results which indicate the formation of a number of folding intermediates.

Overall, the results demonstrate that the utility of photothermal and laser spectroscopy-based techniques such as PAC and TA in elucidating mechanisms of ligand/effector interaction with proteins and folding of a DNA oligomer. The use of theoretical approaches, including cMD simulations, supplements the utility of these techniques and can allow for a molecular mechanisms of ligand interactions with biomolecules or intramolecular interactions of biomolecules to be predicted.

LIST OF REFERENCES

1. Vinogradov, S. N.; Hoogewijs, D.; Bailly, X.; Arredondo-Peter, R.; Guertin, M.; Gough, J.; Dewilde, S.; Moens, L.; Vanfleteren, J. R. Three globin lineages belonging to two structural classes in genomes from the three kingdoms of life. *Proc. Natl. Acad. Sci. USA* **2005**, *102* (32), 11385-11389.
2. Poulos, T. L. Heme Enzyme Structure and Function. *Chem. Rev.* **2014**, *114*, 3919-3962.
3. Chapman, S. K.; Daff, S.; Munro, A. W. Heme: The most versatile redox centre in biology? In *Metal Sites in Proteins and Models*; Hill, H. A. O., Sadler, P. J., Thomson, A. J., Eds.; Springer-Verlag GmbH: Berlin, 1997; Vol. 88, pp 39-70.
4. Dewilde, S.; Kiger, L.; Burmester, T.; Hankeln, T.; Baudin-Creuz, V.; Aerts, T.; Marden, M. C.; Caubergs, R.; Moens, L. Biochemical Characterization and Ligand Binding Properties of Neuroglobin, a Novel Member of the Globin Family. *J. Biol. Chem.* **2001**, *276*, 38949-38955.
5. Sun, Y.; Jin, K.; Mao, X. O.; Zhu, Y.; Greenberg, D. A. Neuroglobin is up-regulated by and protects neurons from hypoxic-ischemic injury. *Proc. Natl. Acad. Sci. USA* **2001**, *98* (26), 15306-15311.
6. Hoy, J. A.; Hargrove, M. S. The structure and function of plant hemoglobins. *Plant Physiology and Biochemistry* **2008**, *46*, 371-379.
7. Forrester, M. T.; Foster, M. W. Protection from nitrosative stress: A central role for microbial flavohemoglobin. *Free Radical Biol. Med.* **2012**, *52*, 1620-1633.
8. Vinogradov, S. N.; Hoogewijs, D.; Bailly, X.; Mizuguchi, K.; Dewilde, S.; Moens, L.; Vanfleteren, J. R. A model of globin evolution. *Gene* **2007**, *398* (1-2), 132-142.
9. Wittenberg, J. A.; Bolognesi, M.; Wittenberg, B. A.; Guertin, M. Truncated Hemoglobins: A New Family of Hemoglobins Widely Distributed in Bacteria, Unicellular Eukaryotes, and Plants. *J. Biol. Chem.* **2002**, *277* (2), 871-874.
10. Paoli, M.; Marles-Wright, J.; Smith, A. Structure-Function Relationships in Heme-Proteins. *DNA Cell Biol.* **2004**, *21* (4), 271-280.

11. Kakar, S.; Hoffman, F. G.; Storz, J. F.; Fabian, M.; Hargrove, M. S. Structure and reactivity of hexacoordinate hemoglobins. *Biophys. Chem.* **2010**, *152*, 1-14.
12. Raphael, A. L.; Gray, H. B. Semisynthesis of Axial-Ligand (Position 80) Mutants of Cytochrome c. *J. Am. Chem. Soc.* **1991**, *113*, 1038-1040.
13. Tezcan, F. A.; Winkler, J. R.; Gray, H. B. Effects of Ligation and Folding on Reduction Potentials of Heme Proteins. *J. Am. Chem. Soc.* **1998**, *120*, 13383-13388.
14. Holm, R. H.; Kennepohl, P.; Solomon, E. I. Structural and Functional Aspects of Metal Sites in Biology. *Chem. Rev.* **1996**, *96*, 2239-2314.
15. Smaghe, B. J.; Kundu, S.; Hoy, J. A.; Halder, P.; Weiland, T. R.; Savage, A.; Venugopal, A.; Goodman, M.; Premer, S.; Hargrove, M. S. Role of Phenylalanine B10 in Plant Nonsymbiotic Hemoglobins. *Biochemistry* **2006**, *45*, 9735-9745.
16. Birukou, I.; Schweers, R. L.; Olson, J. S. Distal Histidine Stabilized Bound O₂ and Acts as a Gate for Ligand Entry in Both Subunits of Adult Human Hemoglobin. *Journal of Biological Chemistry* **2010**, *2851* (12), 8840-8854.
17. Sigfridsson, E.; Ryde, U. On the significance of hydrogen bonds for the discrimination between CO and O₂ by myoglobin. *J. Biol. Inorg. Chem.* **1999**, *4*, 99-110.
18. Lenfant, C.; Torrance, J.; English, E.; Finch, C. A.; Reynafarje, C.; Ramos, J.; Faura, J. Effect of Altitude on Oxygen Binding by Hemoglobin and on Organic Phosphate Levels. *J. Clin. Invest.* **1968**, *47*, 2652-2656.
19. Perutz, M. F. Stereochemistry of Cooperative Effects in Haemoglobin. *Nature* **1970**, *228*, 726-734.
20. Monod, J.; Wyman, J.; Jean-Pierre, C. On the Nature of Allosteric Transitions: A Plausible Model. *Journal of Molecular Biology* **1965**, *12*, 88-118.
21. Perutz, M. F.; Poyart, C. Bezafibrate lowers oxygen affinity of haemoglobin. *The Lancet* **1983**, *322* (8355), 881-882.

22. Lalezari, I.; Lalezari, P. Synthesis and Investigation of Effects of 2-[4-[[[(Arylamino)carbonyl]amino]phenoxy]-2-methylpropionic Acids on the Affinity of Hemoglobin for Oxygen: Structure-Activity Relationships. *Journal of Medicinal Chemistry* **1989**, *32* (10), 2352-2357.
23. Yonetani, T.; Park, S.; Tsuneshige, A.; Imai, K.; Kanaori, K. Global Allosteric Model of Hemoglobin. *The Journal of Biological Chemistry* **2002**, *277* (37), 34508-34520.
24. Tsuneshige, A.; Kanaori, K.; Samuni, U.; Danstker, D.; Friedman, J. M.; Neya, S.; Giangiacomo, L.; Yonetani, T. Semihemoglobins, High Oxygen Affinity Dimeric Forms of Human Hemoglobin Respond Efficiently to Allosteric Effectors without Forming Tetramers. *The Journal of Biological Chemistry* **2004**, *279* (47), 48959-48967.
25. Henry, E. R.; Bettati, S.; Hofrichter, J.; Eaton, W. A. A tertiary two-state allosteric model for hemoglobin. *Biophysical Chemistry* **2002**, *98*, 149-164.
26. Yang, F.; Phillips Jr, G. N. Crystal Structures of CO-, Deoxy- and Met-myoglobins at Various pH Values. *J. Mol. Biol.* **1996**, *256*, 762-774.
27. Spyrakis, F.; Faggiano, S.; Abbruzzetti, S.; Dominici, P.; Cacciatori, E.; Astegno, A.; Droghetti, E.; Feis, A.; Smulevich, G.; Bruno, S.; Mozzarelli, A.; Cozzini, P.; Viappiani, C.; Bidon Chanal, A.; Luque, F. J. Histidine E7 Dynamics Modulates Ligand Exchange between Distal Pocket and Solvent in AHb1 from *Arabidopsis thaliana*. *J. Phys. Chem. B* **2011**, *115*, 4138-4146.
28. Capece, L.; Boechi, L.; Perissinotti, L. L.; Arroyo-Mañez, P.; Bikiel, D. E.; Smulevich, G.; Marti, M. A.; Estrin, D. A. Small ligand-globin interactions: Reviewing lessons derived from computer simulation. *Biochimica et Biophysica Acta* **2013**, *1834*, 1722-1738.
29. Savino, C.; Miele, A. E.; Draghi, F.; Johnson, K. A.; Sciara, G.; Brunori, M.; Vallone, B. Pattern of Cavities in Globins: The Case of Human Hemoglobin. *Biopolymers* **2009**, *91* (12), 1097-1107.
30. Abbruzzetti, S.; Spyrakis, F.; Bidon-Chanal, A.; Luque, F. J.; Viappiani, C. Ligand migration through heme protein cavities: insights from laser flash photolysis and molecular dynamics simulations. *Phys. Chem. Chem. Phys.* **2013**, *15*, 10686-10701.

31. Brunori, M.; Gibson, Q. H. Cavities and packing defects in the structural dynamics of myoglobin. *EMBO Rep.* **2001**, *2*, 674-679.
32. Rajendran, A.; Nakano, S.-i.; Sugimoto, N. Molecular crowding of the cosolutes induces an intramolecular i-motif structure of triplet repeat DNA oligomers at neutral pH. *Chem. Commun.* **2010**, *46*, 1299-1301.
33. Dai, J.; Hatzakis, E.; Hurley, L. H.; Yang, D. I-Motif Structures Formed in the Human c-MYC Promoter Are Highly Dynamic - Insights into Sequence Redundancy and I-Motif Stability. *PLoS One* **2010**, *5* (7), e11647.
34. Porath, J. Immobilized metal ion affinity chromatography. *Protein Expression Purif.* **1992**, *3* (4), 263-281.
35. Mulder, P.; Korth, H.-G.; Pratt, D. A.; DiLabio, G. A.; Valgimigli, L.; Pedulli, G. F.; Ingold, K. U. Critical Re-evaluation of the O-H Bond Dissociation Enthalpy in Phenol. *J. Phys. Chem. A* **2005**, *109*, 2647-2655.
36. Mikšovská, J.; Larsen, R. W. Time-Resolved Photoacoustics Study of the Ruthenium(II) Bis(2,2'-bipyridine)(4,4'-dicarboxy-2,2'-bipyridine) Complex. *Inorg. Chem.* **2004**, *43*, 4051-4055.
37. Peters, K. S.; Watson, T.; Logan, T. Photoacoustic Calorimetry Study of Human Carboxyhemoglobin. *Journal of the American Chemical Society* **1992**, *114*, 4276-4278.
38. Mikšovská, J.; Horsa, S.; Davis, M. F.; Franzen, S. Conformational Dynamics Associated with Photodissociation of CO from Dehaloperoxidase Studied Using Photoacoustic Calorimetry. *Biochemistry* **2008**, *47*, 11510-11517.
39. Astudillo, L.; Bernad, S.; Derrien, V.; Sebban, P.; Miksovska, J. Reduction of the internal disulfide bond between Cys 38 and 83 switches the ligand migration pathway in cytoglobin. *J. Inorg. Biochem.* **2013**, *129*, 23-29.
40. Astudillo, L.; Bernad, S.; Derrien, V.; Sebban, P.; Miksovska, J. Probing the Role of the Internal Disulfide Bond in Regulating Conformational Dynamics in Neuroglobin. *Biophysical Journal* **2010**, *99* (2), L16-L18.

41. Goodman, M. D.; Hargrove, M. S. Quaternary Structure of Rice Nonsymbiotic Hemoglobin. *The Journal of Biological Chemistry* **2001**, *276* (2), 6834-6839.
42. Larsen, R. W.; Mikšovská, J. Time resolved thermodynamics of ligand binding to heme proteins. *Coord. Chem. Rev.* **2007**, *251*, 1101-1127.
43. Rubin, B., Ed. *IUPAC Solubility Data Series*; Pergamon Press: Oxford, 1981; Vol. 7: Oxygen and Ozone, pp 41-43.
44. Steinbach, P. J.; Ionescu, R.; Matthews, C. R. Analysis of Kinetics Using a Hybrid Maximum-Entropy/Nonlinear-Least-Squares Method: Application to Protein Folding. *Biophysical Journal* **2002**, *82*, 2244-2255.
45. Steinbach, P. J. Filtering artifacts from lifetime distributions when maximizing entropy using a bootstrapped model. *Analytical Biochemistry* **2012**, *427*, 102-105.
46. Hargrove, M. S.; Brucker, E. A.; Stec, B.; Sarath, G.; Arredondo-Peter, R.; Klucas, R. V.; Olson, J. S.; Phillips Jr, G. N. Crystal structure of a nonsymbiotic plant hemoglobin. *Structure* **2000**, *8*, 1005-1014.
47. Krieger, E.; Joo, K.; Lee, J.; Lee, J.; Raman, S.; Thompson, J.; Tyka, M.; Baker, D.; Karplus, K. Improving physical realism, stereochemistry, and side-chain accuracy in homology modeling: Four approaches that performed well in CASP8q. *Proteins: Struct., Funct., Bioinf.* **2009**, *77* (S9), 114-122.
48. Hoy, J. A.; Robinson, H.; Trent III, J. T.; Kakar, S.; Smaghe, B. J.; Hargrove, M. S. Plant Hemoglobins: A Molecular Fossil Record for the Evolution of Oxygen Transport. *J. Mol. Biol.* **2007**, *371* (1), 168-179.
49. El Hammi, E.; Warkentin, E.; Demmer, U.; Limam, F.; Marzouki, N. M.; Ermler, U.; Baciou, L. Structure of *Ralstonia eutropha* Flavohemoglobin in Complex with Three Antibiotic Azole Compounds. *Biochemistry* **2011**, *50*, 1255-1264.
50. Humphrey, W.; Dalke, A.; Schulten, K. VMD: Visual Molecular Dynamics. *J. Mol. Graphics* **1996**, *14* (1), 33-38.

51. Brooks, B. R.; Bruccoleri, R. E.; Olafson, B. D.; States, D. J.; Swaminathan, S.; Karplus, M. CHARMM: A program for macromolecular energy, minimization, and dynamics calculations. *J. Comput. Chem.* **1983**, *4* (2), 187-217.
52. Roitberg, A.; Elber, R. Modeling side chains in peptides and proteins: Application of the locally enhanced sampling and the simulated annealing methods to find minimum energy conformations. *J. Chem. Phys.* **1991**, *95* (12), 9277-9287.
53. Schmidtke, P.; Bidon-Chanal, A.; Luque, F. J.; Barril, X. MDpocket: Open Source Cavity Detection and Characterization on Molecular Dynamics Trajectories. *Bioinformatics* **2011**, *27* (23), 3276-3285.
54. Vázquez-Limón, C.; Hoogewijs, D.; Vinogradov, S. N.; Arredondo-Peter, R. The evolution of land plants hemoglobins. *Plant Sci.* **2012**, *191-192*, 71-81.
55. Wittenberg, J. B. Facilitated Oxygen Diffusion: The Role of Leghemoglobin in Nitrogen Fixation by Bacteroids Isolated from Soybean Root Nodules. *J. Biol. Chem.* **1974**, *249* (13), 4057-4066.
56. Hargrove, M. S.; Barry, J. K.; Brucker, E. A.; Berry, M. B.; Phillips Jr, G. N.; Olson, J. S.; Arredondo-Peter, R.; Dean, J. M.; Klucas, R. V.; Sarath, G. Characterization of Recombinant Soybean Leghemoglobin a and Apolar Distal Histidine Mutants. *J. Mol. Biol.* **1997**, *266*, 1032-1042.
57. Gibson, Q. H. The Kinetics of Ligand Binding to Plant Hemoglobins. *J. Biol. Chem.* **1989**, *264* (1), 100-107.
58. Arredondo-Peter, R.; Hargrove, M. S.; Sarath, G.; Moran, J. F.; Lohrman, J.; Olson, J. S.; Klucas, R. V. Rice Hemoglobins: Gene Cloning, Analysis, and O₂-Binding Kinetics of a Recombinant Protein Synthesized in Escherichia Coli. *Plant Physiol.* **1997**, *115*, 1259-1266.
59. Trevaskis, B.; Watts, R. A.; Andersson, C. R.; Llewellyn, D. J.; Hargrove, M. S.; Olson, J. S.; Dennis, E. S.; Peacock, W. J. Two hemoglobin genes in Arabidopsis thaliana - The evolutionary origins of leghemoglobins. *Proc. Natl. Acad. Sci. U. S. A.* **1997**, *94*, 12230-12234.
60. Bruno, S.; Faggiano, S.; Spyraakis, F.; Mozzarelli, A.; Abbruzzetti, S.; Grandi, E.; Viappiani, C.; Feis, A.; Mackowiak, S.; Smulevich, G.; Cacciatori, E.; Dominici, P. The Reactivity with

CO of AHb1 and AHb2 from *Arabidopsis thaliana* is Controlled by the Distal HisE7 and Internal Hydrophobic Cavities. *J. Am. Chem. Soc.* **2007**, *129*, 2880-2889.

61. Das, T. K.; Lee, H. C.; Duff, S. M. G.; Hill, R. D.; Peisach, J.; Rousseau, D. L.; Wittenberg, B. A.; Wittenberg, J. B. The Heme Environment in Barely Hemoglobin. *J. Biol. Chem.* **1999**, *274* (7), 4207-4212.

62. Bisht, N. K.; Abbruzzetti, S.; Uppal, S.; Bruno, S.; Spyrakis, F.; Mozzarelli, A.; Viappiani, C.; Kundu, S. Ligand migration and hexacoordination in type 1 non-symbiotic rice hemoglobin. *Biochim. Biophys. Acta* **2011**, *1814*, 1042-1053.

63. Scott, E. E.; Gibson, Q. H. Ligand Migration in Sperm Whale Myoglobin. *Biochemistry* **1997**, *36*, 1190-11917.

64. Vallone, B.; Nienhaus, K.; Brunori, M.; Nienhaus, G. U. The Structure of Murine Neuroglobin: Novel Pathways for Ligand Migration and Binding. *Proteins: Struct., Funct., Bioinf.* **2004**, *56*, 85-92.

65. Bogumil, R.; Maurus, R.; Hildebrand, D. P.; Brayer, G. D.; Mauk, A. G. Origin of the pH-Dependent Spectroscopic Properties of Pentacoordinate Metmyoglobin Variants. *Biochemistry* **1995**, *34*, 10483-10490.

66. Walther, M.; Raicu, V.; Ogilvie, J. P.; Phillips, R.; Kluger, R.; Miller, R. J. D. Determination of the Fe-CO Bond Energy in Myoglobin Using Heterodyne-Detected Transient Thermal Phase Grating Spectroscopy. *J. Phys. Chem. B* **2005**, *109*, 20605-20611.

67. Rovira, C.; Parrinello, M. First-Principles Molecular Dynamics Simulations of Models for the Myoglobin Active Center. *Int. J. Quantum Chem.* **2000**, *80*, 1172-1180.

68. Keyes, M. H.; Falley, M.; Lumry, R. Studies of Heme Proteins. II. Preparation and Thermodynamic Properties of Sperm Whale Myoglobin. *J. Am. Chem. Soc.* **1971**, *93* (8), 2035-2040.

69. Mokdad, A.; Mikšovská, J.; Larsen, R. W. Photothermal studies of CO photodissociation from peroxidases from horseradish and soybean. *Biochim. Biophys. Acta* **2009**, *1794*, 1558-1565.

70. Moore, J. C.; Battino, R.; Rettich, T. R.; Handa, Y. P.; Wilhelm, E. Partial Molar Volumes of "Gases" at Infinite Dilution in Water at 298.15 K. *J. Chem. Eng. Data* **1982**, *27*, 22-24.
71. Chance, M. R.; Courtney, S. H.; Chavez, M. D.; Ondrias, M. R.; Friedman, J. M. O₂ and CO Reactions with Heme Proteins: Quantum Yields and Geminate Recombination on Picosecond Time Scales. *Biochemistry* **1990**, *29*, 5537-5545.
72. Guilloux, V. L.; Schmidtke, P.; Tuffery, P. Fpocket: An open source platform for ligand pocket detection. *BMC Bioinf.* **2009**, *10*, 168.
73. Sakakura, M.; Yamaguchi, S.; Hirota, N.; Terazima, M. Dynamics of Structure and Energy of Horse Carboxymyoglobin after Photodissociation of Carbon Monoxide. *J. Am. Chem. Soc.* **2001**, *123*, 4286-4294.
74. Fago, A.; Hundahl, C.; Dewilde, S.; Gilany, K.; Moens, L.; Weber, R. E. Allosteric Regulation and Temperature Dependence of Oxygen Binding in Human Neuroglobin and Cytoglobin. *J. Biol. Chem.* **2004**, *279* (43), 44417-44426.
75. Kumar, S.; Nussinov, R. Salt Bridge Stability in Monomeric Proteins. *J. Mol. Biol.* **1999**, *293*, 1241-1255.
76. Shiroishi, M.; Yokota, A.; Tsumoto, K.; Kondo, H.; Nishimaya, Y.; Horii, K.; Matsushima, M.; Ogasahara, K.; Yutani, K.; Kumagai, I. Structural Evidence for Entropic Contribution of Salt Bridge Formation to a Protein Antigen-Antibody Interaction. *J. Biol. Chem.* **2001**, *276* (25), 23042-23060.
77. Wincel, H. Hydration Energies of Deprotonated Amino Acids from Gas Phase Equilibria Measurements. *J. Am. Soc. Mass Spectrom.* **2008**, *19*, 1091-1097.
78. Westrick, J. A.; Peters, K. S.; Ropp, J. D.; Sligar, S. G. Role of the Arginine-45 Salt Bridge in Ligand Dissociation from Sperm Whale Carboxymyoglobin As Probed by Photoacoustic Calorimetry. *Biochemistry* **1990**, *29*, 6741-6746.
79. Sakakura, M.; Morishima, I.; Terazima, M. The Structural Dynamics and Ligand Releasing Process after the Photodissociation of Sperm Whale Carboxymyoglobin. *J. Phys. Chem. B* **2001**, *105*, 10424-10434.

80. Birukou, I.; Schweers, R. L.; Olson, J. S. Distal Histidine Stabilizes Bound O₂ and Acts as a Gate for Ligand Entry in Both Subunits of Adult Human Hemoglobin. *J. Biol. Chem.* **2010**, *285* (12), 8840-8854.
81. Boschcov, P.; Seidel, W.; Muradian, J.; Tominaga, M.; Paiva, A. C. M.; Juliano, L. Ionization Constants and Thermodynamic Parameters of Histidine and Derivatives. *Bioorg. Chem.* **1983**, *12*, 34-44.
82. Kuriyan, J.; Wilz, S.; Karplus, M.; Petsko, G. A. X-ray structure and refinement of carbon-monooxy (Fe II)-myoglobin at 1.5 Å resolution. *J. Mol. Biol.* **1986**, *192* (1), 133-154.
83. Grimsley, G. R.; Scholtz, J. M.; Pace, C. N. A summary of the measured pK values of the ionizable groups in folded proteins. *Protein Sci.* **2009**, *18*, 247-251.
84. Nienhaus, K.; Kriegl, J. M.; Nienhaus, G. U. Structural Dynamics in the Active Site of Murine Neuroglobin and Its Effects on Ligand Binding. *J. Biol. Chem.* **2004**, *279* (22), 22944-22952.
85. Sage, J. T.; Morikis, D.; Champion, P. M. Spectroscopic Studies of Myoglobin at Low pH: Heme Structure and Ligation. *Biochemistry* **1991**, *30*, 1227-1237.
86. Fang, T.-Y.; Zou, M.; Simplaceanu, V.; Ho, N. T.; Ho, C. Assessment of Roles of Surface Histidyl Residues in the Molecular Basis of the Bohr Effect and of β 143 Histidine in the Binding of 2,3-Bisphosphoglycerate in Human Normal Adult Hemoglobin. *Biochemistry* **1999**, *38*, 13423-13432.
87. Müller, J. D.; McMahon, B. H.; Chien, E. Y. T.; Sligar, S. G.; Nienhaus, G. U. Connection between the Taxonomic Substates and Protonation of Histidines 64 and 97 in Carbonmonoxy Myoglobin. *Biophys. J.* **1999**, *77*, 1036-1051.
88. Felle, H. H. pH: Signal and Messenger in Plant Cells. *Plant Biol. (Berlin, Ger.)* **2001**, *3*, 577-591.
89. Lira-Ruan, V.; Sarath, G.; Klucas, R. V.; Arredondo-Peter, R. Synthesis of hemoglobins in rice (*Oryza sativa* var. Jackson) plants growing in normal and stress conditions. *Plant Sci.* **2001**, *161*, 279-287.

90. Perazzolli, M.; Romero-Puertas, M. C.; Delledonne, M. Modulation of nitric oxide bioactivity by plant haemoglobins. *J. Exp. Bot.* **2006**, *57* (3), 479-488.
91. Belogortseva, N.; Rubio, M.; Terrell, W.; Mikšovská, J. The contribution of heme propionate groups to the conformational dynamics associated with CO photodissociation from horse heart myoglobin. *J. Inorg. Biochem.* **2007**, *101* (7), 977-986.
92. Perutz, M. F.; Muirhead, H.; Cox, J. M.; Goaman, L. C. G. Three-dimensional Fourier Synthesis of Horse Oxyhaemoglobin at 2.8 Å Resolution: The Atomic Model. *Nature* **1968**, *219*, 131-139.
93. Lalezari, I.; Lalezari, P.; Poyart, C.; Marden, M.; Kister, J.; Bohn, B.; Fermi, G.; Perutz, M. F. New Effectors of Human Hemoglobin: Structure and Function. *Biochemistry* **1990**, *29*, 1515-1523.
94. Tsuneshige, A.; Park, S.; Yonetani, T. Heterotropic effectors control the hemoglobin function by interacting with its T and R states - a new view on the principle of allostery. *Biophysical Chemistry* **2002**, *98*, 49-63.
95. Yokoyama, T.; Neya, S.; Tsuneshige, A.; Yonetani, T.; Park, S.-Y.; Tame, J. R. H. R-state Haemoglobin with Low Oxygen Affinity: Crystal Structures of Deoxy Human and Carbonmonoxy Horse Haemoglobin Bound to the Effector Molecule L35. *Journal of Molecular Biology* **2006**, *356*, 790-801.
96. Birukou, I.; Maillett, D. H.; Birukova, A.; Olson, J. S. Modulating Distal Cavities in the α and β Subunits of Human HbA Reveals the Primary Ligand Migration Pathway. *Biochemistry* **2011**, *50*, 7361-7374.
97. Lepeshkevich, S. V.; Biziuk, S. A.; Lemeza, A. M.; Dzhagarov, B. M. The kinetics of molecular oxygen migration in the isolated α chains of human hemoglobin as revealed by molecular dynamics simulations and laser kinetic spectroscopy. *Biochimica et Biophysica Acta* **2011**, *1814*, 1279-1288.
98. Murakawa, Y.; Nagai, M.; Mizutani, Y. Differences between Protein Dynamics of Hemoglobin upon Dissociation of Oxygen and Carbon Monoxide. *Journal of the American Chemical Society* **2012**, *134*, 1434-1437.

99. Lepeshkevich, S. V.; Karpiuk, J.; Sazanovich, I. V.; Dzhagarov, B. M. A Kinetic Description of Dioxygen Motion with α - and β -Subunits of Human Hemoglobin in the R-State: Geminate and Bimolecular Stages of the Oxygenation Reaction. *Biochemistry* **2004**, *43*, 1675-1684.
100. Mokdad, A.; Mikšovská, J.; Larsen, R. W. Photothermal studies of CO photodissociation from peroxidases from horseradish and soybean. *Biochimica et Biophysica Acta* **2009**, *1794*, 1558-1565.
101. Mikšovská, J.; Horsa, S.; David, M. F.; Franzen, S. Conformational Dynamics Associated with Photodissociation of CO from Dehaloperoxidase Studied Using Photoacoustic Calorimetry. *Biochemistry* **2008**, *47*, 11510-11517.
102. Miksovska, J.; Astudillo, L. Time Resolved Thermodynamics Associated with Diatomic Ligand Dissociation from Globins. In *Thermodynamics - Interaction Studies - Solids, Liquids and Gases*; Moreno-Pirajan, J. C., Ed.; InTech, 2011.
103. Zhou, T.; Battino, R. Partial Molar Volumes of 13 Gases in Water at 298.15 K and 303.15 K. *Journal of Chemical & Engineering Data* **2001**, *46*, 331-332.
104. Esquerra, R. M.; López-Peña, I.; Tipgunlakant, P.; Birukou, I.; Nguyen, R. L.; Soman, J.; Olson, J. S.; Kliger, D. S.; Goldbeck, R. A. Kinetic spectroscopy of heme hydration and ligand binding in myoglobin and isolated hemoglobin chains: an optical window into heme pocket water dynamics. *Physical Chemistry Chemical Physics* **2010**, *12*, 10270-10278.
105. Wilhelm, E.; Battino, R.; Wilcock, R. J. Low-Pressure Solubility of Gases in Liquid Water. *Chemical Reviews* **1976**, *77* (2), 219-262.
106. Traylor, T. G.; Berzini, A. P. Binding of O₂ and CO to hemes and hemoproteins. *Proceedings of the National Academy of Sciences of the United States of America* **1980**, *77* (6), 3171-3175.
107. Vetromile, C. M.; Miksovska, J.; Larsen, R. W. Time resolved thermodynamics associated with ligand photorelease in heme peroxidases and globins: Open access channels versus gated ligand release. *Biochimica et Biophysica Acta* **2011**, *1814*, 1065-1076.

108. Cho, H. S.; Dashdorj, N.; Schotte, F.; Graber, T.; Henning, R.; Anfinrud, P. Protein structural dynamics in solution unveiled via 100-ps time-resolved x-ray scattering. *Proceedings of the National Academy of Sciences of the United States of America* **2010**, *107* (16), 7281-7286.
109. Projahn, H.-D.; Dreher, C.; van Eldik, R. Effect of Pressure on the Formation and Deoxygenation Kinetics of Oxy-myoglobin. Mechanistic Information from a Volume Profile Analysis. *Journal of the American Chemical Society* **1990**, *112*, 17-22.
110. Leung, W. P.; Cho, K. C.; Chau, S. K.; Choy, C. L. Measurement of the protein-ligand bond energy of carboxy-myoglobin by pulsed photoacoustic calorimetry. *Chemical Physics Letters* **1987**, *141* (3), 220-224.
111. Losi, A.; Viappiana, C. Reaction volume and rate constants for the excited-state proton transfer in aqueous solutions of naphthols. *Chemical Physics Letters* **1998**, *289*, 500-506.
112. Terazime, M. Molecular volume and enthalpy changes associated with irreversible photo-reactions. *Journal of Photochemistry and Photobiology C: Photochemistry Reviews* **2002**, *3*, 81-108.
113. Benesch, R.; Benesch, R. E. The effect of organic phosphates from the human erythrocyte on the allosteric properties of hemoglobin. *Biochemical and Biophysical Research Communications* **1967**, *26* (2), 162-167.
114. Kumar, A. T. N.; Zhu, L.; Christian, J. F.; Demidov, A. A.; Champion, P. M. On the Rate Distribution Analysis of Kinetic Data Using the Maximum Entropy Method: Applications to Myoglobin Relaxation on the Nanosecond and Femtosecond Timescales. *J. Phys. Chem. B* **2001**, *105*, 7847-7856.
115. Lepeshkevich, S. V.; Dzhagarov, B. M. Effect of zinc and cadmium ions on structure and function of myoglobin. *Biochimica et Biophysica Acta* **2009**, *1794*, 103 - 109.
116. Noble, R. W.; Brunori, M.; Wyman, J.; Antonini, E. Studies on the Quantum Yields of the Photodissociation of Carbon Monoxide from Hemoglobin and Myoglobin. *Biochemistry* **1967**, *6* (4), 1216-1222.

117. Lepeshkevich, S. V.; Konovalova, N. V.; Dzhagarov, B. M. Laser Kinetic Spectroscopy Studies of the Bimolecular Oxygenation of α - and β -Subunits with the R-State of Human Hemoglobin. *Biochemistry (Moscow)* **2003**, *68* (5), 551-558.
118. Chernoff, D. A.; Hochstrasser, R. M.; Steele, A. W. Geminate recombination of O₂ and hemoglobin. *Proceedings of the National Academy of Sciences of the United States of America* **1980**, *77* (10), 5606-5610.
119. Bhattacharya, S.; Lecomte, J. T. J. Temperature Dependence of Histidine Ionization Constants in Myoglobin. *Biophysical Journal* **1997**, *73*, 3241-3256.
120. Chang, C.-k.; Simplaceanu, V.; Ho, C. Effects of Amino Acid Substitutions at β 131 on the Structure and Properties of Hemoglobin: Evidence for Communication between α 1 β 1- and α 2 β 2-Subunit Interfaces. *Biochemistry* **2002**, *41*, 5644-5655.
121. Kovalevsky, A. Y.; Chatake, T.; Shibayama, N.; Park, S.-Y.; Ishikawa, T.; Mustyakimov, M.; Fisher, Z.; Langan, P.; Morimoto, Y. Direct Determination of Protonation States of Histidine Residues in a 2 Å Neutron Structure of Deoxy-Human Normal Adult Hemoglobin and Implications for the Bohr Effect. *Journal of Molecular Biology* **2010**, *398*, 276-291.
122. Sun, D. P.; Zou, M.; Ho, N. T.; Ho, C. Contribution of Surface Histidyl Residues in the α -Chain to the Bohr Effect of Human Normal Adult Hemoglobin: Roles of Global Electrostatic Effects. *Biochemistry* **1997**, *36*, 6663-6673.
123. Perutz, M. F.; Fermi, G.; Abraham, D. J.; Poyart, C.; Bursaux, E. Hemoglobin as a Receptor of Drugs and Peptides: X-ray Studies of the Stereochemistry of Binding. *Journal of the American Chemical Society* **1986**, *108*, 1064-1078.
124. Richard, V.; Dodson, G. G.; Mauguén, Y. Human Deoxyhaemoglobin-2,3-Diphosphoglycerate Complex Low-Salt Structure at 2.5 Å Resolution. *Journal of Molecular Biology* **1993**, *233* (2), 270-274.
125. Park, S.-Y.; Yokoyama, T.; Shibayama, N.; Shiro, Y.; Tame, J. R. H. 1.25 Å Resolution Crystal Structures of Human Haemoglobin in the Oxy, Deoxy, and Carbonmonoxy Forms. *J. Mol. Biol.* **2006**, *360*, 690-701.

126. Lukin, J. A.; Simplaceanu, V.; Zou, M.; Ho, N. T.; Ho, C. NMR reveals hydrogen bonds between oxygen and distal histidines in oxyhemoglobin. *Proc. Natl. Acad. Sci. U.S.A* **2000**, *97* (19), 10354-10358.
127. Yonetani, T.; Laberge, M. Protein dynamics explain the allosteric behaviors of hemoglobin. *Biochim. Biophys. Acta* **2008**, *1784* (9), 1146-1158.
128. Yuan, Y.; Simplaceanu, V.; Ho, N. T.; Ho, C. An Investigation of the Distal Histidyl Hydrogen Bonds in Oxyhemoglobin: Effects of Temperature, pH, and Inositol Hexaphosphate. *Biochemistry* **2010**, *49*, 10606-10615.
129. Marden, M. C.; Bohn, B.; Kister, J.; Poyart, C. Effectors of hemoglobin: Separation of allosteric and affinity factors. *Biophys. J.* **1990**, *57*, 397-403.
130. Sottini, S.; Abbruzzetti, S.; Viappiani, C. Evidence for Two Geminate Rebinding States Following Laser Photolysis of R State Hemoglobin Encapsulated in Wet Silica Gels. *J. Phys. Chem. B* **2005**, *109* (23), 11411-11413.
131. Scott, E. E.; Gibson, Q. H.; Olson, J. S. Mapping the Pathways for O₂ Entry Into and Exit from Myoglobin. *J. Biol. Chem.* **2001**, *276* (7), 5177-5188.
132. Poole, R. K.; Hughes, M. N. New functions for the ancient globin family: bacterial responses to nitric oxide and nitrosative stress. *Molecular Microbiology* **2000**, *36* (4), 775-783.
133. Liu, L.; Zeng, M.; Hausladen, A.; Heltman, J.; Stamler, J. S. Protection from nitrosative stress by yeast flavohemoglobin. *Proceedings of the National Academy of Sciences of the United States of America* **2000**, *97* (9), 4672-4676.
134. Dupré-Crochet, S.; Erard, M.; NüBe, O. ROS production in phagocytes: why, when, and where? *Journal of Leukocyte Biology* **2013**, *94*, 657-670.
135. Hausladen, A.; Gow, A.; Stamler, J. S. Flavohemoglobin denitrosylase catalyzes the reaction of a nitroxyl equivalent with molecular oxygen. *Proc. Natl. Acad. Sci. USA* **2001**, *98* (18), 10108-10112.
136. El Hammi, E.; Houée-Lévin, C.; Řezáč, J.; Lévy, B.; Demachy, I.; Baciou, L.; de la Lande, A. New insights into the mechanism of electron transfer within flavohemoglobins: tunnelling

- pathways, packing density, thermodynamic and kinetic analyses. *Phys. Chem. Chem. Phys.* **2012**, *14*, 13872-13880.
137. Ferreiro, D. N.; Boechi, L.; Estrin, D. A.; Martí, M. A. The key role of water in the dioxygenase function of Escherichia coli flavohemoglobin. *J. Inorg. Biochem.* **2013**, *119*, 75-84.
138. Helmick, R. A.; Fletcher, A. E.; Gardner, A. M.; Gessner, C. R.; Hvitved, A. N.; Gustin, M. C.; Gardner, P. R. Imidazole Antibiotics Inhibit the Nitric Oxide Dioxygenase Function of Microbial Flavohemoglobin. *Antimicrobial Agents and Chemotherapy* **2005**, *49* (5), 1837-1843.
139. Ezzine, A.; Moussaoui, M.; El Hammi, E.; Marzouki, M. N.; Baciou, L. Antimicrobial Agents Act Differently on Staphylococcus aureus and Ralstonia eutropha Flavohemoglobins. *Applied Biochemistry and Biotechnology* **2014**, *173*, 1023-1037.
140. Shadrina, M. S.; Peslherbe, G. H.; English, A. M. O₂ and Water Migration Pathways between the Solvent and Heme Pockets of Hemoglobin with Open and Closed Conformations of the Distal HisE7. *Biochemistry* **2015**, *54*, 5279-5289.
141. Trott, O.; Olson, A. J. Autodock Vina: Improving the speed and accuracy of docking with a new scoring function, efficient optimization, and multithreading. *J. Comp. Chem.* **2010**, *31* (2), 455-461.
142. Ermler, U.; Siddiqui, R. A.; Cramm, R.; Friedrich, B. Crystal structure of the flavohemoglobin from Alcaligenes eutrophus at 1.75 Å resolution. *EMBO J.* **1995**, *14* (24), 6067-6077.
143. Esquerra, R. M.; Jensen, R. A.; Bhaskaran, S.; Pillsbury, M. L.; Mendoza, J. L.; Lintner, B. W.; Kilger, D. S.; Goldbeck, R. A. The pH Dependence of Heme Pocket Hydration and Ligand Rebinding Kinetics in Photodissociated Carbonmonoxymyoglobin. *J. Biol. Chem.* **2008**, *283* (20), 14165-14175.
144. Baron, R.; Setny, P.; McCammon, J. A. Water in Cavity-Ligand Recognition. *J. Am. Chem. Soc.* **2010**, *132*, 12091-12097.

145. Steinhoff, H.-J.; Schlitter, J.; Redhardt, A.; Husmeier, D.; Zander, N. Structural fluctuations and conformational entropy in proteins: entropy balance in an intramolecular reaction in methemoglobin. *Biochim. Biophys. Acta* **1992**, *1121*, 189-198.
146. Bochman, M. L.; Paeschke, K.; Zakian, V. A. DNA secondary structures: stability and functions of G-quadruplex structures. *Nat. Rev. Genet.* **2012**, *13*, 770-780.
147. Murchie, A. I. H.; Lilley, D. M. J. Retinoblastoma susceptibility genes contain 5' sequences with a high propensity to form guanine-tetrad structures. *Nucl. Acids Res.* **1992**, *20* (1), 49-53.
148. Guéron, M.; Leroy, J.-L. The i-motif in nucleic acids. *Curr. Opin. Struct. Biol.* **2000**, *10*, 326-331.
149. Jin, K. S.; Shin, S. R.; Ahn, B.; Rho, Y.; Kim, S. J.; Ree, M. pH-Dependent Structures of an i-Motif DNA in Solution. *J. Phys. Chem. B* **2009**, *113*, 1852-1856.
150. Donten, M. L.; Hamm, P.; VandeVondele, J. A Consistent Picture of the Proton Release Mechanism of oNBA in Water by Ultrafast Spectroscopy and Ab Initio Molecular Dynamics. *J. Phys. Chem. B* **2011**, *115*, 1075-1083.
151. Mikšovská, J.; Larsen, R. W. Photothermal Studies of pH Induced Unfolding of Apomyoglobin. *J. Protein Chem.* **2003**, *22* (4), 387-394.
152. Choi, J.; Kim, S.; Tachikawa, T.; Fujitsuka, M.; Majima, T. pH-Induced Intramolecular Folding Dynamics of i-Motif DNA. *J. Am. Chem. Soc.* **2011**, *133*, 16146-16153.
153. Bonetti, G.; Vecchi, A.; Viappiani, C. Reaction volume of water formation detected by time-resolved photoacoustic: photoinduced proton transfer between o-nitrobenzaldehyde and hydroxyls in water. *Chem. Phys. Lett.* **1997**, *269*, 268-273.
154. Lieblein, A. L.; Fürtig, B.; Schwalbe, H. Optimizing the Kinetics and Thermodynamics of DNA i-Motif Folding. *ChemBioChem* **2013**, *14*, 1226-1230.
155. Christensen, J. J.; Wrathall, D. P.; Izatt, R. M.; Tolman, D. O. Thermodynamics of Proton Dissociation in Dilute Aqueous Solution. *J. Phys. Chem.* **1967**, *71* (9), 3001-3006.

156. Mairanovskii, S. G.; Lishcheta, L. I. Rate constants of pyridine protonation at various temperatures as found from polarographic catalytic hydrogen waves. *Russ. Chem. Bull.* **1962**, *11*, 209-216.
157. Ganguly, S.; Kundu, K. K. Protonation/deprotonation energetics of uracil, thymine, and cytosine in water from e.m.f./spectrophotometric measurements. *Can. J. Chem.* **1994**, *72* (4), 1120-1126.
158. SantaLucia Jr., J. A unified view of polymer, dumbbell, and oligonucleotide DNA nearest-neighbor thermodynamics. *Proc. Natl. Acad. Sci. USA* **1998**, *95*, 1460-1465.
159. Kaushik, M.; Suehl, N.; Marky, L. A. Calorimetric unfolding of the bimolecular and i-motif complexes of the human telomere complementary strand. *Biophys. Chem.* **2007**, *126*, 154-164.
160. Leroy, J.-L.; Guéron, M. Solution structures of the i-motif tetramers of d(TCC), d(5methylCCT) and d(T5methylCC): novel NOE connections between amino protons and sugar protons. *Structure* **1995**, *3*, 101-120.
161. Phan, A. T.; Guéron, M.; Leroy, J.-L. The solution structure and internal motions of a fragment of the cytidine-rich strand of the human telomere. *J. Mol. Biol.* **2000**, *299* (1), 123-144.
162. Vojtěchovský, J.; Chu, K.; Berendzen, J.; Sweet, R. M.; Schlichting, I. Crystal Structures of Myoglobin-Ligand Complexes at Near-Atomic Resolution. *Biophys. J.* **1999**, *77* (4), 2153-2174.

VITA

DAVID BUTCHER

Born, Hollywood, Florida

2014 – 2017	Doctoral Candidate Florida International University, Miami FL
2016	Biomedical Research Initiative (BRI) Student Summer Research Award
2011 – 2014	Doctoral Student Florida International University, Miami FL
2008 – 2011	Bachelor of Science in Chemistry (Awarded) Florida International University, Miami FL
2006 – 2008	Bachelor of Science in Chemistry (Incomplete) University of Florida, Gainesville FL

PUBLICATIONS AND RECENT PRESENTATIONS

David Butcher, Myriam Moussaoui, Laura Baciou, Jaroslava Miksovska. (2017). Effects of Azole Drugs on Conformational Dynamics and Energetics Associated with CO Photorelease and Migration within Bacterial Flavohemoglobins. Biophysical Society 61st Annual Meeting. Poster Presentation.

David Butcher, Sophie Bernad, Valerie Derrien, Pierre Sebban, Jaroslava Miksovska. The Role of Ionic Strength and pH in Modulating Thermodynamic Profiles Associated with CO Escape from Rice Non-symbiotic Hemoglobin 1. *J. Phys. Chem. B.* 2017, *121* (2), 351 – 364.

Alyssa Garabedian, David Butcher, Jennifer L. Lippens, Jaroslava Miksovska, Prem P. Chapagain, Danielle Fabris, Mark E. Ridgeway, Melvin A. Park, Francisco Fernandez-Lima. Structures of the kinetically trapped i-motif DNA intermediates. *Phys. Chem. Chem. Phys.* 2016, *18*, 26691 – 26702

David Butcher, Laura Baciou, Myriam Moussaoui, Jaroslava Miksovska. Determination of Thermodynamic and Kinetic Parameters for CO Migration Within Bacterial

Flavohemoglobins of *Ralstonia eutropha* and *Staphylococcus aureus*. Biophysical Society 60th Annual Meeting. Poster Presentation.

David Butcher, Sophie Bernad, Valerie Derrien, Pierre Sebban, Jaroslava Miksovska. Role of ionic strength and the Bohr effect in modulating thermodynamic profiles associated with CO escape in rice non-symbiotic hemoglobin 1. Florida ACS Meeting and Exposition. Poster Presentation.

David Butcher, Laura Baciou, Myriam Moussaoui, Jaroslava Miksovska. Impact of Azole Drugs on Energetics, Kinetics, and Ligand Migration Pathways of CO Photo-dissociation in Bacterial Flavohemoglobins from *Cupriavidus necator* and *Staphylococcus aureus*. Manuscript in preparation.

David Butcher, Takashi Yonetani, Jaroslava Miksovska. Thermodynamic parameters for O₂ photo-release from hemoglobin:effector complexes. Manuscript in preparation.

David Butcher, Jaroslava Miksovska. Ligand migration pathways in rice type 1 non-symbiotic hemoglobin determined by locally enhanced sampling molecular dynamics. Manuscript in preparation.